

**Metal-insulator transition,
orbital symmetries and gaps
in correlated oxides:
an impurity control approach**

by

M. A. Hossain

B.Sc., The University of Dhaka, 2001
CASM, The University of Cambridge, 2002
M.Sc., The University of British Columbia, 2005

A THESIS SUBMITTED IN PARTIAL FULFILLMENT OF
THE REQUIREMENTS FOR THE DEGREE OF

DOCTOR OF PHILOSOPHY

in

The Faculty of Graduate Studies

(Physics)

THE UNIVERSITY OF BRITISH COLUMBIA

(Vancouver)

December, 2009

© M. A. Hossain 2009

Abstract

The primary objective of this research is to develop and study newer ways to control electronic properties of correlated oxide systems using impurities. This goal has been achieved by introducing dilute localized $3d$ Mn impurities in place of a delocalized $4d$ Ru sites in a 2-dimensional Ru-O matrix and doping an electronically reconstructed polar surface of YBCO via surface impurities.

The first part of the work concentrates on X-ray Absorption Spectroscopy (XAS) and Resonant Soft X-ray Scattering (RSXS) studies on lightly Mn doped $\text{Sr}_3\text{Ru}_2\text{O}_7$. Our goal is to understand the electronic structure of the material both at room and low temperature and ultimately to understand the mechanism behind the low temperature metal-insulator transition in this compound. With XAS, we zoom into the local electronic structure of the impurities themselves and discovered unusual valence and crystal field level inversion in the Mn impurities. With the help of density functional theory and cluster multiplet calculations, we developed a model to describe the hierarchy of the crystal field levels of the Mn impurities. Long range magnetic properties of the compound has been probed with Resonant Soft X-ray Scattering (RSXS) on the Mn and Ru L-edges. We have found and analyzed the $(\frac{1}{4}, \frac{1}{4}, 0)$ structurally forbidden diffraction peak and connected it to an antiferromagnetic instability in the parent compound. Doping dependent scattering studies revealed the magnetic structure of the low temperature insulating phase and ultimately the mechanism behind the metal-insulator transition itself.

Angle Resolved Photoemission Spectroscopy (ARPES) has been used to investigate the low energy electronic structure of underdoped high- T_c superconductor YBCO. It has been revealed that due to the presence of polar surfaces there is electronic reconstruction on the surface of a cleaved YBCO sample. A novel technique has been devised that allows one to control the surface doping level *in-situ* by evaporating Potassium (K) on the YBCO surface. We showed that K tunes the surface doping level by donating electrons and thereby makes it possible to continuously tune the surface doping level throughout the phase diagram.

Contents

Abstract	ii
Contents	iii
List of figures	v
List of abbreviations	xi
Acknowledgements	xii
Co-authorship statement	xvii
1 Introduction	1
1.1 Materials and problems	3
1.1.1 Structural/Lattice distortion	3
1.1.2 Competing ferro and antiferromagnetic fluctuations in ruthenates . .	6
1.1.3 Exploring the phase diagram of cuprates in a controlled way	8
1.2 Experimental techniques	9
1.2.1 XAS and X-ray linear dichroism	9
1.2.2 Bragg scattering	11
1.2.3 REXS: a combination of XAS and scattering	12
1.2.4 ARPES	14
1.3 Experimental conditions	14
1.4 Angular dependence of magnetic scattering intensity	17
1.5 Few concepts	19
1.5.1 Orbital hierarchy and Jahn-Teller distortion	20
1.5.2 Hybridization and bonding-antibonding splitting	21
1.5.3 Probing the magnetism of a dilute lattice liquid	23
1.5.4 Polar surfaces	25
1.6 Scope	26
Bibliography	29
2 Crystal-field level inversion in lightly Mn-doped Sr₃Ru₂O₇	31
Bibliography	39

3	Magnetic superstructure and M-I transition in Mn-substituted $\text{Sr}_3\text{Ru}_2\text{O}_7$	40
	Bibliography	48
4	Nested Fermi surface and electronic instability in $\text{Ca}_3\text{Ru}_2\text{O}_7$	49
	Bibliography	57
5	<i>In-situ</i> doping control of the surface of high-T_c cuprates	58
	Bibliography	69
6	Two gaps make a high-temperature superconductor?	72
	Bibliography	83
7	Conclusions	91
	7.1 Signature of long range antiferromagnetism from XAS	91
	7.2 Puzzle of the energy gap	93
	7.3 Random impurities as a probe of spatially inhomogeneous order	95
	7.4 Scattering momentum scans	96
	7.5 Solitons in a 1D spin chain: effect on momentum scan width	97
	7.6 Summary, significance and possibilities: Ruthenates	98
	7.7 Summary, significance and possibilities: YBCO	100
	Bibliography	103
A	List of publications	104

List of figures

1.1	Unit cell of (a) Mn doped $\text{Sr}_3\text{Ru}_2\text{O}_7$ where the Mn impurity position is denoted by the red cage. (b) $\text{Ca}_3\text{Ru}_2\text{O}_7$ showing the rotation and tilting of the octahedra. (c) $\text{YBa}_2\text{Cu}_3\text{O}_{7-\delta}$ where $\delta = 0.5$, i.e. alternating full and empty CuO chains.	3
1.2	(Left) A diagram of R_M vs R_A for $\text{A}_3\text{M}_2\text{O}_7$ type of structure where A and M denote Ca/Sr and Ru/Mn respectively. (Right) Building block of a $\text{A}_3\text{M}_2\text{O}_7$ structure showing inequivalent oxygen sites (taken from [8]).	4
1.3	(a) Phase diagram of $\text{Ca}_{2-x}\text{Sr}_x\text{RuO}_4$. Taken from Nakatsuji <i>et al.</i> [31]. (b) Fermi surface of Sr_2RuO_4 . Taken from Damascelli <i>et al.</i> [32]. (c) Map of momentum dependent susceptibility. Taken from [33] (d) Temperature dependence of the resistivity of $\text{Sr}_3(\text{Ru}_{1-x}\text{Mn}_x)_2\text{O}_7$ for different Mn doping x . The electrical current was fed in the ab plane. Taken from Mathieu <i>et al.</i> [22].	7
1.4	Left: Energy scales in cuprates revealed by a combination of experimental techniques on many different cuprate high- T_c compound with doping level spanning the entire phase diagram (for detail, see Chapter 6). Right: Phase diagram of cuprate high- T_c compound YBCO explored by a single experimental technique on a single piece of sample (for detail, see Chapter 5). . .	8
1.5	(left) Typical XAS spectra obtained from $\text{Sr}_3(\text{Mn}_x\text{Ru}_{1-x})_2\text{O}_7$. (Middle left) Schematic presentation of Mn L-edge XAS transitions (Mn $2p \rightarrow 3d$). (Middle) Crystal field levels of Mn 4+ and 3+ together with corresponding e_g hole symmetry. (Middle right) Possible L-edge transitions with in-plane and out-of-plane polarized light	10
1.6	Schematic diagrams describing the electronic transitions involved with the X-ray absorption, Thomson scattering and resonant X-ray scattering processes.	12
1.7	REXS geometry defining the π and σ polarization and angles, θ , α , ϕ	17
1.8	Azimuthal angle dependence at the Mn edge of the integrated intensity of the $(\frac{1}{4}, \frac{1}{4}, 0)$ resonant diffraction peak at the $\sigma'\pi$ channel ($I_{\sigma'\pi} = f_{\uparrow}^{\sigma'\pi} - f_{\downarrow}^{\sigma'\pi} ^2$, blue), $\pi'\pi$ channel ($I_{\pi'\pi} = f_{\uparrow}^{\pi'\pi} - f_{\downarrow}^{\pi'\pi} ^2$, green). With the lack of an analyzer on the scattered photon side, we could only measure the total intensity, $I_{\sigma'\pi} + I_{\pi'\pi}$, shown by the solid red line (see Chapter 3 for detail).	19
1.9	(Left) Schematic presentation of crystal field splitting of transition metal d level when the symmetry is reduced from spherical to tetragonal. (Middle) electron population of the levels for Ru and Mn 4+ and Mn 3+. (Top right) spatial symmetry of the e_g levels.	20

1.10	Schematic presentation of hybridization between Mn impurity e_g levels split by local reduction of symmetry with the oxygen environment set by the RuO matrix.	22
1.11	(Left top, bottom) Non-magnetic square lattice and the corresponding reciprocal space map showing the structural Bragg peaks. (Right top, bottom) Antiferromagnetic lattice and the corresponding reciprocal space map showing magnetic diffraction peaks together with the structural ones.	23
1.12	(a,d) Non-magnetic square lattice and the corresponding reciprocal space map showing the structural Bragg peaks. (b,e) 100% Mn doped square lattice having an up-up-down-down zig-zag spin order and the corresponding reciprocal lattice map showing only the magnetic diffraction peaks. (c,f) Randomly selected 5% lattice points from (b) and the corresponding diffraction spots resulting from the scattered intensities only from these sites.	24
1.13	Examples of oxide interfaces with polar catastrophe inducing charge reconstruction. Top and bottom panels showing LaO/TiO and AlO/SrO interfaces together with charge density, electric field and potential as a function of layer thickness. Left and right shows the interfaces before and after the charge reconstruction respectively. Taken from [4].	26
1.14	Schematic presentation of net ionic charges of YBCO layers that can lead to polar catastrophe. This unfavorable situation can be resolved by simply removing $+1/2$ electronic charge from the topmost layer ($-1/2$ for the $ 1 - 1 + 1 - 1 + \dots$ series of the BaO termination).	27
2.1	Isotropic Mn $L_{2,3}$ -edge XAS data from $\text{Sr}_3(\text{Ru}_{0.9}\text{Mn}_{0.1})_2\text{O}_7$ and stoichiometric Mn-oxides of known valences. Inset: detailed view of the L_3 -edge chemical shift.	33
2.2	(a) Polarization-dependent Mn $L_{2,3}$ -edge XAS spectra from $\text{Sr}_3(\text{Ru}_{0.9}\text{Mn}_{0.1})_2\text{O}_7$ at $T = 295$ K. (b) Scheme of the XAS process: the L_2 (L_3) edge corresponds to the excitation of a Mn $2p_{1/2}$ ($2p_{3/2}$) electron to the Mn $3d$ valence shell. The L_3 - L_2 energy separation is due to the $2p$ core level spin-orbit coupling. (c) Corresponding experimental linear dichroism: $\text{LD} = [I_{\text{XAS}}(\mathbf{E} \perp c) - I_{\text{XAS}}(\mathbf{E} \parallel c)]$. (d) Calculated LD spectra for two possible e_g -orbital occupations ($x \parallel a, y \parallel b, z \parallel c$).	34
2.3	Density-of-states (DOS) of stoichiometric (a) $\text{Sr}_3\text{Ru}_2\text{O}_7$ (Ru327), (b) $\text{Sr}_3\text{Mn}_2\text{O}_7$ (Mn327) with the crystal structure of Ru327, and (c) Sr_2RuO_4 (Ru214).	35
2.4	(a,b) Spin-up density-of-states (DOS) from LSDA calculations for out-of-plane $d_{3z^2-r^2}$ and in-plane $d_{x^2-y^2}$ Mn e_g orbitals in 11% Mn-doped Ru oxides. (c-f) Ru-O/Mn-impurity hybridization leading to the Mn orbital hierarchy inversion: (c,f) energy of out-of-plane and in-plane Mn-impurity and O orbitals in the $\text{Sr}_3\text{Ru}_2\text{O}_7$ host material before the Mn-O hybridization is turned on; (d,e) once the O/Mn-impurity hybridization is considered, the Mn e_g -orbital hierarchy is inverted ($\Delta_{CF} > 0$) if $\tau_z^2/\Delta_z - \tau_x^2/\Delta_x > \delta$	37

-
- 3.1 (a) Mn and Ru (inset) resonance profile for the $(\frac{1}{4}, \frac{1}{4}, 0)$ superlattice diffraction peak measured at 20 K on $\text{Sr}_3(\text{Ru}_{1-x}\text{Mn}_x)_2\text{O}_7$ with $x = 0.1$. The arrows at 641 and 2968 eV indicate the energies used in the REXS experiments. (b) 10 % Mn rocking curves (' θ scans') for two different azimuthal angles measured at 641 eV and 20 K: $\phi = -5^\circ$ corresponds to $\sim (1/4, 1/4, l)$ scan probing the c -axis component of the order; $\phi = 90^\circ$ corresponds to a $(h, -k, 0)$ scan probing the ab in-plane component. At (c) 10 % Mn $(\frac{1}{4} + \Delta q, \frac{1}{4} + \Delta q, 0)$ momentum scans (' $\theta-2\theta$ scans') at 641 eV for different temperatures. (d) Temperature dependence of the integrated intensity of the Mn-edge $(\frac{1}{4} + \Delta q, \frac{1}{4} + \Delta q, 0)$ momentum scans for $x=5$ and 10 % samples. (e) Same as (d), for the $x=10$ % sample only, at the Ru edge. 42
- 3.2 Azimuthal-angle dependence of the $(\frac{1}{4} + \Delta q, \frac{1}{4} + \Delta q, 0)$ momentum scan integrated intensity, at the Ru and Mn edge for the $x = 0.1$ sample. Both datasets are fitted to the formula $I_{(\frac{1}{4}, \frac{1}{4}, 0)}^{total} = I_{(\frac{1}{4}, \frac{1}{4}, 0)}^{\pi \rightarrow \sigma'} + I_{(\frac{1}{4}, \frac{1}{4}, 0)}^{\pi \rightarrow \pi'} \propto |\cos \theta \cos \phi|^2 + |\sin 2\theta \sin \phi|^2$. Due to the different Mn and Ru scattering angles ($\theta_{Mn} = 61.6^\circ$; $\theta_{Ru} = 10.9^\circ$), the ratio between $(\pi \rightarrow \sigma')$ and $(\pi \rightarrow \pi')$ scattering signals is also different and the maximum intensity position is shifted by 90° in ϕ . The experimental geometry and the two highest symmetry spin patterns consistent with the data are also shown. 43
- 3.3 (a) Normalized Mn-edge $(\frac{1}{4} + \Delta q, \frac{1}{4} + \Delta q, 0)$ momentum scans at 20 K for 5 % (with Lorentzian fit) and 10 % Mn concentration; raw data are shown in the inset. (b) Inverse FWHM of the momentum scans vs. temperature. 45
- 3.4 (a,d,g) Spin-ordered islands in the RuO_2 plane for various Mn contents and spin correlations: (a) 5 % Mn, uncorrelated Mn spins; (d) 5 % Mn, correlated Mn spins; (g) 10 % Mn, correlated Mn spins. (b,e,h) Corresponding location of Mn impurities with up/down (blue/red) spins. (c,f,i) Reciprocal space map of the Mn scattering intensity generated by averaging over 200 random Mn-impurity distributions, of the kind in (b,e,h), to reduce noise. 46
- 4.1 (a), (b) valence band spectra of $\text{Sr}_3\text{Ru}_2\text{O}_7$ and $\text{Ca}_3\text{Ru}_2\text{O}_7$ taken with equal momentum steps along ΓM ($h\nu = 21.2$ eV, $T = 10$ K). In (c), (d) spectra of the two compounds have been normalized to the total spectral weight of the valence band (integrated from 0 to -7 eV), and are compared on two different energy scales. A fit of the low energy weight assuming a FL - like QP on a rising incoherent part, indicates a self energy $\Sigma_I \approx 5$ meV at $E - E_F \approx 15$ meV. 51
- 4.2 (a), (b) Momentum distribution of the lowest lying spectral weight in $\text{Ca}_3\text{Ru}_2\text{O}_7$ at $T = 9$ K. The two different energy windows correspond to effective resolutions of 25 meV and 10 meV, respectively. Red lines in (b) indicate momentum space locations of the dispersion plots in Fig. 4.3 (c) Schematic of the dominant features in the low energy excitations. The small Fermi arc near the M-point is back-folded by the proposed nesting vector to connect to a closed Fermi surface contour (see text). (d) Selected spectra, extracted from the data-set of (a),(b) demonstrating different gap sizes for various points in the BZ. Metallic states are found only in the vicinity of the M-points. . . . 53

-
- 4.3 (a),(b) Dispersion of QP states along ΓM displayed as false color plot or stack of equally spaced EDCs, respectively. A metallic band is found near the M-point. White dots indicate the peak positions found from Lorentzian fits to MDCs. (c)–(e) are taken along the momentum space lines indicated in Fig. 4.2(b) and show in detail how the bands bend back and a gap opens as the nested part of the underlying FS is approached. White dots mark the peak positions in EDCs. 54
- 4.4 Temperature and momentum dependence of the gap. (a) shows spectra taken at 9 K and 52 K along the red line depicted in the BZ inset. (b) Temperature series of spectra at point '3'. (c) Evolution of the leading edge gap with temperature for momentum space points 1–3 with $(k_x, k_y) = (0.88\frac{\pi}{a}, 0)$; $(0.69\frac{\pi}{a}, 0.34\frac{\pi}{b})$; $(0.5\frac{\pi}{a}, 0.5\frac{\pi}{b})$, respectively. 55
- 5.1 **The surface of cleaved YBCO.** (a) Structure of oxygen-ordered YBCO6.5 (with alternating oxygen full and empty chains), showing the BaO and CuO chain terminations of the cleaved surface. Electronic reconstruction takes place at these polar surfaces, similar to the prototypical case of a polar catastrophe in ionic insulators with a $|1 + |1 - |1 + |1 - | \dots$ layer-by-layer charge [25]. This leads to 'overdoped-like' FS features for the surface topmost layers, as shown pictorially in (b) for CuO₂-plane bonding and antibonding bands (FS_B and FS_{AB}), and the one-dimensional CuO chain band (FS_{Ch}). 59
- 5.2 **YBCO FS evolution upon e^- doping.** (a) ARPES FS of as-cleaved YBCO6.5, exhibiting an effective hole doping $p = 0.28$ per planar Cu atom, as determined from the average area of bonding and antibonding CuO₂-bilayer FSs. (b,c) By evaporating potassium on the same sample (< 1 monolayer), electrons are transferred to the top-most CuO₂ bilayer and the corresponding FSs become progressively more hole-underdoped. (c) For heavy K-deposition ($p = 0.11$ as estimated from the area of the chain FS), the E_F ARPES intensity reduces to the 1D CuO chain FS and four disconnected nodal CuO₂ FS arcs. 60
- 5.3 **YBCO dispersion and EDC evolution upon e^- doping.** (a,b) The BaO band high-energy shift in YBCO6.5 as compared to YBCO6.5 reveals that electrons are added upon K deposition; also, bonding (B) and antibonding (AB) CuO₂ features vanish at the antinodes and only the CuO chain band is detected. (c-e) Nodal (N) and antinodal (AN) k_F EDCs showing the progressive opening of an AN gap and loss of CuO₂-plane quasiparticle coherence upon underdoping ($\Delta \sim 10$ and 80 meV for YBCO6.5 and YBCO6.5); the B and AB splitting is resolved only for as-cleaved YBCO6.5. 62

-
- 5.4 **Phase diagram of YBCO by ARPES.** Schematic temperature-doping phase diagram of YBCO adapted from Ref. [7]. The hole doping p per planar copper ($p=0$ for the 1/2-filled Mott insulator with 1 hole per Cu atom), and the corresponding oxygen content ($7-\delta$), are indicated on bottom and top axes [23]. The ARPES FS for under- and overdoped YBCO is also shown; the momentum-distribution maps have been 2-fold and 4-fold symmetrized for $p=0.11$ and 0.28 , respectively. Similar to the data in Fig. 5.2, the doping levels were determined for $p=0.11$ from the area of FS_{Ch} , and for $p=0.28$ from the area of FS_B and FS_{AB} 63
- 5.5 **YBCO MDC evolution upon e^- doping.** MDCs measured on (a) as-cleaved and (b,c) K-deposited YBCO6.5, along the same momentum-space direction of the EDCs shown in Fig. 5.3(a,b), yet limited to the $k_x = -\pi$ and $k_y = [-\pi, \pi]$ range. The energy step between adjacent MDCs is of 15 meV. Also note that, due to the relative peak/background intensity decrease upon K deposition, the MDCs for YBCOK1 and YBCOK2 have been rescaled by a factor of 4.4 and 7.2, respectively, with respect to those of as-cleaved YBCO6.5. 67
- 6.1 Various scenarios for the interplay of pseudogap (blue dashed line) and superconductivity (red solid line) in the temperature-doping phase diagram of the HTSCs. While in (a) the pseudogap merges gradually with the superconducting gap in the strongly overdoped region, in (b) and (c) the pseudogap lines intersects the superconducting dome at about optimal doping (i.e., maximum T_c). In most descriptions, the pseudogap line is identified with a crossover with a characteristic temperature T^* rather than a phase transition; while at all dopings $T^* > T_c$ in (a), beyond optimal doping $T^* < T_c$ in (b) and T^* does not even exist in (c). Adapted from Ref.[12]. 74
- 6.2 Pseudogap ($E_{pg} = 2\Delta_{pg}$) and superconducting ($E_{sc} \sim 5k_B T_c$) energy scales for a number of HTSCs with $T_c^{max} \sim 95$ K (Bi2212, Y123, Tl2201, and Hg1201). The datapoints were obtained, as a function of hole doping x , by angle-resolved photoemission spectroscopy (ARPES), tunneling (STM, SIN, SIS), Andreev reflection (AR), Raman scattering (RS), and heat conductivity (HC). On the same plot we are also including the energy Ω_r of the magnetic resonance mode measured by inelastic neutron scattering (INS), which we identify with E_{sc} because of the striking quantitative correspondence as a function of T_c . The data fall on two universal curves given by $E_{pg} = E_{pg}^{max}(0.27 - x)/0.22$ and $E_{sc} = E_{sc}^{max}[1 - 82.6(0.16 - x)^2]$, with $E_{pg}^{max} = E_{pg}(x = 0.05) = 152 \pm 8$ meV and $E_{sc}^{max} = E_{sc}(x = 0.16) = 42 \pm 2$ meV (the statistical errors refer to the fit of the selected datapoints; however, the spread of all available data would be more appropriately described by ± 20 and ± 10 meV, respectively). 75

6.3	Pseudogap E_{pg} and superconducting E_{sc} energy scales (2Δ) as estimated, by a number of probes and for different compounds, in one single experiment on the very same sample. These data provide direct evidence of for the simultaneous presence of two energy scales, possibly two spectral gaps, coexisting in the superconducting state. The superconducting and pseudogap lines are defined as in Fig. 6.2.	77
7.1	(a,c) Temperature dependent Mn L_2 -edge XAS spectra measured on 5 and 20% Mn-doped samples with $\mathbf{E} \parallel \mathbf{c}$. (b,d) Theoretical L_2 -edge spectra calculated with the inclusion of a 1meV antiferromagnetic exchange field: (b) H^{ex} 30° away from c -axis, $T_{N_{eel}}=50\text{K}$; (d) $H^{ex} \parallel c$ -axis, $T_{N_{eel}}=100\text{K}$. While no field dependence is observed in the 300K non-magnetic state ($T \gg H^{ex} = 1\text{meV} \simeq 10\text{K}$), a clear effect is seen once the ground state is antiferromagnetic. This demonstrates the extreme sensitivity of XAS and linear dichroism to the onset of antiferromagnetic ordering, that Mn impurities do induce antiferromagnetism in $\text{Sr}_3\text{Ru}_2\text{O}_7$, and that the field orientation varies progressively from out-of-plane (b) to in-plane (d) upon increasing Mn-doping from 5 to 20%.	92
7.2	Normalized L_2 -edge peak-height ratio, defined as $L_2^R(T)/L_2^R(15)$, where $L_2^R(T) = [\frac{I_A - I_B}{I_A + I_B}(T) - \frac{I_A - I_B}{I_A + I_B}(295)]$ and $I_{A,B}$ is the intensity of peak A, B in Fig. 7.1, plotted vs. temperature for 5, 10, and 20% Mn-doped $\text{Sr}_3\text{Ru}_2\text{O}_7$. For 20% Mn, the modulus of the data is plotted. The inset presents temperature dependent electrical resistivity data (in logarithmic scale), for the same samples [3]. A sharp increase is observed in both resistivity and X-ray linear dichroism experiments for 5 and 10% Mn, and only a continuous evolution for 20% Mn, indicating that the metal-insulator transition is driven by the onset of antiferromagnetic ordering.	93
7.3	(a) Band structure calculations performed for the distorted structure of the pure compound (after Ref. [5]). (b) Temperature dependent ARPES spectra measured on the 5% Mn-doped sample, in correspondence of the Fermi surface sheets originating from the xy band of the undistorted structure. (c) Across the metal-insulator antiferromagnetic transition a leading-edge gap opens, as seen also on other portions of the Fermi surface.	94
7.4	Interpretation of “ θ -scans” in two different azimuthal angle geometry of the sample with respect to the scattering plane. At $\phi = 0^\circ$ and 90° geometry one probes the order along the c -axis and ab -plane respectively.	96
7.5	Comparison of the momentum scan (“ $\theta - 2\theta$ ”) widths resulting from scattered intensities from: (a) 100% sites without domains with the same system having average domain size of 320 lattice spacing. (b) 100% sites from the system with domains with 10% randomly selected sites from the same system (normalized). (c) 10% random sites with measured $(\frac{1}{4} + \Delta q, \frac{1}{4} + \Delta q, 0)$ scan on 10% Mn doped $\text{Sr}_3\text{Ru}_2\text{O}_7$	97

List of abbreviations

ARPES	Angle Resolved Photoemission Spectroscopy
REXS	Resonant Elastic X-ray Scattering
XRD	X-Ray Diffraction
XAS	X-ray Absorption Spectroscopy
STM	Scanning Tunneling Microscope
STS	Scanning Tunneling Spectroscopy
TMO	Transition Metal Oxide
M-I Transition	Metal Insulator Transition
MIT	Metal Insulator Transition
DFT	Density Functional Theory
LDA	Local Density Approximation
HTSC	High Temperature Superconductor
Tl2201	$\text{Tl}_2\text{Ba}_2\text{CuO}_{6+\delta}$
YBCO	$\text{YBa}_2\text{Cu}_3\text{O}_{7-\delta}$
LSCO	$\text{La}_{2-x}\text{Sr}_x\text{CuO}_4$
NCCO	$\text{Nd}_{2-x}\text{Ce}_x\text{CuO}_4$

Acknowledgements

During my PhD I have had the opportunity to work with many exceptional scientists in many different institutes and synchrotrons. I must admit that my command of English language is not good enough to do a proper job of thanking all these great individuals (but I will try anyway!). I have categorized the acknowledgement section on the basis of institutes starting with my home for about 6.5 years: The University of British Columbia (UBC).

University of British Columbia, Vancouver, Canada:

Prof. Andrea Damascelli: It gives me great pleasure to thank my PhD supervisor, Prof. Andrea Damascelli. When I began as a MSc student in Andrea's group, I had no idea about what experimental physics means. Andrea taught me the ABCs of experiments and guided me through the exciting world of correlated oxide physics with great patience and surprising enthusiasm. While Andrea guided me intensively during the early years, he also gave me great freedom during the later years of my PhD degree; a supervision style that worked perfect for me. It was only Andrea's encouragement and support that enabled me to try out many ideas. Of course, some of them did not work but that was never a problem for him. I was immensely benefited from the vibrant research environment of the group that Andrea strives to maintain, giving us the chance to work and collaborate with visitors and international leaders in our field. I would like to add that I am proud to be Andrea's first student.

Prof. George Sawatzky: I must admit that it has been an overwhelming experience to be around Prof. George Sawatzky and have him as one of my mentors who is one of the global leaders in the field of spectroscopy and correlated electron physics, in both theoretical and experimental aspects. It was a great opportunity to have my first solid state physics course from George. I immediately got hooked to the subject! I would like to thank George for always keeping his door open and help us with his deep insight. All the projects I have been involved during my PhD have been enriched by many original ideas and interpretations by George. I will definitely miss those never ending discussions with George, Andrea and Ilya (Elfimov) whenever we had any interesting data or idea.

I would like to thank

Dr. Ilya Efimov for countless stimulating discussions and helping us with his electronic structure calculations. Ilya's rigorous approach to physics has helped us to refine many of our arguments. Also, Damascelli group members: Jeff Mottershead, Jason Zhu, Ryan Wicks, Jonathan Rosen, Dr. David Fournier, Dr. Giorgio Levy, Dr. Thomas Roth, Christian Veenstra, Mauro Plate, Dr. Markus Raichel and Sawatzky group members: Dr. Jochen Geck, Dr. David Hawthorn, Dr. Kyle Shen, Bayo Lau, Dr. Subhra SenGupta, Dr.

Hiroki Wadati, Dr. Andreas Riemann, Dr. Wilhelm Auerwarter and Dr. Nick Ingle for help and encouragement. I would also like to thank Barbara Tevarotto for wonderful parties at Damascelli-Tovarotto residence and for generously helping us out with her extreme graphics skill.

Prof. Doug Bonn and Prof. Walter Hardy of the famous Bonn-Hardy group of UBC for the very fruitful YBCO collaboration and, of course, for the life saving AMPEL coffee machine! Special thanks to Dr. Ruixing Liang who has taken the YBCO sample growth quality to a new level and providing us those extremely high quality samples. I gratefully remember Ruixing's help during my attempt to dope BSCCO crystals when I had no idea about how delicate these procedures can be. I would like to thank Pinder Dosanjh for help with SQUID measurements. Many thanks to Bonn-Hardy group members: Darren Peets, Jennifer Babiack and Jake Bobowski for humor, collaborations and help with sample preparation.

The distinguished visitors: Prof. Stefan Hühner for discussing his exciting ideas on cuprates and for being very generous to include me as a coauthor in his papers. I am deeply grateful and honored. Dr. Giancarlo Panaccione for many discussions on core level photoemission on ruthenates and also for teaching the wonderful course on synchrotron science.

My PhD committee members: Prof. Andrea Damascelli, Prof. Doug Bonn, Prof. Rob Kiefl, Prof. Johannes Barth and Prof. Fei Zhou for guiding me throughout my PhD years with valuable suggestions and encouragement.

Advanced Light Source (ALS), Lawrence Berkeley National Laboratory, Berkeley, CA, USA:

ALS Fellowship Selection Committee for awarding me the ALS doctoral fellowship in residence for three consecutive years (2006-09). I had a very exciting and productive time at ALS that houses some of the worlds most advanced spectroscopic tools together with a very warm and friendly environment.

Dr. Zahid Hussain for constant support and encouragement during my tenure as an ALS fellow and also for being very generous to let us use his Resonant Elastic X-ray Scattering (REXS) endstation.

Dr. Jonathan Denlinger for being my ALS mentor. I will miss those late night discussions in Jonathan's office and his enthusiasm for anything related to synchrotrons and physics in general.

Dr. Yi-De Chuang for many many reasons: allowing me to use his wonderful X-ray scattering chamber, teaching me the basics of REXS, helping me out during the measurements, letting me use many of his beamtime shifts when I needed to measure urgently etc. etc. It has been a real treat to work with Yi-De!

All the ALS beamline 7.0 scientists/personnel: Dr. Eli Rotenberg, Dr. Aaron Bostwick, Dr. Jessica McChesney for the YBCO collaboration and all the support at their amazing ARPES beamline.

All the ALS beamline 8.0.1, 4.0.2 and 6.3.1 scientists/personnel: Dr. Wanli Yang, Paul Olalde, Dr. Elke Arenholz, Dr. Marco Liberati for wonderful support during the measurements.

Universität zu Köln, Köln, Germany:

Prof. L. Hao Tjeng for his tremendous and enthusiastic help with our X-ray absorption paper and for letting me collaborate with his wonderful and deeply knowledgeable group. Chapter 2 of this thesis bears the mark of this creative collaboration. Whatever I learned about XAS is from Hao and his group and I have no doubt that I learned from the best!

Dr. Maurits Haverkort for doing lots of complicated cluster calculations for our XAS paper, explaining those calculations and teaching me how to do them! It has been an overwhelming experience to be around Maurits who not only has an amazing ability to understand the physics of correlated oxide systems in general but also an equally amazing ability and thirst to teach them to students like me. I certainly hope to continue collaborating with Maurits and continue to learn from him.

Dr. Zhiwei Hu for his skillful help during the measurements in Taiwan and also for those wonderful restaurant trips whenever we had a break. Dr. Christian Schüßler-Langeheine for his skillful help and discussions during the BESSY scattering measurements.

Max-Planck-Institut für Festkörperforschung (MPI), Stuttgart, Germany:

Prof. Bernhard Keimer for wonderful hospitality during my stays at Max Planck Institute, BESSY and also sharing his deep insights on the problems we were working together.

Britta Bohnenbuck for wonderful hospitality at MPI and BESSY. It has been a real pleasure to do experiments with her and sharing ideas. I learned a lot about scattering from Britta.

Stanford University and Stanford Synchrotron Radiation Lightsource (SSRL), Stanford, CA, USA:

Prof. Z.-X. Shen for collaborating with us on APRES measurements on $\text{Ca}_3\text{Ru}_2\text{O}_7$. It has been a pleasure to work with Dr. Felix Baumberger at the McCullough building basement lab in the Stanford campus. Dr. Donghui Lu for his help during the ARPES measurements at SSRL.

ELETTRA, Trieste, Italy:

Prof. Fulvio Permigiani for collaborating with our group and wonderful hospitality during our trip. It has been a pleasure to work with Dr. Federica Bondino, Dr. Onur Mentès, Dr. Marco Zangrando, Dr. Michele Zacchigna.

Berliner Elektronensp.-Gesellschaft für Synchrotronstrahlung (BESSY) and Hahn-Meitner Institut (HMI), Berlin, Germany:

Enrico Schierle and Eugen Weschke for letting us use their resonant scattering chamber.

National Synchrotron Radiation Research Center (NSRRC), Taiwan:

Prof. C. T. Chen for letting us use his famous dragon beamline for XAS measurements.

National Institute of Advanced Industrial Science and Technology (AIST), Tsukuba, Japan:

Dr. Yoshiyuki Yoshida for the very fruitful collaboration on Mn doped $\text{Sr}_3\text{Ru}_2\text{O}_7$ and providing us not only high quality samples but also all the sample characterization data whenever we needed. His help was particularly crucial when we needed very big samples for scattering measurements. It has been a pleasure with Yoshiyuki!

University of Tokyo, Kashiwa, Japan:

Prof. Yoshinori Tokura and Prof. Hidenori Takagi for the very fruitful collaboration on Mn doped $\text{Sr}_3\text{Ru}_2\text{O}_7$ and providing us high quality samples.

Family:

My journey from Bangladesh \rightarrow Cambridge \rightarrow Vancouver has only been possible because of the constant love and sacrifice of my parents. Sadly my father did not live to see it.

Sometimes the PhD program seemed like riding Blaine the Mono, the demented monorail train trying to commit suicide with its passengers ¹. It was only because of Arefa and Adi, the crazy train managed to reach its destination.

¹Stephen King, *The Dark Tower IV: Wizard and Glass*, Grant (1997).

To Arefa, of course

Co-authorship statement

- Chapter 2: My contributions to this project were to perform and analyze all the measurements presented in the paper. This involved performing the experiments at synchrotrons, generating ideas about the models and communicating between international collaborators etc. I also contributed to the cluster and band-structure calculations together with M.W. Haverkort and I.S. Elfimov. Finally, I co-wrote the manuscript with Prof. A. Damascelli.
- Chapter 3: My contributions to this project were to lead every aspect of the project starting from conceiving the idea of the experiments, writing proposals, performing the experiments, maintaining collaborations, analyzing all the data and modeling/simulating the data using Mathematica. I wrote the manuscript with inputs from coauthors, in particular, Prof. A. Damascelli.
- Chapter 4: My contributions to this paper were to perform some of the key measurements presented in the paper as well as some band structure calculations.
- Chapter 5: My contributions to this paper have been to perform all the experiments (with J.D.F. Mottershead), analyze all the data myself and co-writing the paper with Prof. A. Damascelli.
- Chapter 6: This project was conceived by Prof. Stefan Hufner during his sabbatical year at the University of British Columbia. I was part of the group on the UBC side that included Prof. G.A. Sawatzky and Prof. A. Damascelli, who contributed with ideas and co-wrote the paper.

Chapter 1

Introduction

The grand challenge of modern condensed matter physics is to work out a unified theory that can account for the entire phase diagram of strongly correlated electron systems such as copper oxide based high- T_c superconductors, manganites, ruthenium oxides etc. [1]. Materials like high- T_c superconductors can be continuously doped from a Mott insulating state to a metallic Fermi liquid state. On the other hand, ruthenium oxides like $\text{Sr}_3\text{Ru}_2\text{O}_7$, having a paramagnetic Fermi liquid state, show exotic behaviors like magnetic field tuned quantum criticality and electronic nematic liquid behavior. It is extremely difficult to formulate any microscopic theory for these materials due to the fact that many of these properties are emergent phenomena [2], i.e. collective correlated behavior emerging from strong correlation between the electrons in the system that cannot be explained by independent electron properties. Hence, theories and experiments go hand in hand in this frontier of physics like no other. On the experimental side, spectroscopies have provided some of most revealing data available on these materials where one perturbs the system with an external source and measure the response of the system. The complex nature of emergent phenomena has created an urgency to gain better control on the material side so that one can disentangle and focus on a specific property of the material. In this thesis, we used impurities for this purpose. Impurities have been introduced in the bulk and the surface of the correlated oxides to perturb the system in a controlled way, e.g. triggering a key property or stabilizing some inherent fluctuation in the system. This has been shown to serve a dual purpose by allowing us to probe the defining properties of the host system and the host-impurity interaction and also, as a bonus, allow us to observe how impurities themselves behave in exotic environments.

Impurities have always been of paramount importance in the study of strongly correlated oxides. The standard procedure has been to introduce impurities of different size than the host atoms to introduce structural changes in the material or to introduce impurities with different valence as a way to dope the system. But there are other degrees of freedom than structure and charge, namely orbital, spin etc. and part of our approach has been to exploit these less-explored degrees of freedom, for instance, by introducing dilute localized $3d$ Mn impurities in place of a delocalized $4d$ Ru sites in a Ru-O matrix. We have shown that very unusual situations can arise both locally and globally due to the orbital and spin mismatch between the impurity and the host [3]. In the dilute limit of 5% Mn doping of $\text{Sr}_3\text{Ru}_2\text{O}_7$ we observed reversal of crystal-field levels, unconventional valence in Mn and development of long-range antiferromagnetic and possibly orbital order below the metal-insulator transition temperature. This has opened the possibility of tailoring new materials by introducing a variety of $3d$ impurities to $4d$ or even $5d$ systems and also forms another intriguing example of local magnetic changes leading the way to global order, nanoscale phase separation and

eventually a spatially inhomogeneous metal-insulator transition that challenges the current standard theories of materials.

These strange materials pose unique challenges for experiments and novel ideas have to be in place to describe the correct electronic state of the material. In case of YBCO, oxygen doping has been used as a tuning parameter to take the system through phases such as insulator to metal. But it is critical to understand that YBCO contains polar surfaces. While Angle Resolved Photoemission Spectroscopy (ARPES) is a very powerful experimental tool to observe many-body effects in correlated materials, it is surface sensitive, i.e. if the material under investigation has some kind of surface reconstruction, charge-rearrangement and is electronically different at the surface as compared to the bulk, ARPES results will not reveal the bulk electronic structure. In case of YBCO, the freshly cleaved surface is a combination of BaO and CuO-chain layers and while the BaO layer is charge neutral, the CuO-chain layer is not and the specific arrangement of the alternating charged layers introduces polar catastrophe, i.e. divergence of electric potential as a function of material thickness along the c -axis (see section 1.5.4 and Ref. [4]). To avoid such a divergence, the system induces charge reconstruction on the cleaved surface and this is the reason behind ARPES experiments always finding YBCO Fermi surface overly overdoped. We have shown that potassium (K) impurities deposited on the surface can tune this charge reconstructed surface back to the bulk, and have been able to observe the evolution of the Fermi surface from the overdoped to the underdoped region [5].

As experimental techniques, we are using some of the most advanced spectroscopic methods available, namely, Angle Resolved Photoemission Spectroscopy (ARPES), X-ray Absorption Spectroscopy (XAS) and Resonant Elastic Soft X-ray Scattering (REXS). Each of these techniques have unique strengths in delivering certain information about the system under investigation. For instance, ARPES and XAS probe the occupied and unoccupied parts of the electronic states respectively and are therefore complementary to each other. Also XAS can provide us information about the element specific local electronic structure of the atoms in the system but not about the long-range ordering taking place. REXS, on the other hand, is a newer technique that has the unique capability of providing direct information regarding the existence of charge/orbital/spin ordering of the valence electrons that make up a very small fraction of the total number of electrons. On top of all these powerful techniques, we are employing density functional theory (DFT) based electronic structure calculation code WIEN2k [6] and cluster-multiplet calculations (XTLS) [7] to model our systems, taking inputs from the experimental results. WIEN2k is based on the full-potential linearized augmented plane wave method (LAPW) and is regarded as one of the most accurate schemes for band structure calculations. Overall, our philosophy has been to apply several of these techniques to a material problem to unravel different facets of the puzzle and to combine all the information towards a unified understanding of the electronic structure of the material.

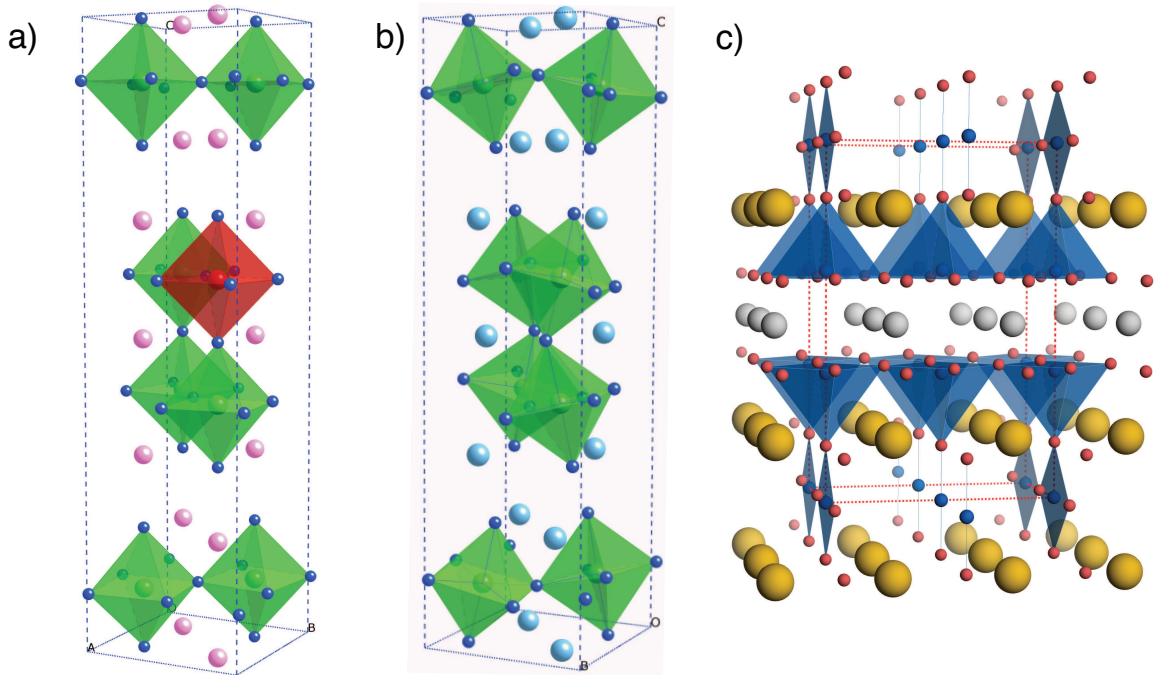


Figure 1.1: Unit cell of (a) Mn doped $\text{Sr}_3\text{Ru}_2\text{O}_7$ where the Mn impurity position is denoted by the red cage. (b) $\text{Ca}_3\text{Ru}_2\text{O}_7$ showing the rotation and tilting of the octahedra. (c) $\text{YBa}_2\text{Cu}_3\text{O}_{7-\delta}$ where $\delta = 0.5$, i.e. alternating full and empty CuO chains.

1.1 Materials and problems

Structurally, the common feature in all the materials investigated in this thesis (Mn doped $\text{Sr}_3\text{Ru}_2\text{O}_7$, $\text{Ca}_3\text{Ru}_2\text{O}_7$ and YBCO) is the perovskite structure with the common feature of oxygen atoms surrounding a Ru or Cu atom. Fig. 1.1 compares the structural unit cells of these compounds that shows, in spite of the similarity of the building blocks, these materials are very sensitive to the constituent elements. For instance, by replacing Sr with Ca one can bring in drastic structural distortion in the material, as shown in Fig. 1.1 (b). As we shall see in the rest of this thesis, the sensitivity of the material properties are not only linked to the crystal structure, but also, and more intimately, linked to the local (Chapter 2), global (Chapter 3) and surface (Chapter 5) electronic structure of the system.

1.1.1 Structural/Lattice distortion

$\text{Sr}_3\text{Ru}_2\text{O}_7$ is a member of a class of materials that can be expressed by the chemical formula: $A_3M_2O_7$ where A is an alkaline/rare-earth metal and B is a transition metal. M occupies the center of an octahedron formed by six oxygen atoms and A is located in the cages formed between these octahedra. A and M together with Oxygen form the perovskite structure that is shown in Fig. 1.1. The values of A and M for the cases of our interest

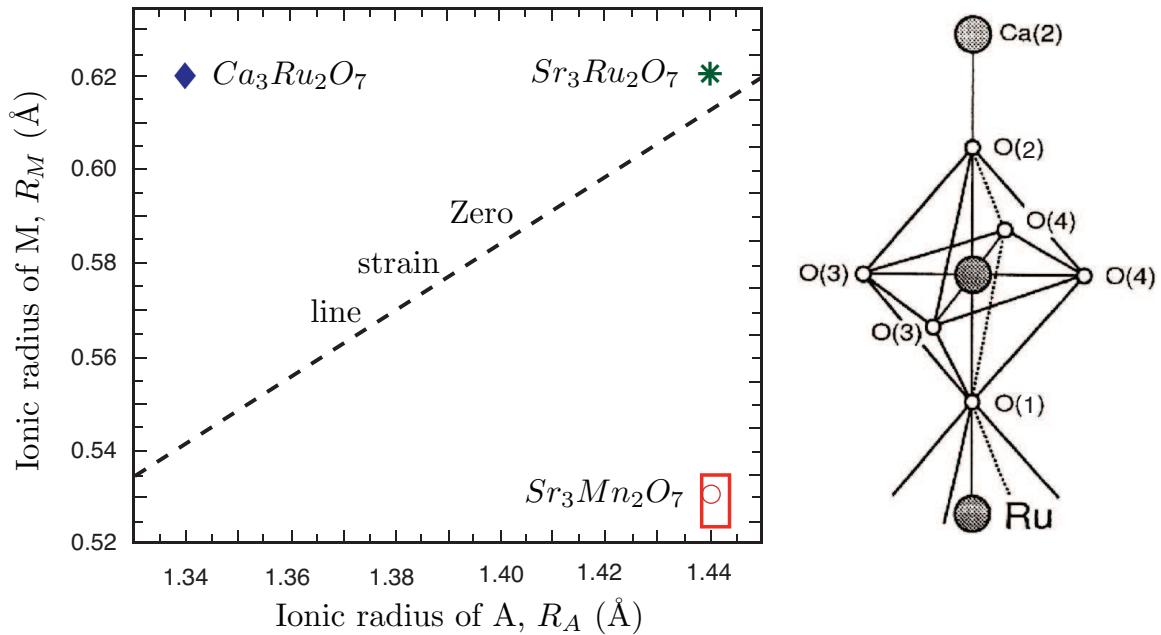


Figure 1.2: (Left) A diagram of R_M vs R_A for $A_3M_2O_7$ type of structure where A and M denote Ca/Sr and Ru/Mn respectively. (Right) Building block of a $A_3M_2O_7$ structure showing inequivalent oxygen sites (taken from [8]).

are tabulated in Table 1.1 following Shannon table [9]. When M and A exactly match the sizes of their cages, they can form a high symmetry structure free of distortion. This special combination of A and M is shown as the “zero strain line” in Fig. 1.2 (a) following Shaked *et al.* [10]. A standard quantity as a measure of distortion is the tolerance factor, defined as $\frac{1}{\sqrt{2}} \frac{R_A + R_O}{R_M + R_O}$ for the compound $A_3M_2O_7$ where R denotes the radius of the corresponding ion (see Table 1.1). If the factor is less than one for these compounds we expect structural distortion. Indeed $Sr_3Ru_2O_7$ is very close to the zero strain line (green star in Fig. 1.2 (a)) and initially it was reported to be tetragonal, with space group $I4/mmm$, similar to Sr_2RuO_4 . However, subsequent measurements revealed ordered rotations of the octahedra due to small incompatibility between the ionic sizes of Sr^{2+} and Ru^{4+} . Shaked *et al.* [10] have shown that the distortions are ordered and they refined the crystal structure into space group $Bbcb$ with a rotation of approximately 7° .

When M is too large compared to A , the network of octahedra is under compression leading to cooperative rotation and tilting (buckling) of the octahedra. This is the case for $Ca_3Ru_2O_7$ (Fig. 1.2 (a) blue diamond symbol in the left corner). On the other hand, in $Sr_3Mn_2O_7$, Mn has 4+ valence and according to Table 1.1, it falls well below the zero strain line (Fig. 1.2 (a), red dot) and hence the structure is susceptible to distortion. However, from Table 1.1 we notice that if Mn valence was 3+ with high spin configuration, the structure would fall very close to the zero strain line near $Sr_3Mn_2O_7$. Hence, one can argue that structural stability may have played a role to determine the special 3+ high spin state

Table 1.1: Approximate ionic radius of participating ions. Taken from “Shannon Effective Ionic Radii Table” [9].

Ion	Ox. state	Coord. number	Spin state	Ionic radius
Mn ³⁺	3	6	LS	0.58
	3	6	HS	0.645
Mn ⁴⁺	4	6		0.53
Ru ⁴⁺	4	6		0.62
Sr ²⁺	2	12		1.44
Ca ²⁺	2	12		1.34
O ²⁻	-2	4		1.38

Table 1.2: Tolerance factor and bond length anisotropy.

Parameter (Å)	Sr ₃ Ru ₂ O ₇ [10] ¹	Sr ₃ Mn ₂ O ₇ [11]	Ca ₃ Ru ₂ O ₇ [8] ²
a/b	3.89	3.789	3.796/3.914
c	20.716	20.064	19.521
Mn/Ru-O(1)	2.012	1.947	1.987
Mn/Ru-O(2)	2.039	1.901	1.989
Mn/Ru-O(3)/O(4)	1.9582	1.895	2.005/1.974
$\frac{\text{Mn/Ru-O(1)}}{\text{Mn/Ru-O(3)/O(4)}}$	1.028	1.028	0.991/1.006
$\frac{\text{Mn/Ru-O(2)}}{\text{Mn/Ru-O(3)/O(4)}}$	1.041	1.003	0.992/1.008
Tolerance factor	0.9941	0.982/1.014/1.041 ³	0.962

of Mn impurities in Sr₃Mn₂O₇ [3] (see Chapter 2 for detail).

As we shall see in the next section, Sr₃Ru₂O₇, Ca₃Ru₂O₇ and Sr₃Mn₂O₇ have very different electronic and magnetic properties and structural distortions play a direct role in defining these properties in a material. There are many coexisting and competing magnetic interactions present in these materials, e.g. super-exchange, double-exchange interactions that are very different in nature. While super-exchange interaction favors antiferromagnetic spin configuration between transition metal ions, double exchange interaction favors ferromagnetic configuration between sites with mixed valency. Their strength critically depends on bond length, bond angle, temperature (energy scale) etc. and hence structural distortions.

¹For undistorted structure. Shaked *et al.* [10] reports subtle distortion in the structure that doubles the volume of the unit cell making $a = b = 5.5006\text{Å}$.

²For undistorted structure. Yoshida *et al.* [8] reports distortion in the structure that doubles the volume of the unit cell making $a = 5.3678, b = 5.5356\text{Å}$. The values in Table 1.2 are distorted lattice values divided by $\sqrt{2}$.

³Tolerance factor for Mn³⁺ high spin state, Mn³⁺ low spin state and Mn⁴⁺ ions at the center of the perovskite respectively.

tions of a certain type can favor one particular type of interaction and define the magnetic property of the system.

1.1.2 Competing ferro and antiferromagnetic fluctuations in ruthenates

Ruthenium oxides are a very important class of compounds that are extremely sensitive to impurities due to the flexible and responsive nature of the delocalized Ru $4d$ orbitals [3]. For example, the radial extend of the $4d$ Ru wave function is significantly larger than that of the Mn $3d$ and even oxygen $2p$ orbitals. This leads to, on the one hand, weaker correlation effects in Ru-oxides than in $3d$ transition metal oxides; on the other hand, to an interesting competition between local and itinerant physics. Impurity doping of a $4d$ system might thus be extremely effective in tuning the macroscopic physical properties, especially when the impurity is a $3d$ transition metal which can enhance the local correlation effects and have a direct impact on the valence, spin, and orbital characteristics of the host material.

Among the $4d$ transition metal oxides (TMO), strontium-ruthenium oxides of the Ruddlesden-Popper type compound series of $\text{Sr}_{n+1}\text{Ru}_n\text{O}_{3n+1}$ with perovskite based crystal structure have been a focus of intensive research due to their diverse and surprising electronic properties. For example, SrRuO_3 is a rare example of an itinerant ferromagnet based on $4d$ electrons [12, 13]. Sr_2RuO_4 is isostructural to the high- T_c compound $\text{La}_{2-x}\text{Ba}_x\text{CuO}_4$ and has the layered perovskite structure with a single RuO_2 plane per formula unit. It is strongly two dimensional, and shows a Pauli like paramagnetic susceptibility [14]. Sr_2RuO_4 is best known for its unconventional superconductivity [14, 15], which is thought to involve spin triplet pairing [16]. Structural distortions in Sr-based ruthenates are either small or absent. Substituting Ca for Sr, however, introduces larger rotations of the Ru-O octahedra since Ca has a much smaller atomic radii than Sr. This causes the bandwidth to narrow and changes to the crystal field splitting. Thus, although Ca and Sr are both divalent cations, the properties of the Ca-based materials are markedly different than Ru-based materials. CaRuO_3 is a paramagnetic metal with a large mass enhancement [17], while Ca_2RuO_4 is an antiferromagnetic insulator [18]. This diversity shows that the ruthenates are characterized by a series of competing instabilities, in particular, both ferro and antiferromagnetic fluctuations are present in this family of compounds.

It is anticipated that being bi-layered, $\text{Sr}_3\text{Ru}_2\text{O}_7$ would possess some intermediate magnetism between the single and infinite layered members of this family that may lead to the possibility of many competing magnetic ground states. Indeed magnetism of $\text{Sr}_3\text{Ru}_2\text{O}_7$ has shown surprising sensitivity to external perturbations such as pressure, magnetic field and classified as a paramagnetic metal on the verge of ferromagnetism. But only after the discovery of field tuned quantum phase transition [19] and metamagnetism [20] in $\text{Sr}_3\text{Ru}_2\text{O}_7$ it is understood that this yet to explore material has all the promises of new and rich magnetic phases that can be tuned with magnetic impurities.

The low temperature transport properties of the bilayer compounds $(\text{Sr}/\text{Ca})_3\text{Ru}_2\text{O}_7$ are similar although magnetic properties are strikingly different. Both materials are metallic and show a resistivity $\sim T^2$ at sufficiently low temperature. Two phase transitions have been identified in $\text{Ca}_3\text{Ru}_2\text{O}_7$: A Néel transition at 56 K and a structural phase transition at 48 K, where the in plane resistivity increases by about 30%, before turning over to a

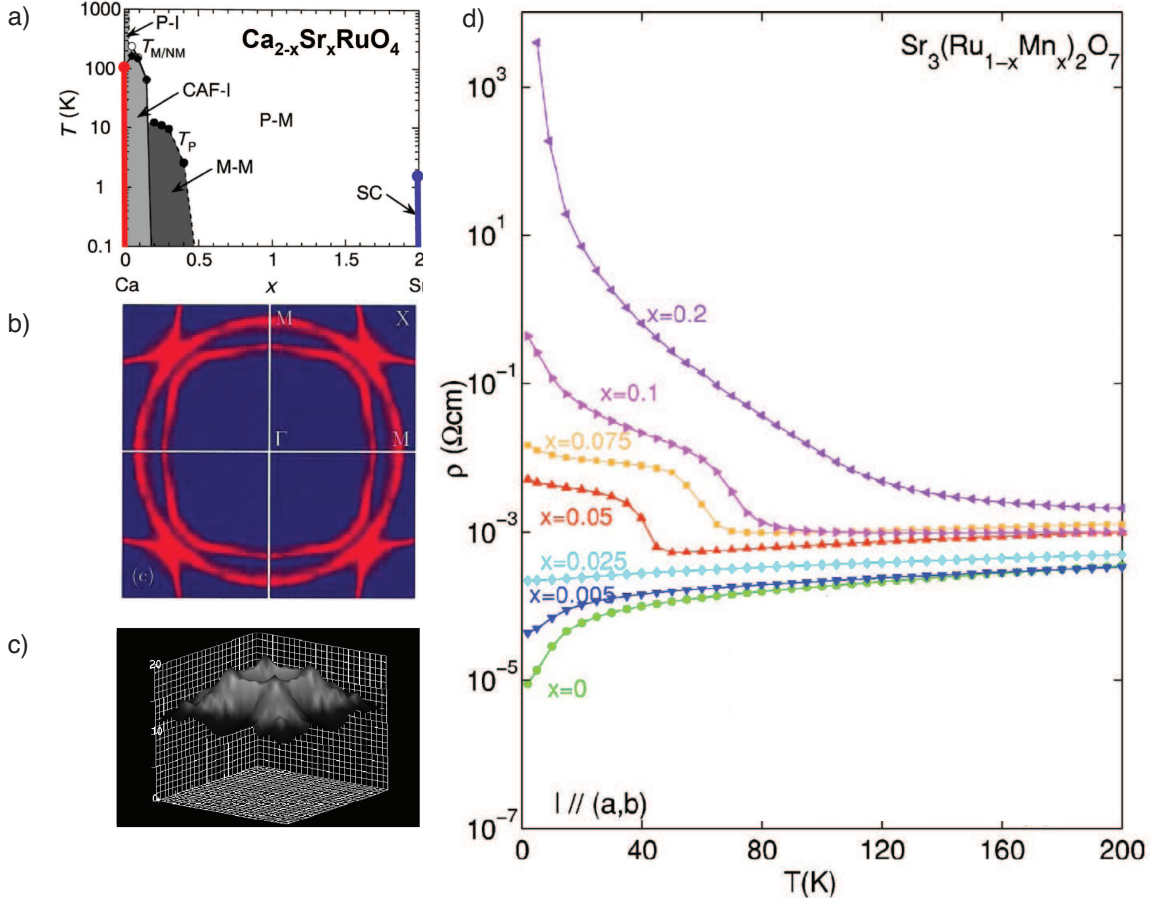


Figure 1.3: (a) Phase diagram of $\text{Ca}_{2-x}\text{Sr}_x\text{RuO}_4$. Taken from Nakatsuji *et al.* [31]. (b) Fermi surface of Sr_2RuO_4 . Taken from Damascelli *et al.* [32]. (c) Map of momentum dependent susceptibility. Taken from [33] (d) Temperature dependence of the resistivity of $\text{Sr}_3(\text{Ru}_{1-x}\text{Mn}_x)_2\text{O}_7$ for different Mn doping x . The electrical current was fed in the ab plane. Taken from Mathieu *et al.* [22].

metallic low-temperature behavior at 30 K [21].

Mathieu *et al.* [22] has successfully grown single crystals of $\text{Sr}_3(\text{Ru}_{1-x}\text{Mn}_x)_2\text{O}_7$ ($0 \leq x \leq 0.2$). The resistivity data as a function of temperature (Fig. 1.3, (d)) show the dramatic effect of Mn doping on the electrical properties of the material. It is clear that Mn impurities are acting as scatterers at low temperature. Mathieu *et al.* proposed a Mott gap formation between $T = 60$ and 80 K for $x > 0.05$. From optical conductivity data the gap was measured to be $\approx 0.2\text{eV}$. It has been concluded that the gap is about an order of magnitude larger than those typically explained by disorder induced Anderson localization effect. Also for 5% Mn doped samples ($x = 0.05$), neutron diffraction data show magnetic peaks suggesting the possibility of an antiferromagnetic ordering below the

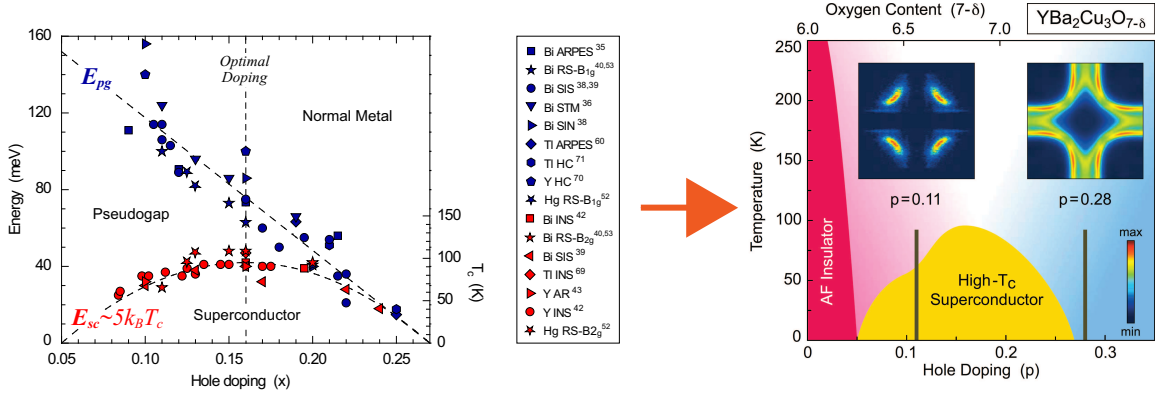


Figure 1.4: Left: Energy scales in cuprates revealed by a combination of experimental techniques on many different cuprate high- T_c compound with doping level spanning the entire phase diagram (for detail, see Chapter 6). Right: Phase diagram of cuprate high- T_c compound YBCO explored by a single experimental technique on a single piece of sample (for detail, see Chapter 5).

metal-to-insulator transition temperature. Structural changes with temperature are smaller compared to other members of the ruthenium oxide family. The contraction of the c axis between $T = 30$ and 275 K for $x = 0.05$ is $\sim 0.1\%$, which is one order of magnitude lower than observed in systems such as Ca_2RuO_4 where structural distortion plays an important role in determining the electronic properties.

1.1.3 Exploring the phase diagram of cuprates in a controlled way

The origin of pseudogap in copper oxide based high temperature superconductors has been a motivation behind an endless stream of experimental and theoretical investigations. As it is discussed in Chapter 6, from the experimental point of view, the main difficulty lies in the fact that there seem to exist two energy scales in the system related to the pseudogap and the superconducting gap. Also, very few cuprate family members can be grown to cover the entire doping phase diagram, i.e. from the Mott insulating state (undoped) to the Fermi liquid state (overdoped), making it difficult to probe these two energy scales in a reliable and consistent fashion. Moreover, as we shall show in Chapter 6, most of the experimental techniques can probe only one energy scale out of the two. This leaves us with an enormous set of data that are essentially incomplete in the sense that there is no single set of experimental data that covers a cuprate compound throughout the whole doping range with a single experimental technique.

On the experimental side, ARPES is perhaps the only experimental technique that can provide a momentum resolved map of the Fermi surface and thereby decisive information regarding the gaps as a function of momentum. However, ARPES is a surface sensitive technique. The Fermi surface of overdoped Tl2201 measured by ARPES [23] and bulk sensitive Angular Magnetoresistance Oscillations (AMRO) [24] agrees very accurately and

provide us reliable momentum resolved data in the overdoped range of the cuprate phase diagram. On the other hand, there are not many reliable measurement on the underdoped side. Form the sample preparation side, YBCO is one of the very few cuprate compounds that can be grown to cover the entire underdoped range of the phase diagram ($p = 0$ to 0.18, see Fig. 1.4) in the very clean limit.

Very recently, Doiron-Leyraud *et al.* [25] reported the first direct evidence for the existence of Fermi surface pockets in the low-energy electronic structure of underdoped $\text{YBa}_2\text{Cu}_3\text{O}_{6.5}$ with high magnetic field quantum oscillation experiments. This result promises to have profound impact on the long-standing debate over the breakdown of the concept of a Fermi surface in the correlated high-temperature superconductors. But quantum oscillation experiments cannot convey any momentum information, i.e. where exactly the small pocket is located on the Fermi surface. This generated intense experimental effort to clarify how relevant this picture is for other cuprate superconductors and also independent confirmation by momentum resolved spectroscopic techniques like ARPES. But all the efforts to probe underdoped YBCO with ARPES have failed due to the notorious surface effect: ARPES always measures an overly overdoped Fermi surface regardless of the actual doping level of the bulk. It was not well understood why that was the case (for further discussions, see section 1.5.4). We have devised a newer method (for detail, see Chapter 5) enabling us to control the doping level of a single piece of YBCO crystal *in situ* and thereby made it possible to measure a reliable momentum resolved Fermi surface map of YBCO for the first time using ARPES across the whole phase diagram [5].

1.2 Experimental techniques

The theory of X-ray scattering, absorption and photoemission can be found in many excellent textbooks and PhD theses (e.g. Ref. [7, 26, 27, 28]) and the following discussion will only touch upon the topics relevant to the studies presented in the thesis.

1.2.1 XAS and X-ray linear dichroism

As an experimental technique, XAS provides an element and site specific probe of local electronic structure. Therefore it is an ideal probe for systems with impurities since element/site-sensitivity of XAS allows us to probe the local environment of impurities or dopants separately from the original atoms.

Chapter 2 presents XAS data at the Mn L-edge where the XAS transition takes place from Mn $2p$ core level to $3d$ valence states. These transitions are schematically presented in Fig. 1.5 (left) and we see two absorptions peaks instead of one is because of the splitting of the $2p$ core level due to strong spin-orbit coupling. It should be noted that the sum of all the $3d$ level orbitals are spherically symmetric, individual orbitals are asymmetric in space. However, as the symmetry of the octahedra around the absorbing $3d$ atom is lowered below cubic (see section 1.5.1), transition to individual d orbital will depend on the orientation of the electric field vector relative to the coordinate system of the crystal.

The term linear dichroism refers to the difference in the XAS spectra when the angle between the sample and linear polarized \mathbf{E} vector of light is changes. Due to the dipole

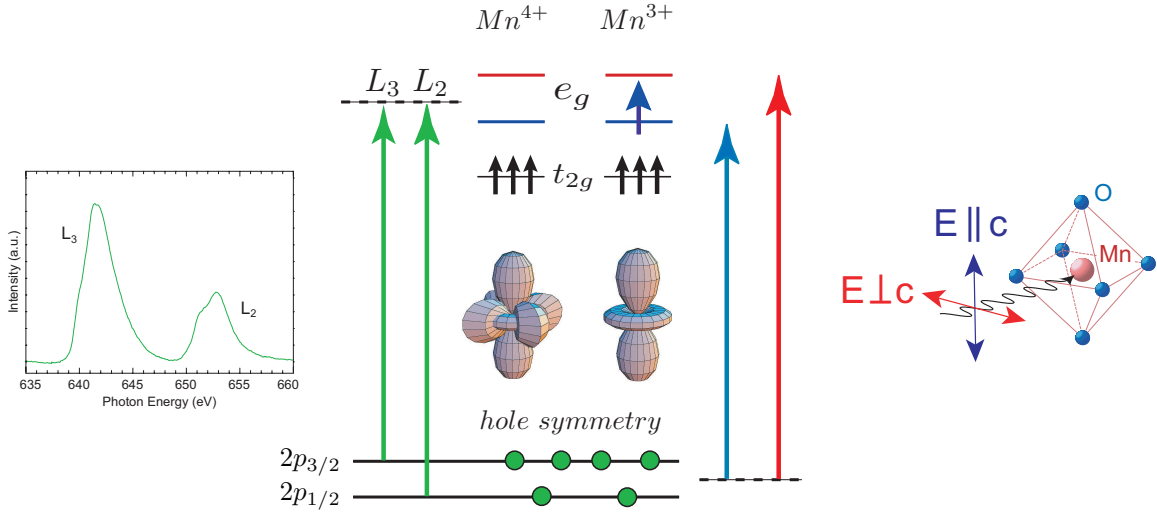


Figure 1.5: (left) Typical XAS spectra obtained from $\text{Sr}_3(\text{Mn}_x\text{Ru}_{1-x})_2\text{O}_7$. (Middle left) Schematic presentation of Mn L-edge XAS transitions ($\text{Mn } 2p \rightarrow 3d$). (Middle) Crystal field levels of Mn 4+ and 3+ together with corresponding e_g hole symmetry. (Middle right) Possible L-edge transitions with in-plane and out-of-plane polarized light

selection rule, in case of Mn L-edge absorption process, in-plane polarized light makes electron transitions possible from core level to the in-plane $3d$ orbital only and the out-of-plane polarized light does the same to the out-of-plane orbital (Fig. 1.5, red and blue arrows). Hence, a difference between the spectra using in-plane and out-of-plane light can provide direct information regarding the population of the orbitals. One has to keep in mind that XAS probes the unoccupied levels and therefore probes the symmetry of the holes (shown in the Fig. 1.5, middle).

The easiest way to visualize the polarization dependence of linear dichroism is through the “search light effect” [28] that can be stated as follows. In an XAS experiment electrons are excited from a core level to empty valence states. With linear polarized x-ray, the electric field vector acts like a search light for the direction of the maximum and minimum number of empty valence states, i.e. the transition intensity is directly proportional to the number of empty valence states in the direction of the field vector. Hence, the angular dependence of the XAS intensity on electric field vector is determined by the spatial distribution of the empty valence states. A striking demonstration of linear dichroism at the Cu L-edge can be found in Ref. [29]. These ideas has been applied in Chapter 2 to explore the orbital symmetry of the Mn $3d$ valence electrons. The $L_{2,3}$ -edge lineshape of the XAS depends on the distribution of the multiplets that has been calculated with XTLS 8.0 written by A. Tanaka [30]. A detail description of the physics and theory behind cluster multiplet calculations can be found in Ref. [7].

1.2.2 Bragg scattering

Let us begin our discussion with a brief description of the scattering process of light (electromagnetic wave or photon) with a single electron (i.e. quantum of charge). The ability of an electron to scatter an X-ray is expressed in terms of *scattering length* that is basically the amplitude of the ratio of the magnitude of the radiated to incident field. This is typically denoted by r_0 and the Thomson scattering length is $r_0 = \left(\frac{e^2}{4\pi\epsilon_0 mc^2}\right) = 2.82 \times 10^{-5} \text{ \AA}$. Let us now look at the expression for the scattering length of an atom or *atomic form factor* that describes the scattering amplitude from a homogeneous charge density:

$$-r_0 f^0(\mathbf{Q}) = -r_0 \int \rho(\mathbf{r}) e^{i\mathbf{Q}\cdot\mathbf{r}} d\mathbf{r} \quad (1.1)$$

where \mathbf{Q} is the momentum transfer. Of course, an atom is not a homogeneous charge distribution. Atomic electrons have discrete energy levels and the electrons that are less tightly bound (L, M shell corresponding to principle quantum number, $n = 1, 2$ respectively) will be able to respond to incoming field quite closely. However, electrons in the core levels (e.g. K shell corresponding to $n = 1$) are much more tightly bound and if the incident X-ray energy is much less than the binding energy of the core level electrons, the response will be much less. This will reduce the overall scattering length of the system by the amount, say f' . Moreover, the bound states of the electrons can be treated as harmonic oscillators and the response of the electrons will have a phase lag with the incident X-ray. Hence we need to introduce a dissipative term if'' in the atomic form factor that becomes:

$$f(\mathbf{Q}, \hbar\omega) = f^0(\mathbf{Q}) + f'(\hbar\omega) + if''(\hbar\omega) \quad (1.2)$$

In the soft X-ray regime or for scattering in the forward direction where the momentum transfer is small, atomic form factor can be approximated as $\int \rho(\mathbf{r}) d\mathbf{r} \sim Z$. Then Eq. 1.2 becomes

$$f(\omega) = Z + f'(\hbar\omega) + if''(\hbar\omega) = F_1(\hbar\omega) + iF_2(\hbar\omega) \quad (1.3)$$

F_1 and F_2 s are known as *Henke-Gullikson* atomic factors that can be found from tables. The scattering length of a molecule will be

$$F^{mol}(\mathbf{Q}, \omega) = \sum_{\mathbf{r}_j} f_j(\mathbf{Q}, \omega) e^{i\mathbf{Q}\cdot\mathbf{r}_j} \quad (1.4)$$

where atoms in the molecule are indexed by j and $f_j(\mathbf{Q})$ represents the atomic form factor of the j th atom. Similarly, for a crystal (a lattice structure with a molecule in each site) we can use the following indexing: \mathbf{R}_n are the lattice vectors that define the lattice and \mathbf{r}_j are the position of the atoms in the molecule with respect to any one particular lattice site. Hence, the position of any atom in the crystal is given by $\mathbf{R}_n + \mathbf{r}_j$ and the form/structure

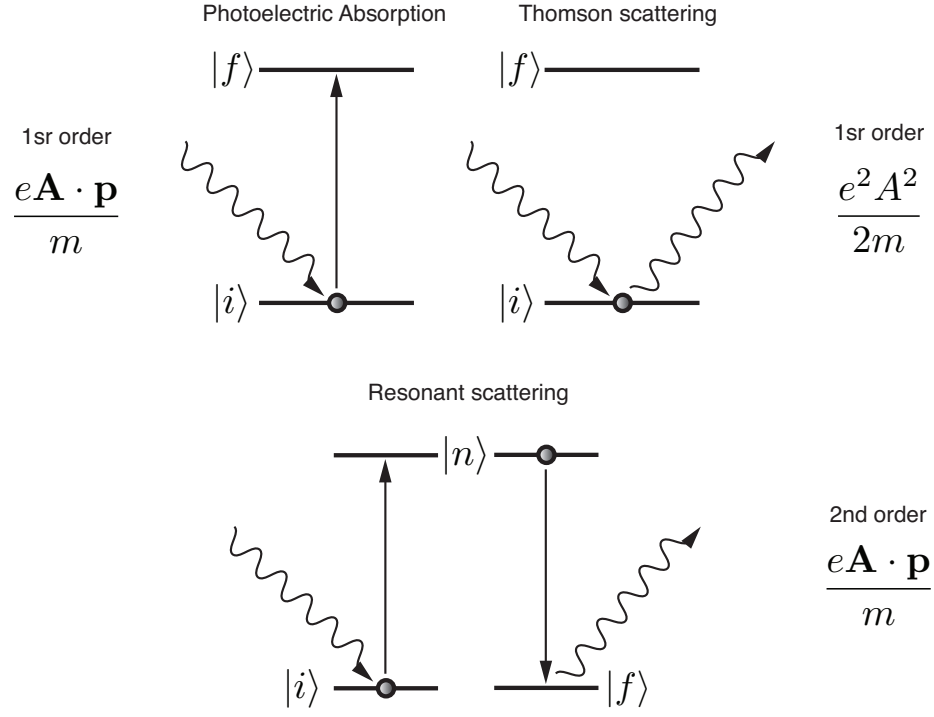


Figure 1.6: Schematic diagrams describing the electronic transitions involved with the X-ray absorption, Thomson scattering and resonant X-ray scattering processes.

factor for the crystal is

$$F^{crystal}(\mathbf{Q}, \omega) = \underbrace{\sum_{\mathbf{r}_j} f_j(\mathbf{Q}, \omega) e^{i\mathbf{Q} \cdot \mathbf{r}_j}}_{\text{Unit cell struc factor}} \underbrace{\sum_{\mathbf{R}_n} e^{i\mathbf{Q} \cdot \mathbf{R}_n}}_{\text{Lattice sum}} \quad (1.5)$$

and $F^{crystal}(\mathbf{Q}, \omega)$ is nonzero if and only if $\mathbf{Q} = \mathbf{G}$ which is of course the Laue or, equivalently, Bragg condition. We can use Eqn. 1.5 to explain some of the results in Chapter 3, shown in Section 7.3.

1.2.3 REXS: a combination of XAS and scattering

At this point, we can take a brief look at the quantum mechanical description of the X-ray absorption and resonant scattering process. We start from the transition rate probability, W , that can be expressed in first order perturbation theory as

$$W = \frac{2\pi}{\hbar} |\langle f | \mathcal{H}_I | i \rangle|^2 \rho(\epsilon_f) \quad (1.6)$$

where $|i\rangle$ and $|f\rangle$ are the initial and the final states of the combined X-ray photon and the interacting electron and $\rho(\epsilon_f)$ is the density of final states. The Hamiltonian $\mathcal{H}_{\mathcal{I}}$ defines the interaction between the X-ray photon and the electron that has the form

$$\mathcal{H}_{\mathcal{I}} = \frac{e\mathbf{A} \cdot \mathbf{p}}{m} + \frac{e^2 A^2}{2m} \quad (1.7)$$

The first term in $\mathcal{H}_{\mathcal{I}}$ is linear in \mathbf{A} that means it can only create or annihilate a photon and gives rise to photoelectric absorption (Fig. 1.6, top left). The second term, on the other hand, is quadratic, meaning that it can first annihilate and then create a photon and, therefore, describes elastic Thomson scattering process (Fig. 1.6, top right). To obtain the resonant scattering term, we need to apply second order perturbation theory where the transition probability is given by

$$W = \frac{2\pi}{\hbar} \left| \langle f | \mathcal{H}_{\mathcal{I}} | i \rangle + \sum_{n=1}^{\infty} \frac{\langle f | \mathcal{H}_{\mathcal{I}} | n \rangle \langle n | \mathcal{H}_{\mathcal{I}} | i \rangle}{E_i - E_n - \hbar\omega} \right|^2 \rho(\epsilon_f) \quad (1.8)$$

Hence, we can see that when $\hbar\omega = E_i - E_n$, i.e. at the absorption edges the scattering intensity is greatly enhanced.

X-ray absorption can be described in terms of the linear absorption coefficient $m = \rho\sigma$ where ρ is the atomic mass density and σ is the absorption cross section. For normal angle of incidence the photon intensity decreases exponentially as a function of depth: $I(z) = I_0 e^{m(\omega)z}$, where I_0 is the incident intensity. The imaginary part of the atomic form factor, f'' in Eqn. 1.2 can be related to the absorption cross section with the following relation [44]:

$$-r_0 f''(\omega) = \frac{k}{4\pi} \sigma(\omega) \quad (1.9)$$

This relationship can be summarized more transparently by expressing the intensities of REXS and XAS in the following manner [34]:

$$I_{REXS}(\mathbf{Q}, \omega) \propto |\epsilon' \cdot F(\mathbf{Q}, \omega) \cdot \epsilon|^2 \quad (1.10)$$

$$I_{XAS}(\omega) \propto |Im[\epsilon \cdot F(\mathbf{Q} = \mathbf{0}, \omega) \cdot \epsilon]|^2 \quad (1.11)$$

where ϵ and ϵ' define the polarization vectors of the incoming and scattered beams. I_{REXS} and I_{XAS} are related by the optical theorem [35] and the real and the imaginary part of $F(\mathbf{Q}, \omega)$ are related by the Kramers-Kronig transformation in the frequency space. It is also important to note that I_{REXS} depends on both the incoming and outgoing polarization of light and hence it is a 3×3 matrix. On the other hand, I_{XAS} depends only on the polarization of the incoming light and hence can be described by the diagonal terms of the tensor.

In an x-ray absorption process, the time scale for creating a core hole is of the order of 10^{-20} s while the rearrangement of the valence electrons in the presence of the core hole (screening) is of the order of $\sim 10^{-16}$ to 10^{-15} s. The lifetime of the core hole is determined by all these relaxation processes and is about 10^{-15} seconds before it decays via radiative or

non-radiative decay channels. For the lighter elements ($Z < 30$) the dominant process is the non-radiative Auger process and the larger Z systems relaxes predominantly by emission of fluorescence photons [38]. Where as in a REXS one does not explicitly create any core hole. The life time of a core hole (τ) in the XAS process is linked to the uncertainty in the energy of the core hole (Γ) via the Heisenberg uncertainty principal. A lifetime of 1fs implies a lifetime broadening of 0.1 eV that is the intrinsic resolution limit of XAS.

1.2.4 ARPES

Angle Resolved Photo-Emission Spectroscopy is based on the photoelectric effect where light is shone on the material knocks electrons out of the material surface. The great success of ARPES in the study of solids is a testament to the capacity of this technique to yield direct access to the energy and momentum of the occupied electronic states. Excellent reviews of ARPES on cuprate superconductors are available, e.g. Ref. [39, 40, 42, 41]. ARPES measurements have a simple interpretation within the framework of one-electron band theory, i.e., it maps the band structure of the material and, therefore, the Fermi surface. On top of this ARPES has emerged as one of the most effective technique to study many-body interactions in layered strongly correlated electron systems due to its unique capability to directly measure the single particle spectral function [40].

The intensity in an ARPES experiment corresponds to the electron removal part of the spectral function modulated by transition matrix elements:

$$I(\mathbf{k}, \omega) = I_0(\mathbf{k}, \nu, \mathbf{A})f(\omega)A(\mathbf{k}, \omega) \quad (1.12)$$

where \mathbf{k} is the in-plane electron momentum, \mathbf{A} is the electromagnetic vector potential, ω is the electron energy with respect to Fermi level, $I_0(\mathbf{k}, \nu, \mathbf{A})$ is proportional to the transition matrix element and $A(\mathbf{k}, \omega)$ is the spectral function. Since the spectral function is directly related to *self energy* which in turn contains all the interactions present in a system, the analysis of ARPES spectra can provide us with direct information about the dominant interactions present in a system as a function of temperature. The presence of the Fermi function factor in the intensity ensures that ARPES can probe only the states below the Fermi energy. For non-interacting fermions, the spectral function is a delta function. However, in Fermi liquids, the spectral functions is renormalized by a factor Z , quasiparticle weight and the remainder of the spectral weight is transferred to an incoherent background. Hence ARPES can map the occupied part of the band structure of a solid and therefore the Fermi surface and, at the same time, can provide us valuable information regarding correlation effects in the system.

1.3 Experimental conditions

Here we discuss the details of XAS, REXS and ARPES experiments on Mn doped $\text{Sr}_3\text{Ru}_2\text{O}_7$ together with the sample preparation process. Details of the ARPES experiments YBCO and $\text{Ca}_3\text{Ru}_2\text{O}_7$ are described in Chapter 5 and 4.

In XAS, there are two commonly possible way to measures the spectra, total electron

yield method (TEY) and total fluorescence yield method (TFY). As mentioned before, in the photoelectric absorption process (Fig. 1.6, top left) a photon is absorbed and an electron is ejected from this atom. The remaining hole can be filled by two dominating processes [26]. In the fluorescent x-ray emission process, one of the outer shell electron fills the hole and the atom emits a photon. One gets the TFY XAS spectra by measuring this emitted photon. On the other hand the outer shell electron can fill the core hole and in the process transfer the energy to another outer shell electron and thereby eject it from the atom, a process known as Auger decay. The TEY method of measuring XAS relies on Auger decay channel of the excited electron [38]. Spectra measured in the TEY method is surface sensitive since the ejected electron cannot escape the solid if it is too deep inside the material. On the other hand, it is much easier for photons to escape the material and hence spectra measured in the TFY method much less surface sensitive than TEY. However, TFY data contains more noise than TEY. In Chapter 2, all the XAS measurements presented are done in the TEY method. In spite of choosing TEY as our measurement method, we do not expect the surface contamination to affect our measurements since the samples were cleaved in situ in a vacuum of $< 10^{-9}$ Torr. Also, simultaneous TFY measurements were done to compare TEY data with more bulk sensitive TFY data. On the other hand REXS, is a combination of XAS and X-ray Diffraction where one always measures outgoing photons and hence it is much more bulk sensitive than TEY method of XAS.

Sample preparation: High-quality single crystals of $\text{Sr}_3(\text{Ru}_{1-x}\text{Mn}_x)_2\text{O}_7$ (with $x = 0.05, 0.1, \text{ and } 0.2$) were grown by the floating zone technique. As described elsewhere [22], the samples were characterized by inductively coupled plasma analysis (in order to check the Mn composition x), x-ray and neutron diffraction, heat capacity, magnetometry, and DC electric transport. The temperature dependent in-plane resistivity, here reproduced from Ref. [22], was measured with a standard four-probe method on a PPMS6000 system. For all Mn doping levels, the crystals cleave easily along the ab -plane in between two adjacent SrO layers, resulting in extremely flat mirror-like surfaces similar to pure Sr_2RuO_4 and $\text{Sr}_3\text{Ru}_2\text{O}_7$.

XAS experiments: X-ray Absorption Spectroscopy (XAS) measurements on $\text{Sr}_3(\text{Ru}_{1-x}\text{Mn}_x)_2\text{O}_7$ single crystals at various temperatures were performed at the National Synchrotron Radiation Research Center (NSRRC) in Taiwan. The Mn and oxygen edge measurements were performed on the Dragon Beamline, while the Ru edge data were recorded on Beamline 15B. In both cases, the XAS spectra were acquired in total electron-yield mode by measuring the sample drain current as a function of the incident photon energy. We used larger cylindrical single crystals (with a radius and height of ~ 3 and 5 mm, respectively), with c -axis perpendicular to the axis of the cylinder. These samples were cut in situ with a knife along the ac -plane, which is also perpendicular to the cylinder axis, at a pressure of 3×10^{-10} torr; no surface aging was observed upon cycling the temperature between 20 and 300K. During the linear dichroism experiments, we utilized the very convenient geometries of the 5% and 10% doped samples by rotating the sample (or the wedge in case of undoped samples that was thin along the c -axis direction) about the direction of incident photon beam, which was linearly polarized in the horizontal plane, so as to measure XAS spectra with $E \parallel c$ and $E \perp c$. This enabled us to obtain linear dichroism

spectra from which experimental artifacts related to the difference in the optical path and to the probing area have been eliminated. The photon energy resolution was 0.3 eV and the degree of linear polarization was $\approx 98\%$.

In order to rule out the presence of ferromagnetism in the low temperature insulating phase of Mn doped $\text{Sr}_3\text{Ru}_2\text{O}_7$, we have performed magnetic circular dichroism experiments in an applied field of 0.5 Tesla at 20 K, with left and right circularly-polarized photons impinging on the samples at normal incidence. The XAS data were normalized dividing the drain current by the beam intensity I_0 , i.e. the photocurrent measured as a function of photon energy on a metal grid interposed in the beam; for the direct comparison as a function of Mn doping, the spectra were also scaled by the nominal Mn content. The absolute energy calibration was obtained from the parallel measurement of a reference MnO sample and the knowledge of its L_3 edge absolute peak position [43].

REXS experiments: RSXS measurements were performed at beam line 8.0.1 at ALS in Berkeley (Mn L -edges) and at beam line KMC- 1 at BESSY in Berlin (Ru L -edges). The measurements were done with π -polarized linear light (see Fig. 1.7). To measure the $(\frac{1}{4}, \frac{1}{4}, 0)$ superlattice diffraction spot, we prepared a (1,1,0) sample surface (not a nature cleavage plane) by cutting the sample with a diamond saw and polishing the surface with diamond paste and alumina. At ALS, due to motorized x and z motion, it was possible to image the surface of the (110) plane at the Mn L-edge and we found the signal profile quite homogeneous throughout the sample surface. On top of that, to make sure that our data does not get affected by any inhomogeneity of the surface, we made sure that we stay in the same spot with the photon beam when we rotated the azimuthal (ϕ) angle. This was done by taking series of images at the Mn L-edge with zx motion at different azimuthal angle to track our region of interest on the (110) sample. During the Ru L-edge measurements at KMC-1 at BESSY, we used an Avalanche Photo Diode (APD) to cut the intensity due to the 4th harmonic.

ARPES experiments: ARPES measurements on $\text{Ca}_3\text{Ru}_2\text{O}_7$ were carried out at the Stanford Synchrotron Radiation Laboratory (SSRL) on the Normal Incidence Monochromator Beamline 5-4. The data were measured with linearly-polarized 28 eV photons and a Scienta SES-200 electron analyzer in angle-resolved mode. Energy and angular resolutions were set to 14meV and 0.3° (i.e., 1.5% of the Brillouin zone). $\text{Sr}_3(\text{Ru}_{1-x}\text{Mn}_x)_2\text{O}_7$ thin platelets were oriented by Laue diffraction prior to the experiments, and then cleaved in situ at a base pressure better than 5×10^{-11} torr. The temperature was cycled between 10 and 100K, without leading to any noticeable aging of the samples' surface. In order to compensate for the angular response of the analyzer, EDC's in a single cut were normalized against those measured on an amorphous Au film (10K Au data were also used for the absolute energy calibration). Different cuts were then normalized with respect to each other on the basis of the spectral weight from above the chemical potential, integrated in both momentum and energy.

Details of the ARPES experiments on YBCO can be found in Chapter 5.

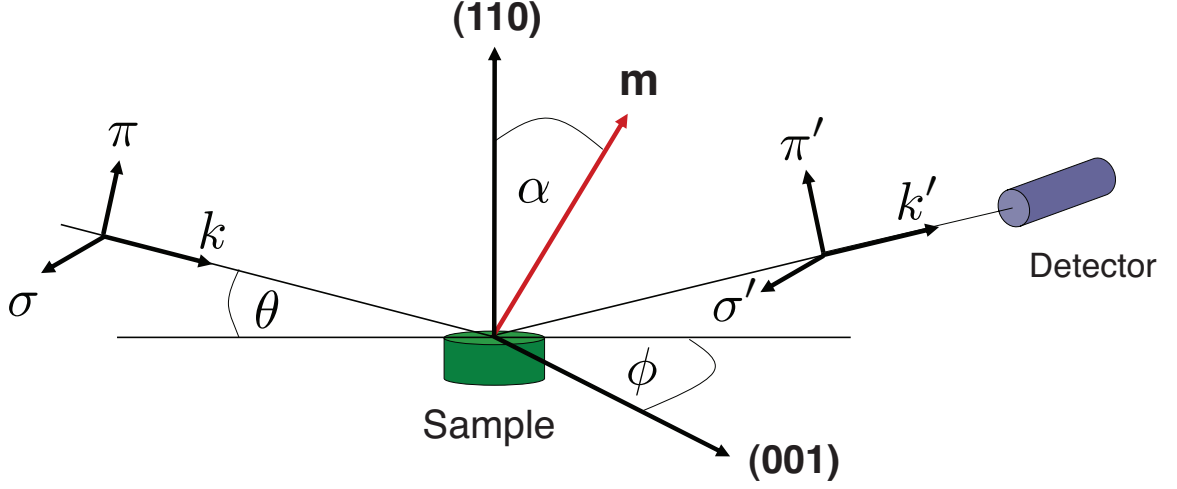


Figure 1.7: REXS geometry defining the π and σ polarization and angles, θ , α , ϕ .

1.4 Angular dependence of magnetic scattering intensity

For an electric 2^L -pole (EL) resonance in a magnetic ion, the resonant contribution to the coherent scattering length is [45]:

$$f_{EL}(\omega) = \frac{4\pi}{|k|} f_D \sum_{M=-L}^L [\hat{\epsilon}'^* \cdot \mathbf{Y}_{LM}(\hat{\mathbf{k}}') \mathbf{Y}_{LM}^*(\hat{\mathbf{k}}) \cdot \hat{\epsilon}] F_{LM}(\omega) \quad (1.13)$$

In Eq. 1.13 $\mathbf{Y}_{LM}(\hat{\mathbf{k}})$ are vector spherical harmonics, f_D is the Debye-Waller factor that takes into account the attenuation of x-ray scattering caused by thermal motion, \mathbf{k} , \mathbf{k}' are the wavevectors and ϵ , ϵ' are the polarization vectors of the incoming and scattered beams, respectively. F_{LM} determines the strength of the resonance that depends on the atomic properties of the scattering ion is defined in Ref. [46].

It is useful to express the vector spherical harmonics in the scattering length (Eqn. 1.13) as a function of the polarization vectors ϵ , ϵ' of the incoming and the scattered beams:

$$f_{E1}(\omega) = [(\hat{\epsilon}' \cdot \hat{\epsilon})F^{(0)} - i(\hat{\epsilon}' \times \hat{\epsilon}) \cdot \hat{m}F^{(1)} + (\hat{\epsilon}' \cdot \hat{m})(\hat{\epsilon} \cdot \hat{m})F^{(2)}] \quad (1.14)$$

where

$$F^{(0)} = \frac{3}{4k} [F_{11} + F_{1-1}] \quad (1.15)$$

$$F^{(1)} = \frac{3}{4k} [F_{11} - F_{1-1}] \quad (1.16)$$

$$F^{(2)} = \frac{3}{4k} [2F_{10} - F_{11} - F_{1-1}] \quad (1.17)$$

and $\hat{\mathbf{m}}$ is a unit vector denoting the direction of the local magnetic moment. We can simplify

the expression of the scattering length with the use of 2×2 matrices with basis spanned by component parallel (π) and perpendicular (σ) to the scattering plane, as suggested by Ref. [46]:

$$\begin{pmatrix} \sigma'\sigma & \sigma'\pi \\ \pi'\sigma & \pi'\pi \end{pmatrix}$$

where the first and the second factor in each element denotes outgoing and incoming light polarization. With this basis, the scattering length for electric dipole scattering can be expressed as:

$$f_{E1} = F^{(0)} \begin{pmatrix} 1 & 0 \\ 0 & \cos 2\theta \end{pmatrix} - iF^{(1)} \begin{pmatrix} 0 & m_1 \cos \theta + m_3 \sin \theta \\ m_3 \sin \theta - m_1 \cos \theta & -m_2 \sin 2\theta \end{pmatrix} \quad (1.18)$$

$$+ F^{(2)} \begin{pmatrix} m_2^2 & -m_2(m_1 \sin \theta - m_3 \cos \theta) \\ m_2(m_1 \sin \theta + m_3 \cos \theta) & -\cos^2 \theta (m_1^2 \tan^2 \theta + m_3^2) \end{pmatrix}$$

where θ is the scattering angle and m_1 , m_2 and m_3 are the components of $\hat{\mathbf{m}}$ along the sample axes:

$$\begin{aligned} m_1 &= \sin \alpha \cos \phi \\ m_2 &= \sin \alpha \sin \phi \\ m_3 &= -\cos \alpha \end{aligned} \quad (1.19)$$

Eqn. 1.19 explicitly shows the angular dependence of the magnetic scattering intensity (dipole).

As an example of the azimuthal angle (ϕ) dependence of the scattered intensity, we will present the detail calculations behind Fig. 3.2 of Chapter 3. We can start from Eqn. 1.5:

$$I_{\mu\nu} = \left| \sum_j e^{i\mathbf{Q}\cdot\mathbf{R}_j} f_{\uparrow,\downarrow}^{\mu\nu} \right|^2 \quad (1.20)$$

where μ and ν are denoting the polarizations of the incoming and diffracted light, respectively. f_{\uparrow} and f_{\downarrow} are the scattering lengths of the \uparrow and \downarrow spin directions, respectively. For a 4×4 magnetic unit cell

$$\begin{array}{cccc} \downarrow & \uparrow & \uparrow & \downarrow \\ \downarrow & \downarrow & \uparrow & \uparrow \\ \uparrow & \downarrow & \downarrow & \uparrow \\ \uparrow & \uparrow & \downarrow & \downarrow \end{array}$$

and $\mathbf{Q} = (\frac{1}{4}, \frac{1}{4}, 0)$, Eqn. 1.20 becomes:

$$I_{\mu\nu} = \left| 4(1+i)(f_{\uparrow}^{\mu\nu} - f_{\downarrow}^{\mu\nu}) \right|^2 \quad (1.21)$$

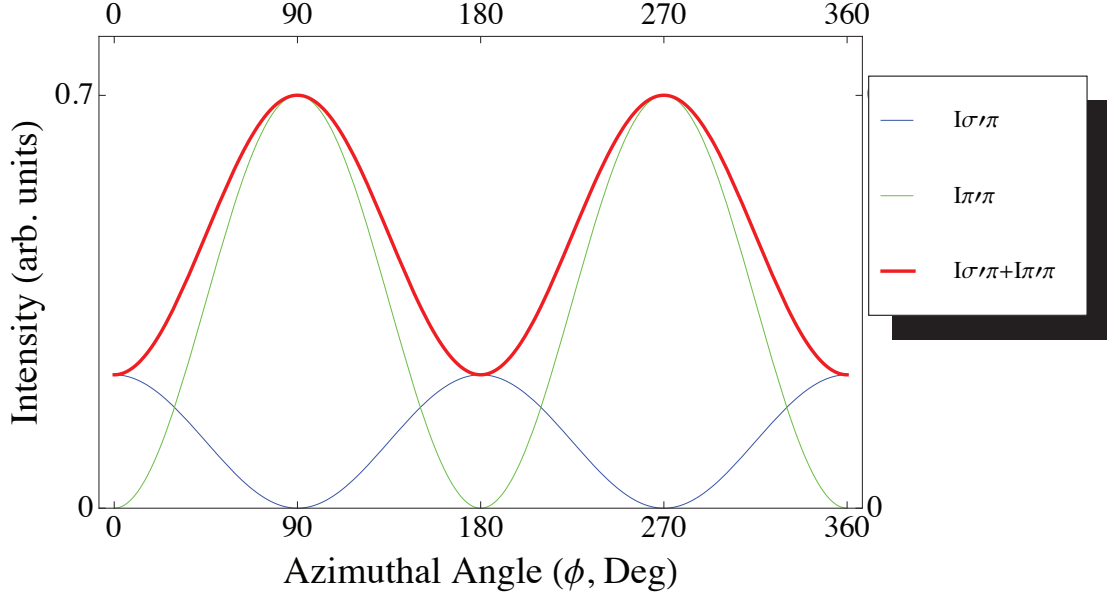


Figure 1.8: Azimuthal angle dependence at the Mn edge of the integrated intensity of the $(\frac{1}{4}, \frac{1}{4}, 0)$ resonant diffraction peak at the $\sigma'\pi$ channel ($I_{\sigma'\pi} = |f_{\uparrow}^{\sigma'\pi} - f_{\downarrow}^{\sigma'\pi}|^2$, blue), $\pi'\pi$ channel ($I_{\pi'\pi} = |f_{\uparrow}^{\pi'\pi} - f_{\downarrow}^{\pi'\pi}|^2$, green). With the lack of an analyzer on the scattered photon side, we could only measure the total intensity, $I_{\sigma'\pi} + I_{\pi'\pi}$, shown by the solid red line (see Chapter 3 for detail).

which has the following angular dependence:

$$f_{\uparrow} - f_{\downarrow} = \begin{pmatrix} f_{\uparrow}^{\sigma'\sigma} - f_{\downarrow}^{\sigma'\sigma} & f_{\uparrow}^{\sigma'\pi} - f_{\downarrow}^{\sigma'\pi} \\ f_{\uparrow}^{\pi'\sigma} - f_{\downarrow}^{\pi'\sigma} & f_{\uparrow}^{\pi'\pi} - f_{\downarrow}^{\pi'\pi} \end{pmatrix} = \begin{pmatrix} 0 & m_1 \cos \theta + m_3 \sin \theta \\ -m_1 \cos \theta + m_3 \sin \theta & -m_2 \sin 2\theta \end{pmatrix}$$

which is the second term of Eqn. 1.19.

Plugging in $\theta = 61.6^\circ$ for the Mn L-edge and $\alpha = 0^\circ$ when magnetic moments are along the c -axis, we can plot the azimuthal (ϕ) angular dependence of the $(\frac{1}{4}, \frac{1}{4}, 0)$ diffraction spot intensity, $I_{\mu\nu}$ for incoming π -polarized light, shown in Fig. 1.8 (Red line).

1.5 Few concepts

This section combines the theoretical ideas presented in the previous sections to the material problems we are considering. It also serves as an introduction to some of the key concepts presented in the later chapters. The first section deals with the valence and orbital hierarchy of the elements present in Mn doped $\text{Sr}_3\text{Ru}_2\text{O}_7$ (schematically represented in Fig. 1.9). The second part presents the model of Mn impurity e_g level hybridization with the environment, used extensively in Chapter 2 (Fig. 1.10). The next section presents the concept behind

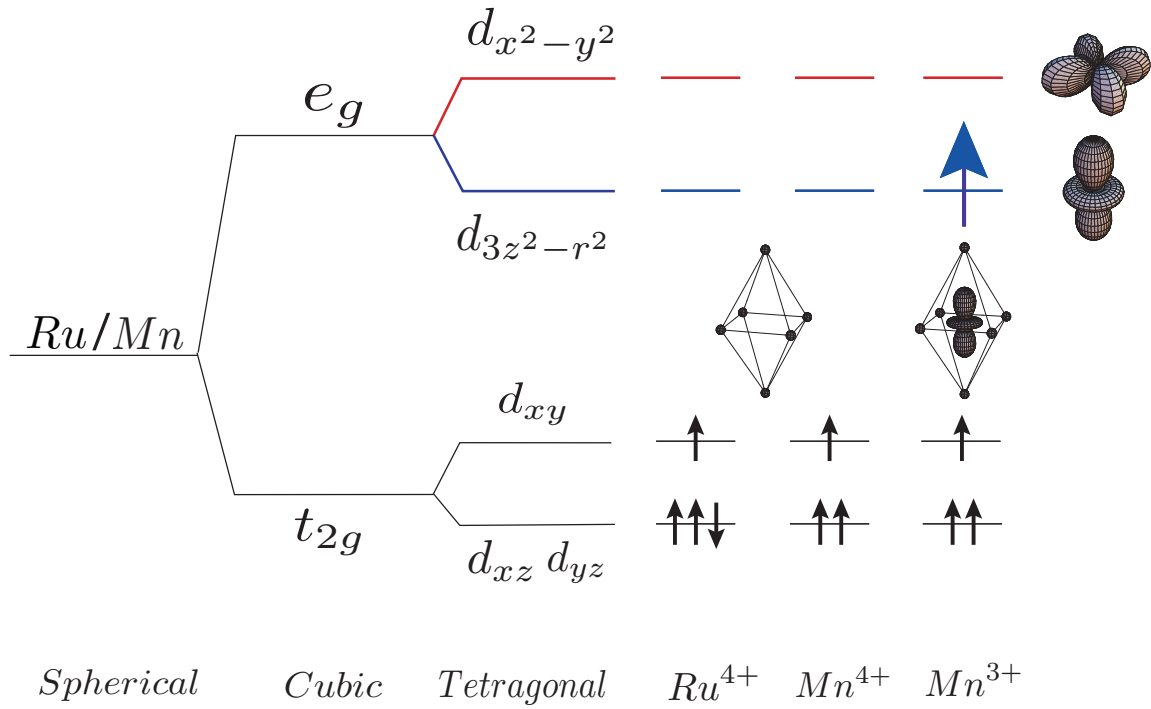


Figure 1.9: (Left) Schematic presentation of crystal field splitting of transition metal d level when the symmetry is reduced from spherical to tetragonal. (Middle) electron population of the levels for Ru and Mn $4+$ and Mn $3+$. (Top right) spatial symmetry of the e_g levels.

observing structurally forbidden magnetic diffraction spots with RSXS and explores the possibility to observe magnetic reflections from a dilute random lattice or lattice liquid (Fig. 1.11, discussed in detail in Chapter 3). We conclude with a discussion of polar surfaces in connection with oxide heterostructures and YBCO (Figs. 1.13 and 1.14), a concept used in Chapter 5.

1.5.1 Orbital hierarchy and Jahn-Teller distortion

Both Ru and Mn have d valence shell that has 5 orbitals. These 5 orbitals are degenerate in terms of energy when the atoms are in a spherically symmetric potential (Fig. 1.9) and this degeneracy is lifted when the symmetry is reduced. Fig. 1.9 left hand side show the splitting for cubic and tetragonal symmetry. Since $Sr_3Ru_2O_7$ crystal structure is known to have tetragonal symmetry (oxygen cage elongated along the c -axis) [10], we can expect the situation shown in the middle of the figure 1.9.

The valence of Ru in $Sr_3(Mn_xRu_{1-x})_2O_7$ is $4+$ and when a Mn impurity replaces a Ru atom, it should also have a $4+$ valence. Fig. 1.9 (right hand side) shows Ru^{4+} having 3 $4d$ electrons, all sharing the t_{2g} orbitals since $4d$ levels are very delocalized and covalent

compared to $3ds$. The covalent $4d$ levels therefore have much larger crystal field level splitting than Hund's coupling can overcome, i.e. energy gain by maximizing the total spin is less than the crystal field level splitting. Hence, all 4 electrons have to share the t_{2g} orbitals with a low spin configuration (total spin $S=1$). In case of Mn^{4+} , there is only 3 $3d$ electrons and not having any orbital degrees of freedom, they will share the 3 t_{2g} levels. However, just in case Mn atoms take a $3+$ valence instead of the expected $4+$, there will be an extra (4th) $3d$ electron. Since $3d$ levels are more localized, Hund's coupling is much stronger than crystal field in this case, and the system gains more energy by maximizing the total spin and the 4th electron must go to the e_g level instead of t_{2g} . As there are two e_g orbitals, this brings in orbitals degrees of freedom to the problem.

At this point, the following question arises: out of the two e_g orbitals, in-plane ($x^2 - y^2$ symmetry) and out-of-plane ($3z^2 - r^2$ symmetry), where would this 4th $3d$ electron go to? This can be answered intuitively using the concept of Jahn-Teller distortion. The cage made of six oxygen around each Ru is elongated along the c -axis [10] and, therefore, there is more room for the 4th electron in the out-of-plane direction to stay away from nearby in-plane oxygen electrons. Hence, in such an environment the 4th electron must reside in the out-of-plane e_g orbital.

1.5.2 Hybridization and bonding-antibonding splitting

Let us consider a situation where a Mn e_g level is interacting with an oxygen ligand of the same symmetry, i.e. their wavefunction has spatial overlapping. Just like simple molecular orbital approach to solve the energy levels of a hydrogen molecule, let us take $|\psi\rangle$ as the state vector of an electron in the combined Mn $d_{x^2-y^2}$ and $O_{x^2-y^2}$ system (same treatment is applicable for the case of mixing between Mn $d_{3z^2-r^2}$ and $O_{3z^2-r^2}$). Let $|Mn_{x^2-y^2}\rangle$ and $|O_{x^2-y^2}\rangle$ denote the electron state in the Mn $d_{x^2-y^2}$ and $O_{x^2-y^2}$ levels respectively. If we assume that $|Mn_{x^2-y^2}\rangle$ and $|L_{x^2-y^2}\rangle$ form the adequate basis set, we can expand the ground state $|\psi\rangle$ of the combined system as

$$|\psi\rangle = c_1|Mn_{x^2-y^2}\rangle + c_2|L_{x^2-y^2}\rangle \quad (1.22)$$

Hence, the Schrödinger equation for the molecular state is

$$H(c_1|Mn_{x^2-y^2}\rangle + c_2|L_{x^2-y^2}\rangle) = E_{x^2-y^2}(c_1|Mn_{x^2-y^2}\rangle + c_2|L_{x^2-y^2}\rangle) \quad (1.23)$$

To solve this equation, we project it onto the basis states $|Mn_{x^2-y^2}\rangle$ and $|L_{x^2-y^2}\rangle$:

$$c_1 E_{Mn_{x^2-y^2}} + c_2 t_{Mn-L} = c_1 E_{x^2-y^2} \quad (1.24)$$

$$c_1 t_{L-Mn} + c_2 E_{L_{x^2-y^2}} = c_2 E_{x^2-y^2} \quad (1.25)$$

where $E_{Mn_{x^2-y^2}} = \langle Mn_{x^2-y^2} | H | Mn_{x^2-y^2} \rangle$, $E_{L_{x^2-y^2}} = \langle L_{x^2-y^2} | H | L_{x^2-y^2} \rangle$, $t_{Mn-L} = \langle Mn_{x^2-y^2} | H | L_{x^2-y^2} \rangle$ and $t_{L-Mn} = \langle L_{x^2-y^2} | H | Mn_{x^2-y^2} \rangle$. Let us assume that the hopping integral, $t_{x^2-y^2} = t_{Mn-L} = t_{L-Mn}$. Then the solution is

$$E_{x^2-y^2} = \frac{1}{2} \left[(E_{Mn_{x^2-y^2}} + E_{L_{x^2-y^2}}) \pm \sqrt{(E_{Mn_{x^2-y^2}} - E_{L_{x^2-y^2}})^2 + 4t_{x^2-y^2}^2} \right] \quad (1.26)$$

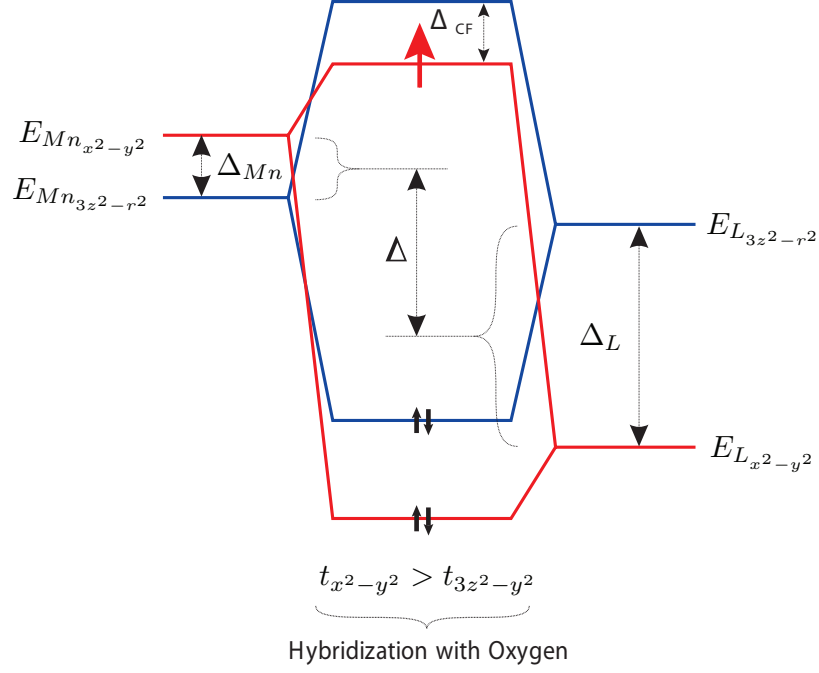


Figure 1.10: Schematic presentation of hybridization between Mn impurity e_g levels split by local reduction of symmetry with the oxygen environment set by the RuO matrix.

Defining $E_{Mn_{x^2-y^2}} - E_{L_{x^2-y^2}} = \Delta$, up to first order:

$$E_{x^2-y^2} = \frac{E_{Mn_{x^2-y^2}} + E_{L_{x^2-y^2}}}{2} \pm \frac{t_{x^2-y^2}^2}{\Delta_{x^2-y^2}} \quad (1.27)$$

Hence the magnitude of the bonding-antibonding splitting depends on two parameters: $t_{x^2-y^2}$ and $\Delta_{x^2-y^2}$. The arguments presented above apply to the Mn $d_{3z^2-r^2}$ level hybridizing with oxygen ligand with $3z^2 - r^2$ symmetry and we get the same expression as Eqn. 1.27 for $E_{3z^2-r^2}$. The role of these parameters are discussed in detail in Chapter 2.

Now, after hybridization, the energy difference between the $x^2 - y^2$ and $3z^2 - r^2$ antibonding states (mainly of Mn $3d$ character) is:

$$\begin{aligned} \Delta_{CF} &= \frac{1}{2}(\Delta_L - \Delta_{Mn}) \\ &+ \frac{1}{4}(\sqrt{16t_{3z^2-r^2}^2 + (-2\Delta + \Delta_L + \Delta_{Mn})^2} \\ &- \sqrt{16t_{x^2-y^2}^2 + (2\Delta + \Delta_L + \Delta_{Mn})^2}) \end{aligned} \quad (1.28)$$

where Δ , Δ_{CF} , Δ_L and Δ_{Mn} are defined in Fig. 1.10. Δ_{CF} can take both positive or negative values depending on relative magnitude of Δ and Δ_L (Δ_{Mn} is typically small for

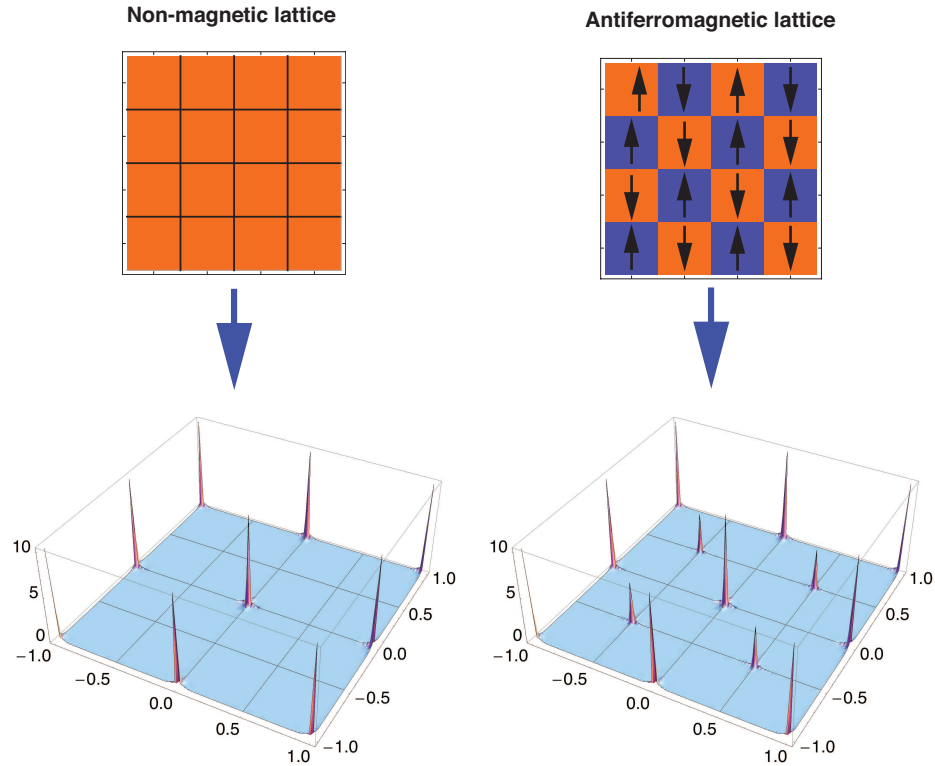


Figure 1.11: (Left top, bottom) Non-magnetic square lattice and the corresponding reciprocal space map showing the structural Bragg peaks. (Right top, bottom) Antiferromagnetic lattice and the corresponding reciprocal space map showing magnetic diffraction peaks together with the structural ones.

these materials). This can lead to reversal of orbital hierarchy which is also discussed in Chapter 2.

1.5.3 Probing the magnetism of a dilute lattice liquid

RSXS is a combination of X-ray diffraction and X-ray absorption spectroscopy. Conventional X-ray Diffraction (XRD) technique is enormously successful in revealing structural information for all kinds of systems, ranging from physics to biology. However, XRD is based on Thomson scattering where the scattering amplitude is proportional to the total charge density of the lattice sites [26]. In case of a square lattice spanned by Ru atoms, there are 44 electrons at each site. If one electron at each site participates in forming a magnetic/charge/orbital superlattice, conventional XRD will not be able to detect these very weak magnetic orderings since the corresponding diffraction peaks will be buried under the hugely intense structural ordering peaks. However, as shown in Sec 1.2, close to the absorption edge, these weak ordering signals get enhanced and it becomes possible to explore the weaker spin/charge/orbital orderings. This idea is schematically presented in

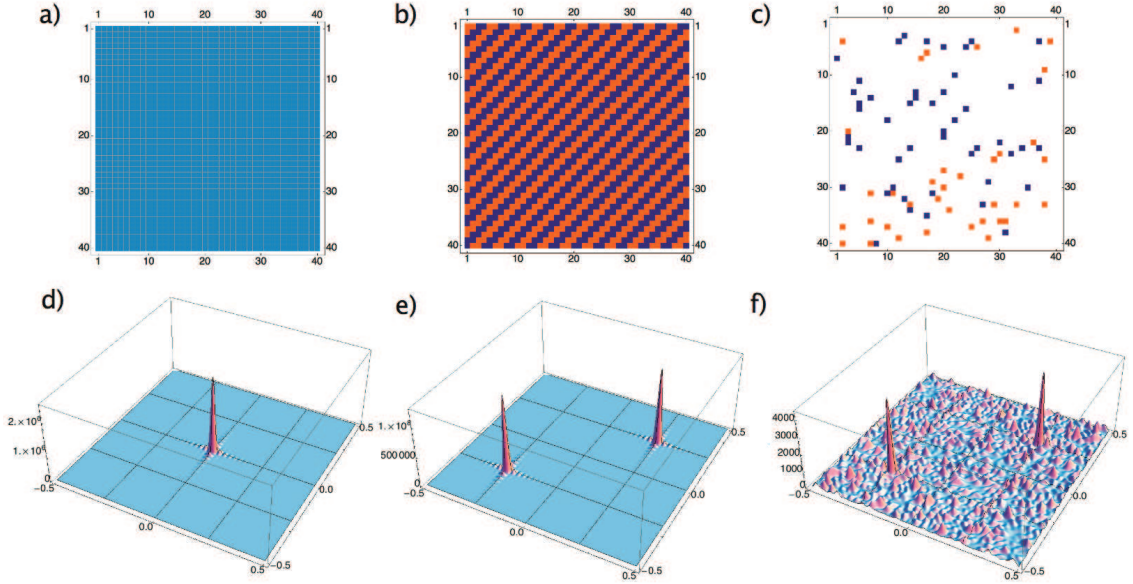


Figure 1.12: (a,d) Non-magnetic square lattice and the corresponding reciprocal space map showing the structural Bragg peaks. (b,e) 100% Mn doped square lattice having an up-up-down-down zig-zag spin order and the corresponding reciprocal lattice map showing only the magnetic diffraction peaks. (c,f) Randomly selected 5% lattice points from (b) and the corresponding diffraction spots resulting from the scattered intensities only from these sites.

Fig. 1.11 where top left presents a nonmagnetic square lattice and the reciprocal space map (that can be obtained by XRD) is shown in the left bottom corner. This can be regarded as a antiferromagnetic lattice above the Néel temperature. Fig. 1.11, top right shows the lattice below the Néel temperature, with a simple antiferromagnetic spin order. Its reciprocal space map (bottom right) shows the appearance of structurally forbidden magnetic peaks as $\mathbf{Q}=(\pm\frac{1}{2}, \pm\frac{1}{2}, 0)$ positions.

Apart from the resonant enhancement of the scattering amplitude, there is another unique feature of RSXS compared to XRD, which is element sensitivity. For instance, in case of $\text{Sr}_3(\text{Mn}_x\text{Ru}_{1-x})_2\text{O}_7$, by tuning the energy of the incoming light to that of the Mn L-edge absorption energy, one can get resonance enhanced signals only from the Mn sites. Now, the dilute Mn atoms are randomly distributed in the system, and therefore, even if there is some kind of order in the host Ru-O system that is participated by the Mn impurities, are we supposed to get any ordering signal at the Mn edge? Fig. 1.12 attempts to answer this question for a simpler situation where Mn spins are 100% correlated. Fig. 1.12 (a) shows a nonmagnetic square lattice (just like Fig. 1.11, top left, only a bigger lattice) and (d) shows the corresponding reciprocal space map presenting only the (0,0,0) peaks (smaller field of view than Fig. 1.11). (b) shows the case of a 100% Mn doped system (like $\text{Sr}_3\text{Mn}_2\text{O}_7$)

where all the Mn atoms are participating in an up-up-down-down zig-zag antiferromagnetic pattern (discussed in detail in Chapter 3). (e) shows the corresponding reciprocal space map revealing a $(\frac{1}{4}, \frac{1}{4}, 0)$ and $(-\frac{1}{4}, -\frac{1}{4}, 0)$ magnetic diffraction peak. In Fig. 1.12 (c) 5% sites are selected randomly from (b) with corresponding spins, i.e. the 5% site spins follow the up-up-down-down zig-zag spins pattern with 100% correlation. (f) shows the reciprocal space map revealing very weak but clear $(\frac{1}{4}, \frac{1}{4}, 0)$ and $(-\frac{1}{4}, -\frac{1}{4}, 0)$ magnetic peaks. This unintuitive result can be explained in the following manner: while the 5% Mn atoms are randomly distributed, they are still residing in the host square lattice. Hence, if the random impurities can somehow participate in the spin order, they will scatter coherently and should give rise to the corresponding magnetic scattering peaks. This cartoon, of course, do not explain many features of the experimental data observed in the real system, for example, broadening of the scattering peaks that indicate domain formation. Also, simulations in Fig. 1.12 assumes 100% spin correlation between the Mn impurities. In case of domain formation in the system, the spin correlation between Mn atoms will be much less than 100%, and in that case should one be able to observe the magnetic peak at the Mn edge? Also, what mechanism allows spins correlation between the dilute Mn atoms in the first place? More importantly, what is the relation between the magnetic order and the metal-insulator transition in this compound seen in Ref. [22]? All these important questions have been addressed in Chapter 3.

1.5.4 Polar surfaces

H. Hwang's group in 2004 has revolutionized the field of designer materials by showing that combining two simple insulators, LaAlO_3 and SrTiO_3 it is possible to produce an interface that is metallic [47]. This has led to a series of discoveries where the essential idea is to combine two or more materials with very simple properties to produce an interfacial region with completely new properties. In case of the original discovery, metallic interface between insulators, it has been showed that the interface is a border between stacks of charge neutral atomic layers in SrTiO_3 and alternately charges atomic layers of LaAlO_3 (see Fig. 1.13). At this point, it is crucial to realize that the electrostatic potential produced by the LaAlO_3 alternating charges stacks diverges with the material thickness. However, nature plays a neat trick to avoid this energetically unfavorable situation by a charge reconstruction starting right at the interface. Of course, such a polar discontinuity has been discussed in semiconductor heterointerfaces for a long time [48] and what is new is the concept of charge redistribution or reconstruction. Unlike the semiconductors, a transition metal ion network can acquire mixed valence and this can balance the charge discontinuity at the interface, explained by the following simplified model. In the LaAlO_3 and SrTiO_3 interface, (Fig. 1.13, panel c), a fraction of the Ti atoms tend to be of 3+ valence instead of its normal valence of 4+. This is possible by bringing extra electrons from the adjacent LaO layer. This would bring the electric field and potential back to zero at the upper surface. Similarly, divergence for the $\text{AlO}_2/\text{SrO}/\text{TiO}_2$ interface can be avoided by removing half an electron from the SrO plane in the form of oxygen vacancies (Fig. 1.13, panel d).

Polar discontinuities can occur at the surface of layered systems with polar planes. This can easily be visualized in the case of $\text{YBCO}_{6,0}$, in which the alternation of $\text{Cu}_{\text{Chain}}^{1+}$,

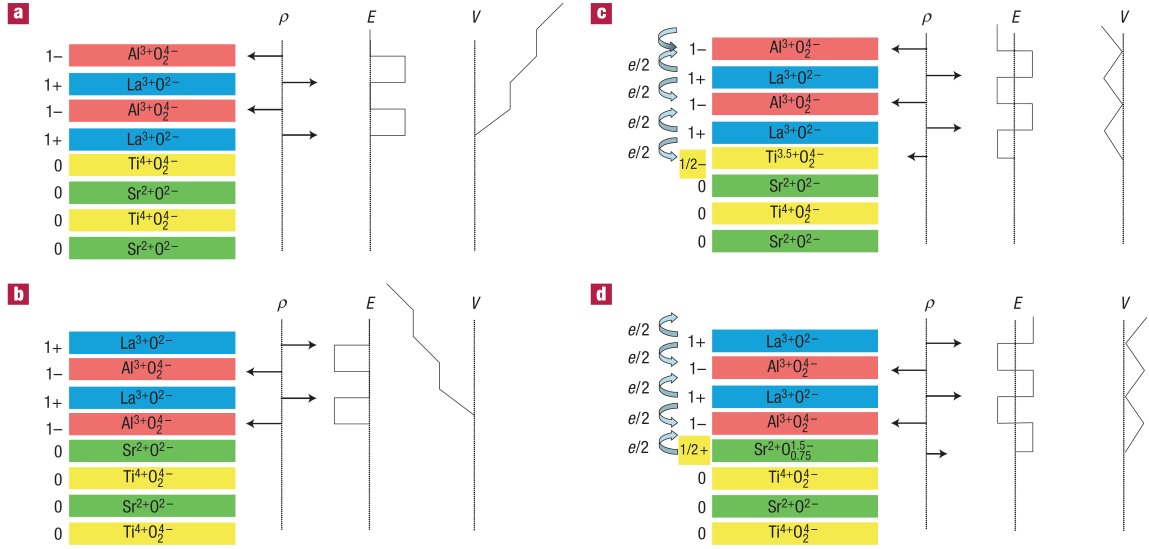


Figure 1.13: Examples of oxide interfaces with polar catastrophe inducing charge reconstruction. Top and bottom panels showing LaO/TiO and AlO/SrO interfaces together with charge density, electric field and potential as a function of layer thickness. Left and right shows the interfaces before and after the charge reconstruction respectively. Taken from [4].

$(\text{Ba}^{2+}\text{O}^{2-})^{0+}$, $(\text{Cu}^{2+}\text{O}^{4-} / \text{Y}^{3+} / \text{Cu}^{2+}\text{O}^{4-})^{1-}$, etc., corresponds to the prototypical case of a $|1 + |1 - |1 + |1 - | \dots$ polar catastrophe [4]. YBCO is complicated by the presence of CuO-chain layers and the lack of a neutral [001] cleavage plane. More specifically, YBCO cleaves between the CuO chain layer and the BaO layer, leaving on the cleaved surface a distribution of CuO and BaO terminations. The surface of cleaved oxygen-ordered YBCO_{6.5} (with alternating oxygen full and empty chains) is shown in Fig. 5.1 (panel a) emphasizing the BaO and CuO chain terminations of the cleaved surface. Surface polarity drives the removal of $\sim 1/2$ electron (hole) from the topmost CuO₂ bilayer (CuO chain layer) for the BaO (CuO chain) termination. This electronic reconstruction leads to ‘overdoped-like’ CuO₂-plane bonding (B) and antibonding (AB) FSS, almost irrespective of the nominal bulk doping. Since ARPES is a surface sensitive technique, ARPES measurements on YBCO always measures a very overdoped Fermi surface, irrespective of the doping level of the bulk. This problem has been solved in Chapter 5 with the help of a novel technique that can continuously tune the surface doping level of YBCO *in situ*.

1.6 Scope

In this thesis spectroscopic data obtained on a number of correlated oxide systems are presented together with models based on cluster multiplet and density functional calculations. The common feature of most of the systems investigated is that the electronic and magnetic

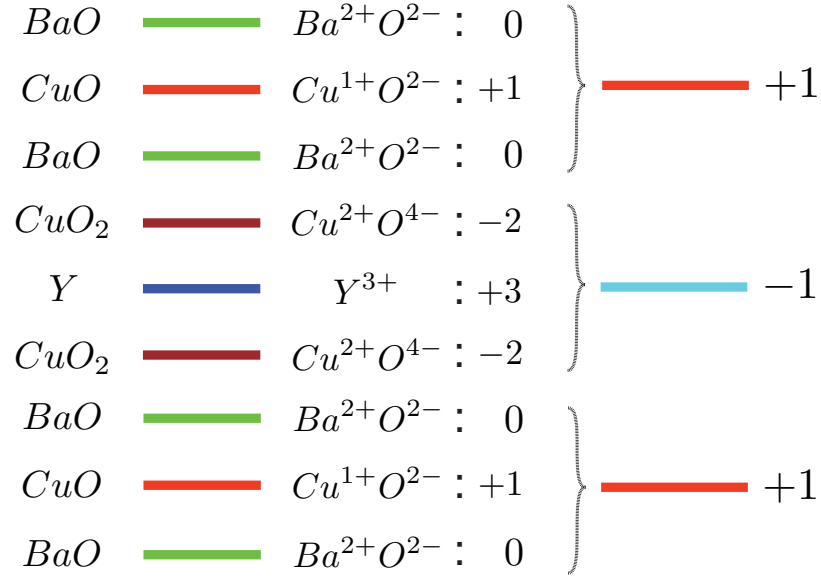


Figure 1.14: Schematic presentation of net ionic charges of YBCO layers that can lead to polar catastrophe. This unfavorable situation can be resolved by simply removing $+1/2$ electronic charge from the topmost layer ($-1/2$ for the $|1-|1+|1-|1+|\dots$ series of the BaO termination).

properties are controlled by impurities in the bulk and on the surface of the materials.

Chapters 2 and 3 present investigation on lightly Mn doped $Sr_3Ru_2O_7$. Our goal is to understand the electronic structure of the material both at room and low temperature and ultimately to understand the mechanism behind the low temperature metal-insulator transition in this compound.

In chapter 2 we zoom into the local electronic structure of the impurity themselves. Here the impurities have localized $3d$ valence shell (Mn) that find themselves in a more delocalized highly covalent $4d$ (Ru) environment and the motivation is to directly probe how this interaction affects the impurities. We start by investigating the valence of the Mn impurities with the help of X-ray Absorption Spectroscopy (XAS) which is the most direct and reliable experimental technique to check valence of an element. X-ray linear dichroism has been used to investigate population and symmetry of the highest occupied valence orbital. With the help of density functional theory and cluster multiplet calculations, we developed a model to describe the hierarchy of the crystal field levels of the Mn impurities.

Chapter 3 focuses on the long range magnetic properties of the Mn doped $Sr_3Ru_2O_7$ with Resonant Soft X-ray Scattering (RSXS) on the Mn and Ru L-edges. We found and analyzed the $(\frac{1}{4}, \frac{1}{4}, 0)$ forbidden diffraction peak and connected it to an antiferromagnetic instability in the parent compound. Doping dependent scattering studies revealed the magnetic structure of the low temperature insulating phase and ultimately the mechanism behind the metal-insulator transition itself.

In chapter 4 we investigate the metal insulator transition in $\text{Ca}_3\text{Ru}_2\text{O}_7$ by Angle Resolved Photoemission Spectroscopy (ARPES). Structurally, $\text{Ca}_3\text{Ru}_2\text{O}_7$ is similar to $\text{Sr}_3\text{Ru}_2\text{O}_7$, with Sr is replaced by Ca that introduces rotation and tilting of the metal-oxide octahedrons. However, this brings in profound changes in the electronic and magnetic properties. While $\text{Sr}_3\text{Ru}_2\text{O}_7$ is metallic paramagnet, $\text{Ca}_3\text{Ru}_2\text{O}_7$ goes through a Néel and structural phase transition at 56K and 48K respectively. ARPES measurements revealed a momentum dependent gap opening up below 48K pointing towards an electronic instability.

Chapter 5 presents our ARPES studies on high temperature superconductor YBCO. ARPES studies on YBCO has always been plagued by the fact that the measured Fermi surface appeared to be that of an overly overdoped system, regardless of the doping level of the bulk material. Here we pointed out that one has to take care of the fact that YBCO is a layered material where each layer can be described as a polar surface. By evaporating potassium impurities on these polar surfaces, we managed to continuously tune the doping level of the material surface and finally measured the Fermi surface of the underdoped YBCO for the first time. The technique promises the ability to continuously tune the doping level of other hole doped high- T_c superconductor from overdoped to all the way to a Mott insulating state that may even let one go to the electron doped regime.

In chapter 6 we discuss the unresolved problem of the connection between the pseudogap and the superconducting gap of a high-temperature superconductor. We sifted through the enormous collection of data on copper oxide based high- T_c superconductors and demonstrated that there are two coexisting energy scales in these compounds exhibited by the pseudogap and the superconducting gap. It has been pointed out that most of the existing experimental techniques can probe only one type of gap: either the superconducting gap or the pseudogap. We suggested that the pseudogap state is a precursor and necessary condition for the superconducting state.

Bibliography

- [1] M. Imada, A. Fujimori, and Y. Tokura, Rev. Mod. Phys. **70**, 1039 (1998).
- [2] P.W. Anderson, Science, **177**, 393 (1972).
- [3] M.A. Hossain *et al.*, Phys. Rev. Lett. **101**, 016404 (2008).
- [4] N. Nakagawa, H. Hwang and D.A. Muller, Nature Materials **5**, 204 (2006).
- [5] M.A. Hossain *et al.*, Nature Physics **4**, 527 (2008).
- [6] P. Blaha *et al.*, An Augmented Plan Wave and Local Orbitals Program for Calculating Crystal Properties, edited by K. Schwarz (Technical University of Wien, Vienna, 2001).
- [7] M.W. Haverkort, cond-mat/0505214 v1 (2005).
- [8] Y. Yoshida *et al.*, Phys. Rev. B **72**, 054412 (2005).
- [9] R. D. Shannon, Acta Cryst. **A32**, 751(1976).
- [10] H. Shaked, J.D. Jorgensen, O. Chmaissem, S. Ikeda and Y. Maeno, J. Solid State Chem. **154**, 361 (2000).
- [11] J. F. Mitchell *et al.*, J. Solid State Chem. **141**, 599 (1998).
- [12] P. B. Allen *et al.*, Phys. Rev. B **53**, 4393 (1996).
- [13] L. Klein *et al.*, J. Phys. Condens. Matter **8**, 10 111 (1996).
- [14] Y. Maeno *et al.*, Nature (London) **372** (1994) 532.
- [15] A.P. Mackenzie and Y. Maeno, Rev. Mod. Phys. **75**, 657 (2003).
- [16] K. Ishida *et al.*, Nature (London) **396**, 658 (1998).
- [17] G. Cao, S. McCall, M. Shepard, J. E. Crow and R. P. Guertin, Phys. Rev. B **56**, 321 (1997).
- [18] S. Nakatsuji, S. I. Ikeda, and Y. Maeno, J. Phys. Soc. Jpn. **66**, 1868 (1997).
- [19] S. A. Grigera *et al.*, Science **294**, 329 (2001).
- [20] R. A. Borzi *et al.*, Science **315**, 214 (2007).
- [21] Y. Yoshida *et al.*, Phys. Rev. B **69**, 220411(R) (2004).

-
- [22] R. Mathieu *et al.*, Phys. Rev. B **72**, 092404 (2005).
- [23] M. Platé *et al.*, Phys. Rev. Lett. **95**, 077001 (2005).
- [24] N.E. Hussey *et al.*, Nature **425**, 814 (2003).
- [25] N. Doiron-Leyraud *et al.*, Nature **447**, 565 (2007).
- [26] J. Als-Nielsen, D. McMorrow, Elements of Modern X-ray Physics, John Wiley (2001).
- [27] J. Stöhr and H.C. Siegmann, Magnetism, Springer (2006).
- [28] J. Stöhr, NEXAFS Spectroscopy, Springer (1992).
- [29] C.T. Chen *et al.*, Phys. Rev. Lett. **68**, 2543 (1992).
- [30] A. Tanaka and T. Jo, J. Phys. Soc. Jpn. **63**, 2788 (1994).
- [31] S. Nakatsuji *et al.*, Phys. Rev. Lett. **84**, 2666 (2000).
- [32] A. Damascelli *et al.*, Phys. Rev. Lett. **85**, 5194 (2000).
- [33] I.I. Mazin and D.J. Singh, Phys. Rev. Lett. **82**, 4324 (1999).
- [34] M.W. Haverkort *et al.* arXiv:0805.4341v1 (2008).
- [35] R.G. Newton, Am. J. Phys. **44**, 639 (1976).
- [36] R. S. Perry, Y. Maeno, cond-mat/0403572.
- [37] Kostic *et al.*, Phys. Rev. Lett. **81**, 2498 (1998).
- [38] F. de Groot and A. Kotani, Core Level Spectroscopy of Solids, CRC Press (2008).
- [39] S. Hüfner, Photoelectron Spectroscopy, Springer (2003).
- [40] A. Damascelli, Z. Hussain and Z.-X. Shen, Rev. Mod. Phys. **75**, 473 (2003).
- [41] J.C. Campuzano, Angle resolved photoemission in the high temperature superconductors in *Strong interactions in low dimensions*, D. Baeriswyl and L. Degiorgi ed., Springer (2007).
- [42] A. Damascelli, Physica Scripta **109**, 61 (2004).
- [43] H. Kurata and C. Colliex, Phys. Rev. B **48**, 2102 (1993).
- [44] S. Gasiorowicz, *Quantum Physics*, John Wiley.
- [45] J.P. Hannon, G.T. Trammel, M. Blume and D. Gibbs, Phys. Rev. Lett. **61**, 1245 (1988).
- [46] J.P. Hill and D.F. McMorrow, Acta Cryst., **A52**, 236 (1996).
- [47] A. Ohtomo and H. Y. Hwang, Nature **427**, 423 (2004).
- [48] G.A. Baraff, J.A. Appelbaum, D.R. Hamann, Phys. Rev. Lett. **38**, 237 (1977).

Chapter 2

Crystal-field level inversion in lightly Mn-doped $\text{Sr}_3\text{Ru}_2\text{O}_7$

$\text{Sr}_3(\text{Ru}_{1-x}\text{Mn}_x)_2\text{O}_7$, in which $4d$ -Ru is substituted by the more localized $3d$ -Mn, is studied by x-ray dichroism and spin-resolved density functional theory. We find that Mn impurities do not exhibit the same $4+$ valence of Ru, but act as $3+$ acceptors; the extra e_g electron occupies the in-plane $3d_{x^2-y^2}$ orbital instead of the expected out-of-plane $3d_{3z^2-r^2}$. We propose that the $3d-4d$ interplay, via the ligand oxygen orbitals, is responsible for this crystal-field level inversion and the material's transition to an antiferromagnetic, possibly orbitally-ordered, low-temperature state. ¹

¹A version of this chapter has been published. Hossain, M.A., Hu, Z., Haverkort, M.W., Burnus, T., Chang, C.F., Klein, S., Denlinger, J.D., Lin, H.-J., Chen, C.T., Mathieu, R., Kaneko, Y., Tokura, Y., Satow, S., Yoshida, Y., Takagi, H., Tanaka, A., Elmov, I.S., Sawatzky, G.A., Tjeng, L.H., and Damascelli A. (2008) Crystal-field level inversion in lightly Mn-doped $\text{Sr}_3\text{Ru}_2\text{O}_7$. *Physical Review Letters*. **101**: 016404.

Ruthenium oxides are a particularly interesting class of materials exhibiting Fermi liquid properties, unconventional superconductivity, ferromagnetism and metamagnetism, antiferromagnetic insulating behavior, and orbital ordering. The richness of this physics is a testament of the intimate interplay between charge, spin, orbital, and lattice degrees of freedom, despite the fact that $4d$ transition metals (TM) are not considered to induce strong electronic correlations. The radial extent of the $4d$ wave functions is significantly larger than for TM- $3d$ and even O- $2p$ orbitals. This leads to, on the one end, weaker correlation effects than in $3d$ TM-oxides; on the other hand, to an interesting competition between local and itinerant physics. Doping a TM $4d$ -O $2p$ host with dilute $3d$ TM impurities might thus be extremely effective in tuning valence, spin, and, orbital characteristics and, in turn, the macroscopic physical properties. We will explore these ideas in the hotly debated $\text{Sr}_3(\text{Ru}_{1-x}\text{Mn}_x)_2\text{O}_7$ family: metamagnetism and a field tuned quantum phase transition were discovered on the pure compound [1, 2, 3]; with the inclusion of a few percent of Mn, a metal-insulator transition was observed in transport experiments and the emergence of a Mott-like antiferromagnetic state was proposed [4].

To address the nature of the metal-insulator phase transition in $\text{Sr}_3(\text{Ru}_{1-x}\text{Mn}_x)_2\text{O}_7$ and the role of Mn impurities, we used x-ray absorption spectroscopy (XAS). This is an element and site-specific probe that provides information on the electronic structure of impurities and host atoms separately, as well as on the emergence of magnetic correlations. By performing polarization-dependent XAS experiments, one can study linear dichroism (LD) and magnetic circular dichroism (MCD). While MCD in an externally applied magnetic field is sensitive to the expectation value of the local magnetic moment $\langle \mathbf{M} \rangle$ and is thus a probe of ferromagnetism, LD is proportional to $\langle \mathbf{M}^2 \rangle$ and in turn the nearest-neighbor spin-spin correlation function, thus providing unique information on orbital population [5, 6] as well as antiferromagnetic order [7, 8]. We performed temperature-dependent MCD experiments in a 0.5 Tesla field on Mn-doped $\text{Sr}_3\text{Ru}_2\text{O}_7$ for Mn concentration as high as 20%, without detecting any signal above the 2% noise level, which excludes ferromagnetism down to 15K. In this paper, we will thus concentrate on room-temperature XAS-LD experiments.

Single crystals of $\text{Sr}_3(\text{Ru}_{1-x}\text{Mn}_x)_2\text{O}_7$ were grown by the floating zone technique [4]. Total electron-yield XAS measurements were performed at the Dragon beamline at NSRRC in Taiwan and at beamline 8.0.1 at ALS in Berkeley (the energy resolution was 0.3 eV and the degree of linear polarization $\sim 98\%$). All sample surfaces were prepared by in-situ cleaving at pressures better than 2×10^{-9} mbar. The XAS data were normalized to the beam intensity I_0 ; the absolute energy calibration (with accuracy ~ 0.02 eV) was obtained from the simultaneous XAS measurement of a MnO single crystal performed in a separate chamber with a small part of the beam [9].

Before discussing the LD results and possible ordering phenomena, we will address the very basic question of what is the valence of Mn in $\text{Sr}_3(\text{Ru}_{1-x}\text{Mn}_x)_2\text{O}_7$. The pure compound is ionic with valence Sr^{2+} , Ru^{4+} , and O^{2-} , which would suggest the substitution of Ru^{4+} with Mn^{4+} upon doping. Interestingly, in the related compounds $\text{SrRu}_{1-x}\text{Cr}_x\text{O}_3$ [10] and $\text{CaRu}_{1-x}\text{Cr}_x\text{O}_3$ [11] one might also expect the naive $\text{Ru}^{4+} \rightarrow \text{Cr}^{4+}$ substitution. However, although the valence was not probed directly, from the anomalous dependence of the unit cell volume on Cr content a substantial $\text{Ru}^{4+} + \text{Cr}^{4+} \rightarrow \text{Ru}^{5+} + \text{Cr}^{3+}$ charge transfer was proposed [10, 11]. Thus, in the present case, the $4+$ valence of Mn should not be taken for

granted but determined experimentally. Room-temperature, isotropic Mn $L_{2,3}$ -edge XAS data from 10% Mn-doped $\text{Sr}_3\text{Ru}_2\text{O}_7$ are presented in Fig. 2.1, together with the results from other Mn-oxide compounds characterized by a well-defined Mn valence, such as MnO (2+), LaMnO_3 (3+), and $\text{Sr}_3\text{Mn}_2\text{O}_7$ (4+) (see Fig. 2.2b for a description of the $L_{2,3}$ -edge XAS process). As shown in Fig. 2.1, the energy position of the $L_{2,3}$ absorption edge is exquisitely sensitive to the valence of an element. The shift of the center of gravity to high energy upon increasing the Mn valence from 2+ to 4+ (i.e., ‘chemical shift’), and the very close match between $\text{Sr}_3(\text{Ru}_{0.9}\text{Mn}_{0.1})_2\text{O}_7$ and LaMnO_3 $L_{2,3}$ -edge energy and lineshape (inset of Fig. 2.2), provide already the first surprise: Mn impurities in $\text{Sr}_3\text{Ru}_2\text{O}_7$ act as Mn^{3+} electron acceptors.

The 3+ valence of Mn has important consequences. While Mn^{4+} has three d electrons in the 1/2-filled t_{2g} shell, Mn^{3+} has an extra e_g electron ($t_{2g}^3 e_g^1$) and is Jahn-Teller active, which adds the orbital dimension to the problem. The key question is whether the e_g electron will occupy the in-plane $d_{x^2-y^2}$ or out-of-plane $d_{3z^2-r^2}$ orbital. Since $\text{Sr}_3\text{Ru}_2\text{O}_7$ is a tetragonally distorted system with RuO_6 octahedra elongated along the c -axis, crystal-field splitting

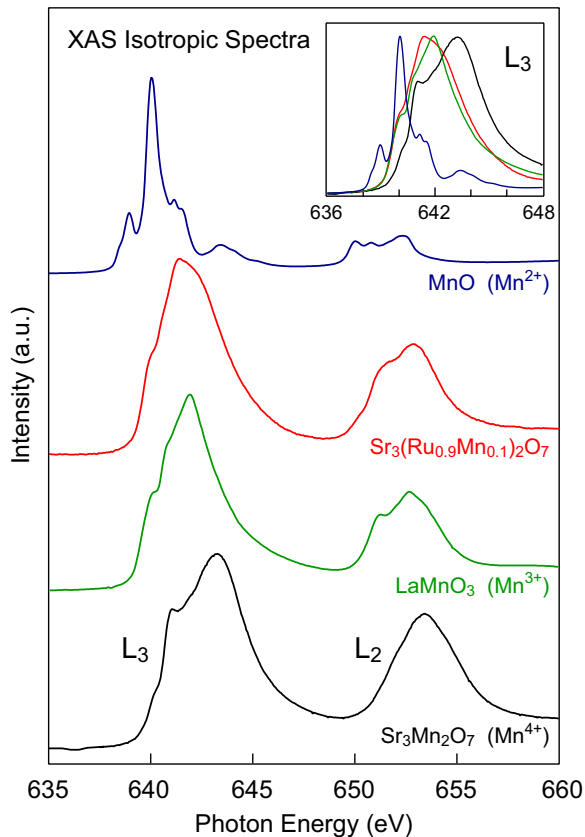


Figure 2.1: Isotropic Mn $L_{2,3}$ -edge XAS data from $\text{Sr}_3(\text{Ru}_{0.9}\text{Mn}_{0.1})_2\text{O}_7$ and stoichiometric Mn-oxides of known valences. Inset: detailed view of the L_3 -edge chemical shift.

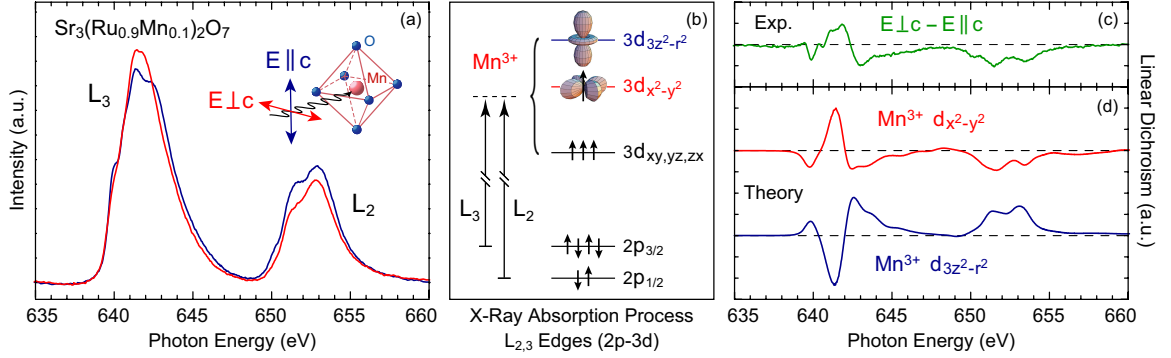


Figure 2.2: (a) Polarization-dependent Mn $L_{2,3}$ -edge XAS spectra from $\text{Sr}_3(\text{Ru}_{0.9}\text{Mn}_{0.1})_2\text{O}_7$ at $T = 295$ K. (b) Scheme of the XAS process: the L_2 (L_3) edge corresponds to the excitation of a Mn $2p_{1/2}$ ($2p_{3/2}$) electron to the Mn $3d$ valence shell. The L_3 - L_2 energy separation is due to the $2p$ core level spin-orbit coupling. (c) Corresponding experimental linear dichroism: $\text{LD} = [I_{\text{XAS}}(\mathbf{E} \perp c) - I_{\text{XAS}}(\mathbf{E} \parallel c)]$. (d) Calculated LD spectra for two possible e_g -orbital occupations ($x \parallel a, y \parallel b, z \parallel c$).

would lead to the occupation of the out-of-plane $d_{3z^2-r^2}$ orbital. This intuitive picture can be directly verified by x-ray LD. Room-temperature, linearly polarized Mn $L_{2,3}$ -edge XAS spectra from 10% Mn-doped $\text{Sr}_3\text{Ru}_2\text{O}_7$ are presented in Fig. 2.2a. The corresponding LD, defined as the difference between XAS spectra acquired with light polarization perpendicular ($\mathbf{E} \perp c$) and parallel ($\mathbf{E} \parallel c$) to the crystal c axis, is shown in Fig. 2.2c. Information about the orbital population of Mn e_g levels can be extracted through the detailed comparison between the measured LD and multiplet cluster calculations for different electronic configurations of the Mn, which are shown in Fig. 2.2d. As we will discuss below, the multiplet calculations are based on parameters from our *ab-initio* density functional theory results (Fig. 2.3 and 2.4), and are thus not an arbitrary fit of the data. The two simulated LD spectra are opposite to each other in terms of sign and reveal the in-plane $d_{x^2-y^2}$ orbital polarization for the Mn^{3+} e_g electrons (Fig. 2.2b), instead of the expected $d_{3z^2-r^2}$. Also, the room-temperature LD spectra are virtually indistinguishable for all of the $\text{Sr}_3(\text{Ru}_{1-x}\text{Mn}_x)_2\text{O}_7$ samples we studied (not shown), indicating that the Mn^{3+} valence and $d_{x^2-y^2}$ orbital polarization persist across the whole 5-20% doping range.

This *inversion* of the conventional *crystal-field orbital hierarchy* at Mn impurities in $\text{Sr}_3(\text{Ru}_{1-x}\text{Mn}_x)_2\text{O}_7$ is a very surprising result. To illustrate this point, we have performed local-density approximation (LDA) band-structure calculations for undoped $\text{Sr}_3\text{Ru}_2\text{O}_7$ (Ru327) and $\text{Sr}_3\text{Mn}_2\text{O}_7$ (Mn327), with the full-potential linearized augmented plane-wave density functional theory code WIEN2K. In both cases we have used structural data for Ru327 [12], since our end goal will be that of studying Ru327 for dilute Ru-Mn substitution. As shown in Fig. 2.3a and b, the basic electronic structures for the two stoichiometric compounds is very similar and is set by the overlap of O- $2p$ and TM- d orbitals. However, the Mn- $3d$ orbitals are more spatially localized than the rather extended Ru- $4d$ orbitals; this leads

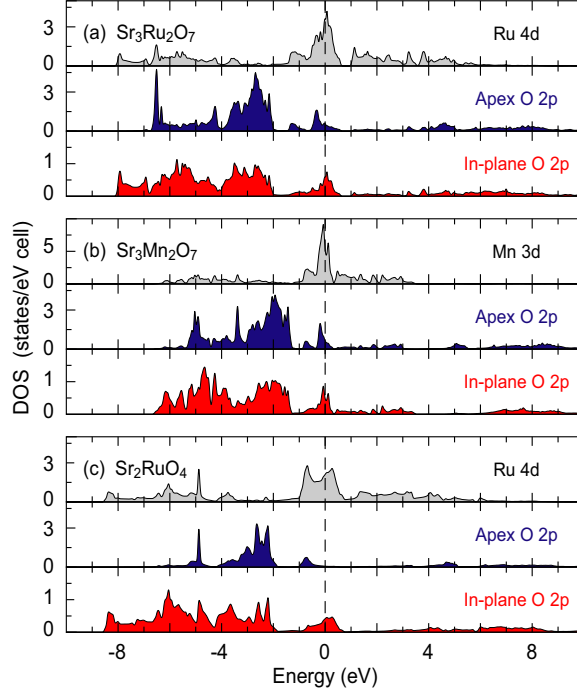


Figure 2.3: Density-of-states (DOS) of stoichiometric (a) $\text{Sr}_3\text{Ru}_2\text{O}_7$ (Ru327), (b) $\text{Sr}_3\text{Mn}_2\text{O}_7$ (Mn327) with the crystal structure of Ru327, and (c) Sr_2RuO_4 (Ru214).

to a reduced bonding-antibonding splitting with the O- $2p$ states and, as clearly evidenced by the in-plane O- $2p$ density-of-states (DOS), to an overall 30% bandwidth reduction in Mn327 as compared to Ru327. As for the states of mainly TM- d character, the t_{2g} band is located within a 1-2 eV range about the chemical potential and is partially occupied (corresponding to a 4+ valence for both Mn and Ru), while the e_g states are higher in energy and completely unoccupied. Most importantly, as summarized in Table 2.1, the first moments of the TM- e_g partial DOS indicate a lower energy for the $d_{3z^2-r^2}$ than $d_{x^2-y^2}$ states in both Ru327 and Mn327, consistent with the standard crystal field description for elongated TM- O_6 octahedra.

To understand the origin of the level inversion observed in $\text{Sr}_3(\text{Ru}_{1-x}\text{Mn}_x)_2\text{O}_7$, we have to further our density functional theory study with the inclusion of dilute Mn impurities. The close similarity of Ru327 and Sr_2RuO_4 (Ru214) electronic structures, with almost identical bandwidths (Fig. 2.3a,c), first moments (Table 2.1), and marginal k_z dispersion (not-shown), suggests that the computationally demanding problem of performing calculations for dilute impurities in bilayer Ru327 can be more efficiently solved in single-layer Ru214 [13] (the main difference between the two is the apical oxygen DOS in Fig. 2.3a,c, which is due to the presence of an additional apical site within the RuO_2 bilayer in Ru327 and is not relevant to the present discussion). We have thus performed spin-polarized calculations (LSDA) for Mn-doped Ru214 with a 3×3 supercell in the ab -plane ($\sim 11\%$ Mn).

As shown by the spin-up e_g Mn DOS in Fig. 2.4a,b, in which Mn- $d_{x^2-y^2}$ is lower in energy than Mn- $d_{3z^2-r^2}$, LSDA calculations do reproduce the crystal-field inversion discovered in $\text{Sr}_3(\text{Ru}_{1-x}\text{Mn}_x)_2\text{O}_7$. This result, which as we have seen is specific to the case in which Mn is introduced as an impurity, originates from the interplay between the spatially confined Mn-3d orbitals and the very extended, yet very anisotropic, Ru4d-O2p electronic backbone of the Ru-O host. Let us illustrate this unusual behavior on the basis of the qualitative hybridization scheme of Fig. 2.4c-f. Before the O/Mn-impurity hybridization is turned on (Fig. 2.4c and f), the Mn e_g orbitals are arranged according to the conventional crystal-field splitting for elongated TM- O_6 octahedra, with a small positive difference $\delta = \epsilon_x - \epsilon_z$ for the on-site energies $\epsilon_{x,z}$ of the Mn $d_{x^2-y^2}$ and $d_{3z^2-r^2}$ orbitals. As the hybridization is turned on, however, a level inversion $\Delta_{CF} > 0$ can be realized if $\tau_z^2/\Delta_z - \tau_x^2/\Delta_x > \delta$, where Δ_x (Δ_z) is the on-site energy difference between Mn $d_{x^2-y^2}$ ($d_{3z^2-r^2}$) and in-plane (apical) oxygen ligand orbitals, and τ_x (τ_z) is the in-plane (out-of-plane) O-ligand/Mn- d hybridization parameter. Since $\tau_x > \tau_z$ for elongated octahedra, the level inversion requires $\Delta_x \gg \Delta_z$, which is indeed realized in Mn-doped Ru214 and Ru327 with a few eV difference between Δ_x and Δ_z . Note, however, that although the LSDA calculations of Fig. 2.4a,b do capture the orbital hierarchy revealed by XAS-LD experiments, the location of the Mn $d_{x^2-y^2}$ orbitals right above the chemical potential would still lead to a Mn⁴⁺ valence. This can be understood as a consequence of the self-interaction that in LDA reduces the ionization energy of localized states more than that of extended states, making it easier for Mn impurities embedded in the Ru-O host to achieve a higher oxidation state. To some extent the LDA+U scheme takes care of the self-interaction problem and Mn³⁺ is obtained in calculations with $U_{Mn} > 4$ eV [14].

The findings of our density functional theory study provide an ab-initio foundation for the ligand field calculations of the Mn multiplet electronic structure and LD spectra presented in Fig. 2.2d. These were performed with the program XTLS8.3 [15] and the parameters $U_{dd}=4.5$, $U_{dp}=6.0$, $\Delta=0.5$, $\delta = \epsilon_x - \epsilon_z = 0.2$, $\tau_{x(z)} = \sqrt{3}pd\sigma_{x(z)}$, all expressed in eV, where: U_{dd} and U_{dp} are the Mn $d-d$ and Mn $d-2p$ average Coulomb repulsion; Δ is the multiplet average energy difference between the Mn d^4 and the Mn $d^5\bar{L}$ configuration; $pd\sigma_z = -1.2$ eV is the out-of plane O-ligand/Mn- d hopping-integral, which has been taken

Orbital	Ru327	Mn327	Ru214
Symmetry	(eV)	(eV)	(eV)
TM $_{x^2-y^2}$	3.23	1.94	3.20
TM $_{3z^2-r^2}$	2.93	1.82	2.93
MO $_{3z^2-r^2}$	-6.00	-4.20	-5.73
MO $_{x^2-y^2}$	-6.95	-4.94	-7.38

Table 2.1: DOS first moments ($\int \omega \text{DOS}(\omega) d\omega$) calculated for oxygen molecular orbitals (MO) and transition metal (TM) e_g orbitals with $x^2 - y^2$ and $3z^2 - r^2$ symmetry, for stoichiometric Ru327, Mn327 (in the Ru327 structure), and Ru214. Negative (positive) values identified occupied (unoccupied) states.

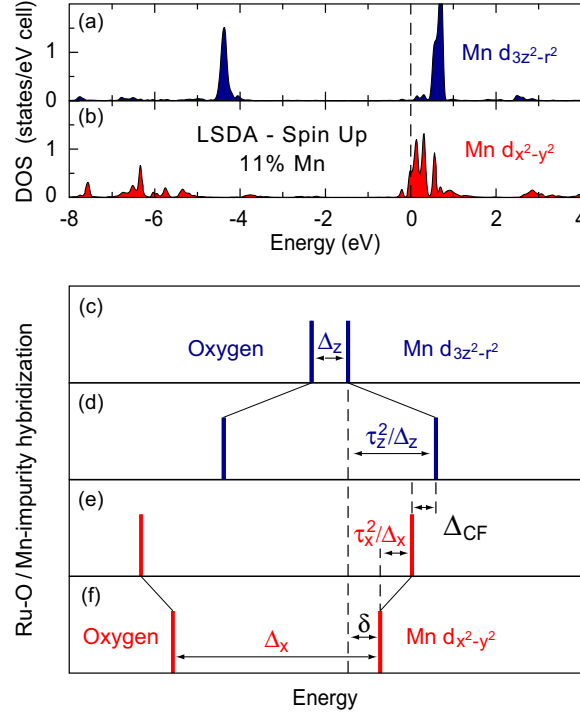


Figure 2.4: (a,b) Spin-up density-of-states (DOS) from LSDA calculations for out-of-plane $d_{3z^2-r^2}$ and in-plane $d_{x^2-y^2}$ Mn e_g orbitals in 11% Mn-doped Ru oxides. (c-f) Ru-O/Mn-impurity hybridization leading to the Mn orbital hierarchy inversion: (c,f) energy of out-of-plane and in-plane Mn-impurity and O orbitals in the $\text{Sr}_3\text{Ru}_2\text{O}_7$ host material before the Mn-O hybridization is turned on; (d,e) once the O/Mn-impurity hybridization is considered, the Mn e_g -orbital hierarchy is inverted ($\Delta_{CF} > 0$) if $\tau_z^2/\Delta_z - \tau_x^2/\Delta_x > \delta$.

to be 80% of the in-plane $pd\sigma_x = -1.5$ eV. Finally, the $d_{3z^2-r^2}$ LD spectrum in Fig. 2.2d was calculated with degenerate ligand orbitals, in which case $d_{3z^2-r^2}$ is occupied. The $d_{x^2-y^2}$ LD spectrum is instead obtained with $\Delta_x - \Delta_z = 4.7$ eV, and the close agreement with the experimental LD spectrum (Fig. 2.2c,d) provides a direct confirmation of our analysis.

We have shown that, at the microscopic level, the remarkable sensitivity of $\text{Sr}_3\text{Ru}_2\text{O}_7$ to light Mn doping stems from the interplay of the localized Mn $3d$ impurity with extended Ru $4d$ -O $2p$ orbitals. Clearly, one should include in the calculations also detailed information on the local structure around the Mn impurities: a contraction along the c axis and elongation along a and b axes have been seen by x-ray diffraction across the metal-insulator transition [4], which might imply a compression of the MnO_6 octahedra. Our study indicates that, although such compression would be consistent with - and further enhance - the observed crystal-field level inversion, the driving mechanism for this phenomenon is purely of electronic origin. More generally, the substitution of $3d$ -TM impurities in $4d$ and even $5d$ TM-oxides might provide a novel, powerful approach to the tailoring of the physical

properties of complex electronic oxides.

This work is supported by the Sloan Foundation (AD), ALS Doctoral Fellowship (MAH) and CRC (AD, GAS) Programs, NSERC, CFI, CIFAR, and BCSI. ALS is supported by the U.S. DOE under Contract No. DE-AC02-05CH11231, and the research in Köln by the Deutsche Forschungsgemeinschaft (DFG) through SFB 608.

Bibliography

- [1] R.S. Perry *et al.*, Phys. Rev. Lett. **86**, 2661 (2001).
- [2] S.A. Grigera *et al.*, Science **294**, 329 (2001).
- [3] R.S. Perry *et al.*, Phys. Rev. Lett. **92**, 166602 (2004).
- [4] R. Mathieu *et al.*, Phys. Rev. B **72**, 092404 (2005).
- [5] C.T. Chen *et al.*, Phys. Rev. Lett. **68**, 2543 (1992).
- [6] D.J. Huang *et al.*, Phys. Rev. Lett. **92**, 087202 (2004).
- [7] P. Kuiper *et al.*, Phys. Rev. Lett. **70**, 1549 (1993).
- [8] D. Alders *et al.*, Phys. Rev. B **57**, 11623 (1998).
- [9] H. Kurata and C. Colliex, Phys. Rev. B **48**, 2102 (1993).
- [10] A.J. Williams *et al.*, Phys. Rev. B **73**, 104409 (2006).
- [11] V. Durairaj *et al.*, Phys. Rev. B **73**, 214414 (2006).
- [12] H. Shaked *et al.*, J. Sol. State Chem. **154**, 361(2000).
- [13] O. Chmaissem *et al.*, Phys. Rev. B **57**, 5067 (1998).
- [14] I.S. Elfimov, M.W. Haverkort, *et al.*, unpublished (2007).
- [15] A. Tanaka and T. Jo, J. Phys. Soc. Jpn. **63**, 2788 (1994).

Chapter 3

Magnetic superstructure and M-I transition in Mn-substituted $\text{Sr}_3\text{Ru}_2\text{O}_7$

We present a temperature-dependent resonant elastic soft x-ray scattering (REXS) study of the metal-insulator transition in $\text{Sr}_3(\text{Ru}_{1-x}\text{Mn}_x)_2\text{O}_7$, performed at both Ru and Mn L -edges. Resonant magnetic superstructure reflections, which indicate an incipient instability of the parent compound, are detected below the transition. Based on modelling of the REXS intensity from randomly distributed Mn impurities, we establish the inhomogeneous nature of the metal-insulator transition, with an effective percolation threshold corresponding to an anomalously low $x \lesssim 0.05$ Mn substitution. ¹

¹A version of this chapter will be submitted for publication. Hossain, M.A., Bohnenbuck, B., Chuang, Y.-D., Cruz Gonzalez, A.G., Wu, H.-H., Zegkinoglu, I., Haverkort, M.W., Geck, J., Hawthorn, D.G., Hu, Z., Schüßler-Langeheine, C., Mathieu, R., Tokura, Y., Satow, S., Takagi, H., Yoshida, Y., Denlinger, J.D., Elfimov, I.S., Hussain, Z., Keimer, B., Sawatzky, G.A., and Damascelli, A. (2009) Magnetic Superstructure and Metal-Insulator Transition in Mn-Substituted $\text{Sr}_3\text{Ru}_2\text{O}_7$.

Electronic and lattice instabilities in strongly correlated electron systems give rise to many fascinating phenomena, such as for example various types of spin, charge, and orbital ordering. This is a common feature of many of the $3d$ transition-metal oxides, with the best-known examples including the stripe instability in the cuprate superconductors and the magnetic phase separation in manganites. Competing instabilities and ordering phenomena can also be found in the somewhat less correlated $4d$ transition-metal oxides, with the ruthenates being one of the most prominent families. $\text{Sr}_3\text{Ru}_2\text{O}_7$, which is the subject of this study, is known as a metal on the verge of ferromagnetism [1] due to the presence of strong ferromagnetic fluctuations. More recently, magnetic field tuned quantum criticality [2] and electronic nematic fluid behavior [3] have been proposed for this compound and associated with a metamagnetic transition. However, the deeper connection between these effects is still highly debated and its description will depend on a fuller understanding of the incipient instabilities in $\text{Sr}_3\text{Ru}_2\text{O}_7$.

Magnetic impurities such as Mn have been introduced in $\text{Sr}_3\text{Ru}_2\text{O}_7$ in an attempt to stabilize the magnetic order in the system [4]. It has been shown that due to the interplay between localized Mn $3d$ and delocalized Ru $4d$ -O $2p$ valence states, Mn impurities display an unusual crystal field level inversion already at room temperature [5]. Upon lowering the temperature, a metal-insulator phase transition has been observed for 5% Mn substitution at $T_c \simeq 50$ K, and at progressively higher T_c upon increasing the Mn concentration [4]. In this Letter, we investigate the nature of the low-temperature insulating phase of $\text{Sr}_3(\text{Ru}_{1-x}\text{Mn}_x)_2\text{O}_7$ and the role of Mn impurities using resonant elastic soft x-ray scattering (REXS). For the first time we have been able to measure the diffraction signal from randomly-distributed dilute impurities; we will show that Mn substitution not only induces long-range magnetic order but also provides a unique opportunity to probe the electronic instabilities in the parent compound and thereby reveal the mechanism behind the metal-insulator transition itself.

A starting point for our REXS study has already been provided by previous neutron scattering work that detected $\mathbf{q} = (\frac{1}{4}, \frac{1}{4}, 0)$ and $(\frac{1}{4}, \frac{3}{4}, 0)$ superlattice peaks appearing below T_c for the 5% Mn system [4]. While this suggests the emergence of an electronic modulation and in particular of magnetic order, to specify its nature we need to establish if the modulation vector \mathbf{q} changes upon varying the Mn concentration beyond $x = 0.05$. In addition, to pinpoint the role of Mn impurities it is necessary to use an experimental tool, such as REXS, that can probe Ru and Mn selectively.

REXS is a relatively new spectroscopic technique to probe and study long-range charge/spin/orbital order in an element specific and direct way. REXS measurements were performed at beamlines 8.0.1 at ALS in Berkeley (Mn L -edges) and KMC-1 at BESSY in Berlin (Ru L -edges). In both cases we used a two-circle ultra-high-vacuum diffractometer in horizontal scattering geometry, with the incident photon beam polarized parallel to the diffraction plane (π). The scattered signal contained polarization components parallel (π') and perpendicular (σ') to the diffraction plane. $\text{Sr}_3(\text{Ru}_{1-x}\text{Mn}_x)_2\text{O}_7$ single crystals grown by the floating zone technique [4] were cut and polished along the (110) direction. The samples were mounted on cryogenic manipulators, allowing a cryostat polar angle rotation (θ) and also azimuthal rotation (ϕ) of the sample about the scattering vector, in the temperature range 20-300 K. Note that the diffraction peaks will be indexed with

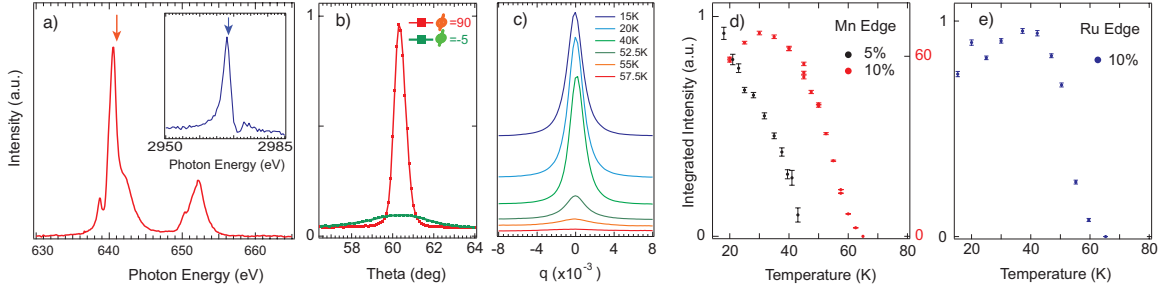


Figure 3.1: (a) Mn and Ru (inset) resonance profile for the $(\frac{1}{4}, \frac{1}{4}, 0)$ superlattice diffraction peak measured at 20 K on $\text{Sr}_3(\text{Ru}_{1-x}\text{Mn}_x)_2\text{O}_7$ with $x = 0.1$. The arrows at 641 and 2968 eV indicate the energies used in the REXS experiments. (b) 10 % Mn rocking curves (θ scans) for two different azimuthal angles measured at 641 eV and 20 K: $\phi = -5^\circ$ corresponds to $\sim(1/4, 1/4, l)$ scan probing the c -axis component of the order; $\phi = 90^\circ$ corresponds to a $(h, -k, 0)$ scan probing the ab in-plane component. At (c) 10 % Mn $(\frac{1}{4} + \Delta q, \frac{1}{4} + \Delta q, 0)$ momentum scans (θ - 2θ scans) at 641 eV for different temperatures. (d) Temperature dependence of the integrated intensity of the Mn-edge $(\frac{1}{4} + \Delta q, \frac{1}{4} + \Delta q, 0)$ momentum scans for $x = 5$ and 10 % samples. (e) Same as (d), for the $x = 10\%$ sample only, at the Ru edge.

respect to the undistorted tetragonal $I4/mmm$ unit cell with axes along the RuO bond directions ($a_0 = b_0 \simeq 3.9 \text{ \AA}$), while the magnetic and transport anisotropy will be discussed with reference to the 45° rotated and distorted orthorhombic $Bbcb$ unit cell of $\text{Sr}_3\text{Ru}_2\text{O}_7$ ($a^*, b^* \simeq 5.5 \text{ \AA}$) [6].

We performed REXS experiments on a range of Mn-substituted $\text{Sr}_3\text{Ru}_2\text{O}_7$ samples, at the Mn and Ru L -edges (for clarity, mostly data from 10 % Mn are shown in Fig. 3.1). For Mn concentration $x = 0.05$ and 0.1, this revealed a low-temperature structurally forbidden $\mathbf{q} = (\frac{1}{4}, \frac{1}{4}, 0)$ superlattice diffraction peak at the Mn L -edge. Similarly, experiments at the Ru L -edge on a 10 % sample detected $\mathbf{q} = (\frac{1}{4}, \frac{1}{4}, 0)$ and also $\mathbf{q} = (\frac{3}{4}, \frac{3}{4}, 0)$ reflections. Fig. 3.1(a) and its inset present the $(\frac{1}{4}, \frac{1}{4}, 0)$ resonance profile at $T = 20 \text{ K}$, i.e. the energy dependence of this superlattice peak intensity at the Mn $L_{2,3}$ and Ru L_2 -edges. Fig. 3.1(b) shows the Mn-edge $(\frac{1}{4}, \frac{1}{4}, 0)$ rocking curves at $T = 20 \text{ K}$, i.e. the θ -angle dependence of the intensity at 641 eV for different azimuthal angles ϕ (see inset of Fig. 3.2 for the experimental geometry). Since the peak width in momentum is proportional to the inverse of the correlation length, the sharp $q_{x,y}$ dependence (θ scan at $\phi = 90^\circ$) and the broad response in q_z (θ scan at $\phi = -5^\circ$) indicate a two-dimensional order with weak correlation along the c -axis. Lastly, the structurally forbidden reflections are detected only below the DC transport metal-insulator T_c , with a progressively increasing strength upon reducing temperature and increasing Mn concentration. This is shown in Fig. 3.1(c) for the 10 % Mn-edge $(\frac{1}{4} + \Delta q, \frac{1}{4} + \Delta q, 0)$ scan, and in Fig. 3.1(d,e) for the Mn and Ru-edge integrated peak intensities (at 641 and 2968 eV, respectively).

Altogether, the results in Fig. 3.1 demonstrate that the metal-insulator transition is

accompanied by a two-dimensional order with wavelength $2\sqrt{2}a_0$ and modulation vector \mathbf{q} along the diagonal of the $I4/mmm$ zone. The order is predominantly electronic and not structural (we did not observe corresponding superlattice reflections in non-resonant low-temperature x-ray diffraction), nor associated with the spatial ordering of the Mn impurities as evidenced by the doping independence of \mathbf{q} . The nature of this electronic order, i.e. spin/charge/orbital, can be further clarified by the detailed azimuthal-angle dependence of the integrated intensity of the Ru and Mn-edge $(\frac{1}{4}, \frac{1}{4}, 0)$ peaks. The results for the 10% Mn system are presented in Fig. 3.2, together with a theoretical angle dependence calculated for pure spin order [7], with spins parallel to the c -axis. The agreement between measured and calculated azimuthal dependence implies the primarily magnetic nature of the ordering, with average spin direction along the c -axis at both Ru and Mn sites.

To specify the exact pattern of the spin order, we should note that in addition to the above mentioned forbidden superlattice peaks, also a $\mathbf{q} = (\frac{1}{4}, \frac{5}{4}, 0)$ reflection was observed in our neutron scattering study on the $x = 0.05$ material [8]. Instead, no $\mathbf{q} = (\frac{1}{2}, \frac{1}{2}, 0)$ reflection was detected with either neutron or REXS at the Ru edge (at the Mn edge this

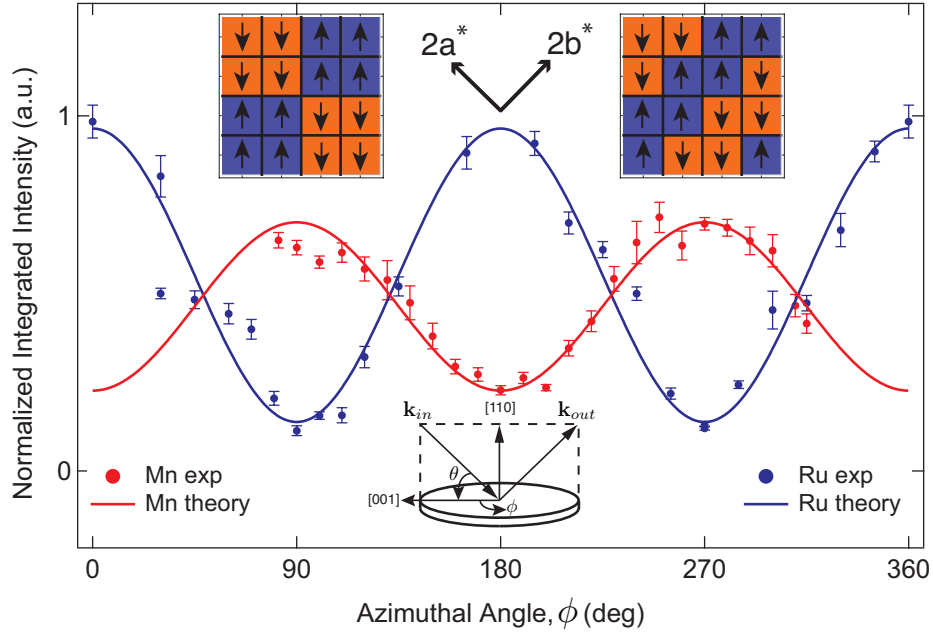


Figure 3.2: Azimuthal-angle dependence of the $(\frac{1}{4} + \Delta q, \frac{1}{4} + \Delta q, 0)$ momentum scan integrated intensity, at the Ru and Mn edge for the $x = 0.1$ sample. Both datasets are fitted to the formula $I_{(\frac{1}{4}, \frac{1}{4}, 0)}^{total} = I_{(\frac{1}{4}, \frac{1}{4}, 0)}^{\pi \rightarrow \sigma'} + I_{(\frac{1}{4}, \frac{1}{4}, 0)}^{\pi \rightarrow \pi'} \propto |\cos \theta \cos \phi|^2 + |\sin 2\theta \sin \phi|^2$. Due to the different Mn and Ru scattering angles ($\theta_{Mn} = 61.6^\circ$; $\theta_{Ru} = 10.9^\circ$), the ratio between $(\pi \rightarrow \sigma')$ and $(\pi \rightarrow \pi')$ scattering signals is also different and the maximum intensity position is shifted by 90° in ϕ . The experimental geometry and the two highest symmetry spin patterns consistent with the data are also shown.

\mathbf{q} value cannot be reached). These results enforce a very strong constraint on the possible spin texture but still allow for more than one compatible spin pattern. Among those, the most significant are the two highest symmetry ones, which due to the presence of domains (more below) would give rise to identical REXS patterns: a *checkerboard* antiferromagnetic ordering of square blocks of four parallel spins (Fig. 3.2, left inset); alternatively, an antiferromagnetic alternation of ferromagnetic *zigzag stripes* aligned diagonally with respect to the tetragonal $I4/mmm$ zone (Fig. 3.2, right inset). While the checkerboard pattern is isotropic with respect to the crystallographic a^* and b^* axes of the $Bbcb$ orthorhombic zone, the zigzag stripe pattern is not. Since this electronic anisotropy is appealing in relation to the reports of a nematic fluid phase in $\text{Sr}_3\text{Ru}_2\text{O}_7$ with $a^* - b^*$ resistive anisotropy in an applied magnetic field [3, 9, 10], let us continue by focusing on the zigzag stripe order; note, however, that the following discussion on the nature of the metal-insulator transition is independent of this choice.

Because of their coincidence in temperature, it seems natural to associate the metal-insulator transition with the onset of magnetic order induced by the Mn impurities. To further our understanding of the mechanism of the metal-insulator transition, we have studied the doping and temperature dependence of the width and intensity of the Mn-edge momentum scans, which provide an estimate of the magnetic-order correlation length and of the fraction of participating Mn impurities. Fig. 3.3(a) presents a comparison of the Mn-edge $(\frac{1}{4} + \Delta q, \frac{1}{4} + \Delta q, 0)$ momentum scans at 20 K for $x = 0.05$ and 0.1. As evidenced by the combination of normalized (main panel) and raw data (inset), both the integrated intensity and peak width are strongly enhanced (by factors of 10 and 4, respectively) upon increasing x from 5 to 10%. The detailed temperature dependence of the Mn-edge correlation length, defined as the inverse of the full-width half maximum (FWHM) of the momentum scans, is shown in Fig. 3.3(b) for both samples (similar correlation length results were obtained at the Ru-edge).

To start modelling this behavior, we should note that only the magnetically correlated Mn impurities contribute to the $(\frac{1}{4}, \frac{1}{4}, 0)$ scattering intensity at the Mn L -edge; calculations assuming a random distribution of Mn sites show that if 100% of the Mn impurities took part in the long-range spin order, as Mn doping is increased from 5 to 10% the diffraction peak integrated intensity should increase by a factor of about 4, i.e. nearly quadratically in the number of scattering centers [11]. The observed 10-fold increase implies that a much smaller fraction of the Mn moments are correlated for $x = 0.05$ and suggests the following scenario for the emergence of long-range magnetic order. At a sufficiently low temperature, each Mn impurity surrounds itself by a two-dimensional spin-ordered island, within the metallic RuO_2 plane. When these islands begin to overlap, the RuO-mediated exchange interaction can energetically favor a coherent spin arrangement between the islands and, as a result, the Mn impurities will interfere constructively. In the dilute 5% Mn regime, there are isolated Mn impurities whose spins are not participating in the order and will not contribute to the superlattice diffraction peak intensity; at 10% Mn concentration, however, there are statistically hardly any isolated Mn atoms and hence almost all them will contribute. As experimentally observed, the diffraction peak intensity would increase much faster than quadratically with increasing x .

It might appear surprising that a REXS signal is obtained from dilute, randomly dis-

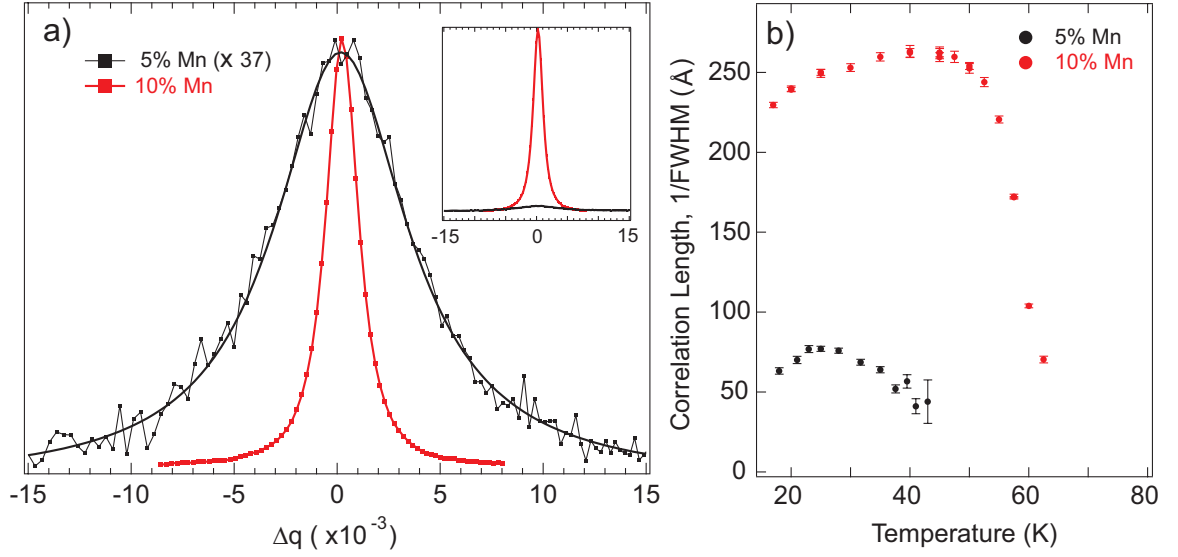


Figure 3.3: (a) Normalized Mn-edge ($\frac{1}{4} + \Delta q, \frac{1}{4} + \Delta q, 0$) momentum scans at 20 K for 5% (with Lorentzian fit) and 10% Mn concentration; raw data are shown in the inset. (b) Inverse FWHM of the momentum scans vs. temperature.

tributed Mn impurities. One should realize, however, that constructive interference is dependent not on the spatial location of the impurities, provided that the Mn atoms occupy substitutional Ru sites, but rather on the proper phase relation between their magnetic moments. This can be demonstrated with a simulation based on the correlation lengths obtained from the inverse of the FWHM of the experimental momentum scans (~ 55 and 235 \AA for 5 and 10% Mn concentration, respectively, at 20K). Fig. 7.5(a) presents a 40×40 RuO_2 lattice in real space, with 5% Mn sites each inducing a 4×4 unit of the zigzag stripe pattern (the simulation would identically apply to the case of the checkerboard ordering). Here, no correlation between the Mn spins has been imposed. As in Fig. 3.2, blue and red squares in Fig. 7.5(a) represent up and down spins along the c -axis, while the white patches are regions of the RuO_2 plane where no magnetism has been induced [the position of the Mn impurities and their corresponding spins are shown in Fig. 7.5(b)]. Due to the lack of correlation between the Mn spins, the Mn-edge ($\pm \frac{1}{4}, \pm \frac{1}{4}, 0$) peaks are extremely broad and weak, buried in the noisy background, as shown by the reciprocal space map of the scattering intensity in Fig. 7.5(c). The situation is very different for correlated Mn spins, as shown in Fig. 7.5(d,e,f) which presents the same sequence as panels (a,b,c), still for $x = 5\%$, but for an average cluster size of 55 \AA (~ 13 lattice spacing) as observed experimentally. The superlattice ($\pm \frac{1}{4}, \pm \frac{1}{4}, 0$) peaks are clearly discernible above the noise in Fig. 7.5(f). Note that this particular spin pattern also gives rise to $(\frac{2n+1}{4}, \frac{2n+1}{4}, 0)$ diffraction peaks, with n being an integer, but for the present discussion it is sufficient to restrict the field of view to $q_x, q_y = \pm 0.5 \pi/a_0$. For $x = 10\%$ and $\sim 235 \text{ \AA}$ magnetic islands (~ 57 lattice spacing), we can observe in Fig. 7.5(g,h,i) sharp diffraction spots with a peak height 30 times that of

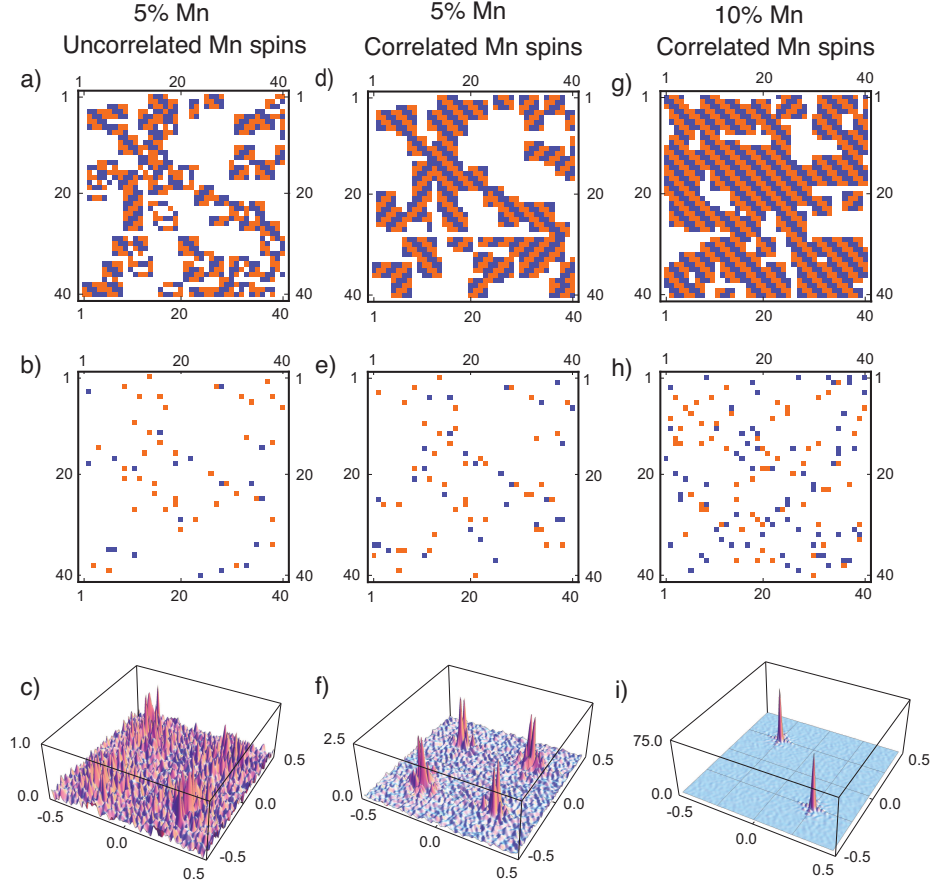


Figure 3.4: (a,d,g) Spin-ordered islands in the RuO_2 plane for various Mn contents and spin correlations: (a) 5% Mn, uncorrelated Mn spins; (d) 5% Mn, correlated Mn spins; (g) 10% Mn, correlated Mn spins. (b,e,h) Corresponding location of Mn impurities with up/down (blue/red) spins. (c,f,i) Reciprocal space map of the Mn scattering intensity generated by averaging over 200 random Mn-impurity distributions, of the kind in (b,e,h), to reduce noise.

$x=5\%$, in good agreement with the experimentally observed ~ 37 -fold increase (Fig. 3.3a). We should also note that $(-\frac{1}{4}, -\frac{1}{4}, 0)$ and $(\frac{1}{4}, \frac{1}{4}, 0)$ peaks are absent because the domain size is now larger than the lattice cell used for the simulation; in the real experiments they would be still visible.

We can now summarize our findings and try to establish a connection between long-range spin order and metal-insulator transition in $\text{Sr}_3(\text{Ru}_{1-x}\text{Mn}_x)_2\text{O}_7$, and possibly the magnetic fluctuations and nematic fluid behavior of the parent compound. Since $\text{Sr}_3\text{Ru}_2\text{O}_7$ does not show any long-range magnetic order, it is clear that the latter is induced by the $S=2$, $3d\text{-Mn}^{3+}$ impurities [4, 5].

Nevertheless, the ordering is independent of the precise 5-10% Mn concentration, sug-

gesting that the role of Mn is primarily that of triggering and/or stabilizing an instability incipient in the parent compound. Indeed, strong two-dimensional spin fluctuations have been observed in $\text{Sr}_3\text{Ru}_2\text{O}_7$ in zero field, which appear to cross over from ferro to antiferromagnetic upon reducing the temperature below 20 K [12]; and also a momentum-dependent spin anisotropy induced by spin-orbit coupling should be expected, as in Sr_2RuO_4 [13]. For both checkerboard and zigzag stripe spin patterns, the insulating behavior would result from the interaction of the propagating carriers with the ordered spin background. Note, however, that the zigzag stripe order would exhibit a marked transport anisotropy even in the absence of any applied field, with high and low conductivity behavior, respectively, along and perpendicular to the ferromagnetic stripes. In this latter case the macroscopic metal-insulator transition would thus depend on the formation of magnetic domains with different orientation. One might speculate that the transport anisotropy expected for a single zigzag stripe domain in $\text{Sr}_3(\text{Ru}_{1-x}\text{Mn}_x)_2\text{O}_7$, and the one detected in the parent compound in magnetic fields [3], could be fingerprints of the same nematic fluid instability [9, 10]; this however will require further scrutiny.

It should be emphasized that $\text{Sr}_3(\text{Ru}_{1-x}\text{Mn}_x)_2\text{O}_7$ in the dilute Mn substitution regime provides a unique opportunity to study with great accuracy the role of impurities and disorder in inducing phase separation, percolative, and glassy behavior in the general class of correlated oxides. For instance, it is interesting to note that the effective percolation threshold is achieved at $\lesssim 5\%$ Mn concentration [4]; in terms of magnetically correlated sites, as shown in Fig. 7.5(a,d) this corresponds to 50.2% of the RuO_2 plane, thus remarkably close to the threshold for classical metallic percolation on a square lattice which is suppressed at a 50% mixture of metallic and insulating bonds [14]. Furthermore, the non-monotonic temperature dependence of the correlation length presented in Fig. 3.3(b) has also been seen in reentrant spin glasses, due to the interplay of competing interactions and disorder [15, 16]. Finally, speculating on the much higher resonant enhancement observed at the Mn as compared to the Ru absorption edge (an at-least 36-fold enhancement should be expected due to the cross-section difference between $2p-3d$ and $2p-4d$ excitations), one might imagine using random impurities as a highly sensitive probe of spin/charge/orbital order of a host system that is difficult to access via the majority lattice population.

We thank M.Z. Hasan for the use of the ALS scattering chamber. This work is supported by ALS (M.A.H), Sloan Foundation (A.D.), CRC Program (A.D., G.A.S.), NSERC, CFI, CIFAR, and BCSI. ALS is supported by the U.S. DOE Contract No. DE-AC02-05CH11231.

Bibliography

- [1] S.I. Ikeda *et al.*, Phys. Rev. B **62**, R6089 (2000).
- [2] S.A. Grigera *et al.*, Science **294**, 329 (2001).
- [3] R.A. Borzi *et al.*, Science **315**, 214 (2007).
- [4] R. Mathieu *et al.*, Phys. Rev. B **72**, 092404 (2005).
- [5] M.A. Hossain *et al.*, Phys. Rev. Lett. **101**, 016404 (2008).
- [6] H. Shaked *et al.*, J. Solid State Chem. **154**, 361 (2000).
- [7] J.P. Hill and D.F. McMorrow, Acta Crystallogr., Sect. C: Found. Crystallogr. **52**, 236 (1996).
- [8] R. Mathieu, T. Arima, and Y. Tokura (unpublished).
- [9] S. Raghu *et al.*, Phys. Rev. B **79**, 214402 (2009).
- [10] W.C. Lee and C. Wu, arXiv:0902.1337 (2009).
- [11] M.W. Haverkort *et al.* (unpublished).
- [12] L. Capogna *et al.*, Phys. Rev. B **67**, 012504 (2003).
- [13] M.W. Haverkort *et al.*, Phys. Rev. Lett. **101**, 026406 (2008).
- [14] S. Kirkpatrick, Rev. Mod. Phys. **45**, 574 (1973).
- [15] H. Maletta *et al.*, Phys. Rev. Lett. **48**, 1490 (1982).
- [16] G. Aeppli *et al.*, Phys. Rev. B **28**, 5160 (1983).

Chapter 4

Nested Fermi surface and electronic instability in $\text{Ca}_3\text{Ru}_2\text{O}_7$

High resolution angular resolved photoemission data reveal well defined quasiparticle bands of unusually low weight, emerging in line with the metallic phase of $\text{Ca}_3\text{Ru}_2\text{O}_7$ below ~ 30 K. At the bulk structural phase transition temperature of 48 K, we find clear evidence for an electronic instability, gapping large parts of the underlying Fermi surface that appears to be nested. Metallic pockets are found to survive in the small, non-nested sections, constituting a low-temperature Fermi surface with two orders of magnitude smaller volume than in all other metallic ruthenates. The Fermi velocities and volumes of these pockets are in agreement with the results of complementary quantum oscillation measurements on the same crystal batches.¹

¹A version of this chapter has been published. Baumberger, F., Ingle, N.J.C., Kikugawa, N., Hossain, M.A., Meevasana, W., Perry, R.S., Shen, K.M., Lu, D.H., Damascelli, A., Rost, A., Mackenzie, A.P., Hussain, Z., and Shen, Z.-X. (2006) Nested Fermi Surface and Electronic Instability in $\text{Ca}_3\text{Ru}_2\text{O}_7$. *Physical Review Letters*. **96**: 107601.

The characterization and description of novel phases found in transition metal oxides (TMOs) has stimulated progress in condensed matter physics over the last decades [1]. The itinerant electron system of the perovskite ruthenium oxides provides a prime opportunity to study such complex ground states and phase transitions/competition in TMOs starting from a quasiparticle (QP) band structure picture [2]. Ruthenates can be grown with extremely high purity which has allowed detailed studies of the Fermi surface topology through the detection of quantum oscillations (QO) [3, 4], and Sr_2RuO_4 has served as a bench-mark system for the potential of angular resolved photoemission (ARPES) to derive quantitative information on band dispersion and QP scattering rates [5, 6]. Although these studies yielded fully consistent results, it should be noted that ARPES probes a larger energy scale, and can reveal information that is complimentary to low-temperature transport and thermodynamic measurements. While all Sr based ruthenates of the Ruddlesden-Popper series $(\text{Sr}/\text{Ca})_{n+1}\text{Ru}_n\text{O}_{3n+1}$ are metallic at low temperature, the situation becomes more ambiguous upon substitution of Sr with the isovalent, but smaller Ca ion. This causes structural distortions leading to a rotation and tilting of the RuO_6 octahedra, which in turn reduces hopping matrix elements and thus emphasizes correlation effects [8, 7]. The subject of this study, $\text{Ca}_3\text{Ru}_2\text{O}_7$, has been reported to be 'semi-metallic', with two phase transitions, a Neel transition at 56 K and a structural phase transition at 48 K, where the *in plane* resistivity increases by about 30%. At lower temperatures the resistivity is metallic, but very large [9, 13, 10].

In this paper, we report the growth of crystals with an order of magnitude lower residual resistivity than previously achieved, and high-resolution ARPES and QO measurements on them. We find an extremely small QP residue Z (fraction of spectral weight in the coherent quasiparticle excitation), extended parallel Fermi surface sections and a momentum dependent gap, opening at the bulk phase transition temperature. Comparison of Fermi volumes and velocities from the two techniques establishes the ground state of $\text{Ca}_3\text{Ru}_2\text{O}_7$ as a low carrier density metal. Together, the data indicate that the unusual ground state results from a Peierls-like electronic instability, gapping away large parts of the Fermi surface.

Photoemission experiments were performed with a Scienta SES 2002 spectrometer, using He I α radiation (21.22 eV) from a microwave driven monochromatized discharge lamp (Gammadata VUV5000). The differential pumping of the He leakage from the plasma chamber has been optimized to provide a partial pressure in the measurement chamber near the sensitivity limit of UHV ion-gauges, without restricting the large solid angle of $\approx 10^\circ$ collected by the refocussing toroidal monochromator. Energy and angular resolutions were set to 7.5 meV / $\pm 0.15^\circ$ for all measurements. Single crystals of $\text{Ca}_3\text{Ru}_2\text{O}_7$ with a residual *in-plane* resistivity below 100 $\mu\Omega\text{cm}$ were grown by a floating zone method [10], oriented by Laue diffraction and cleaved *in situ* at a pressure below 5×10^{-11} torr along the *ab*-plane. Samples cleaved at 10 K and 60 K yielded consistent results and the low-energy spectra showed minimal changes over the time span of a typical experimental run of 24 hours. Magnetoresistance and Hall effect were studied between 50 mK and 1 K in a dilution refrigerator / 15 T magnet.

Full details of our quantum oscillation and magneto-transport measurements will be published elsewhere, but to form a basis for comparison with the ARPES results we summarize them here. The Fermi surface consists of tiny, quasi-two-dimensional pockets of

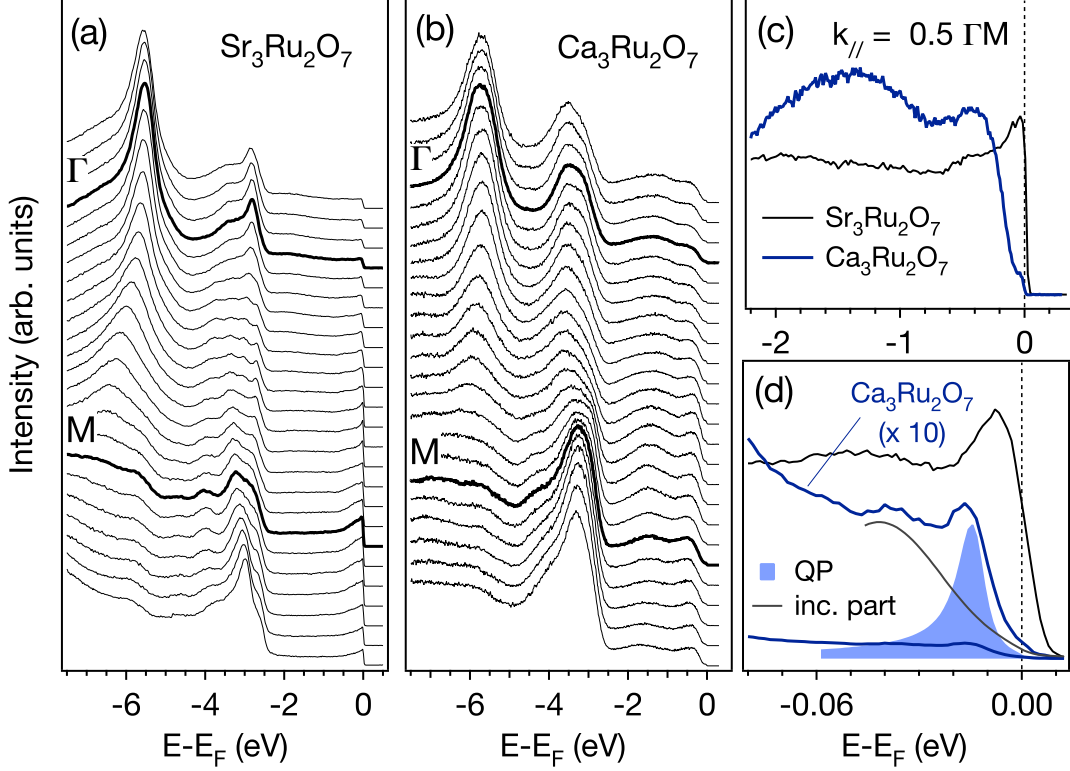


Figure 4.1: (a), (b) valence band spectra of $\text{Sr}_3\text{Ru}_2\text{O}_7$ and $\text{Ca}_3\text{Ru}_2\text{O}_7$ taken with equal momentum steps along ΓM ($h\nu = 21.2$ eV, $T = 10$ K). In (c), (d) spectra of the two compounds have been normalized to the total spectral weight of the valence band (integrated from 0 to -7 eV), and are compared on two different energy scales. A fit of the low energy weight assuming a FL-like QP on a rising incoherent part, indicates a self energy $\Sigma_I \approx 5$ meV at $E - E_F \approx 15$ meV.

electrons and holes, typical areas 0.3% of that of Brillouin zone (BZ). The measured quasiparticle effective masses correspond to Fermi velocities of approximately 5×10^4 m/s. The masses account, within experimental error, for the small electronic specific heat of 2.8 mJ/molK² which we measured on the same crystals, so we are confident that the QOs are probing the entire Fermi surface.

In Fig. 4.1, we compare the ARPES spectra of $\text{Ca}_3\text{Ru}_2\text{O}_7$ and $\text{Sr}_3\text{Ru}_2\text{O}_7$ over a large energy range. The isoelectronic nature upon substitution of Sr with Ca is clearly reflected in the spectra which show similar energies and dispersive behavior of the main valence band peaks. Despite this gross similarity of the lower valence states, there is a striking difference in the spectral function near the Fermi level (E_F). While $\text{Sr}_3\text{Ru}_2\text{O}_7$ shows intense quasiparticle peaks and multiple bands crossing the Fermi level, the spectral weight in $\text{Ca}_3\text{Ru}_2\text{O}_7$ is dramatically suppressed below ~ 150 meV and only a weak tail extends towards

E_F (Fig. 4.1(c)). For the rest of the paper, we will focus on this tail, which reflects the lowest lying excitations responsible for the transport and thermodynamic properties. The high resolution and stability of our spectrometer has allowed us for the first time to observe well defined quasiparticle bands, emerging on this faint tail below a temperature of ≈ 30 K, in line with the onset of coherent metallic transport in the ab -plane [9, 10]. These states exhibit an extremely low QP residue Z , over an order of magnitude lower than in $\text{Sr}_3\text{Ru}_2\text{O}_7$, indicative of strongly enhanced interactions, but remain sharply defined in energy. From fits to empirical spectral functions (see Fig. 4.1(d)), we estimate an intrinsic lifetime broadening $\Sigma_I \approx 5$ meV at binding energies around 15 - 20 meV, comparable to the value found for the intense quasiparticle peaks in the moderately correlated Fermi liquid compound Sr_2RuO_4 [5]. For a Fermi liquid with momentum independent self-energy, the QP spectral weight depends only on the mass-enhancement and therefore on the scattering rate. The observation of sharp QPs at energies > 15 meV with small Z thus points to strongly momentum, and possibly orbital dependent interactions ².

The momentum distribution of the spectral weight near E_F is shown in Figs. 2(a, b). These maps are often casually identified with the Fermi surface. However, the present case requires a more careful interpretation. Integrating the spectral weight over a typical energy range of $E_F \pm 12$ meV results in two dominant structures, as summarized in Fig. 4.2(c). A “*large square*” contour with rounded corners, connecting the M-points of the reduced orthorhombic BZ, and a smaller, more intense square composed of four broad triangular features. The identification of these contours as Fermi surface sheets would conflict with the QO-data, which indicate extremely small carrier pockets with an average volume of only 0.3% of the BZ. It is important to elucidate the origin of the apparent inconsistency, because large FS sheets are expected from band structure calculations [14] and were observed in the isovalent $\text{Sr}_3\text{Ru}_2\text{O}_7$ in LDA calculations [15], ARPES [16, 17] and de Haas-van Alphen data [4].

In Fig. 4.2(b), the spectral weight is integrated over a narrower energy range of ± 3 meV. Clearly, this suppresses the intense inner square contour, indicating that the constituting states are gapped and do not contribute to the Fermi surface. Extracting energy distribution curves (EDCs) at selected momentum points from the same data-set confirms this finding. The spectra at points 1–3 and 4–6, marked in Fig. 4.2(a), show weakly dispersing, faint QP peaks and a clear leading edge that is gapped by 5–9 meV (Fig. 4.2(d)). Next, we focus on the “*large square*” contour. Two sets of spectra, crossing it (7–9, 10–12) show tails extending up to E_F but a distinct leading edge with midpoints (LEM) clearly below the Fermi level. Metallic states with a LEM at the chemical potential are found only in the rounded edges of the “*large square*”, near the M-points. Summarizing the data of Fig. 4.2, we find a peak in the zero-frequency momentum distribution (bright spot in the Fermi surface map), coexisting with a leading edge gap. This behavior is characteristic for systems where an electronic instability such as a charge density wave or the formation of Cooper pairs opens a gap in the single particle excitation spectrum. Assuming a particle-hole symmetric but gapped band, the remnant intensity in the photoemission Fermi surface map can be identified with the underlying band structure *before* the instability gapped away most of

²Data taken at various photon energies between 16 eV and 41 eV showed a similarly low weight of the coherent QP.

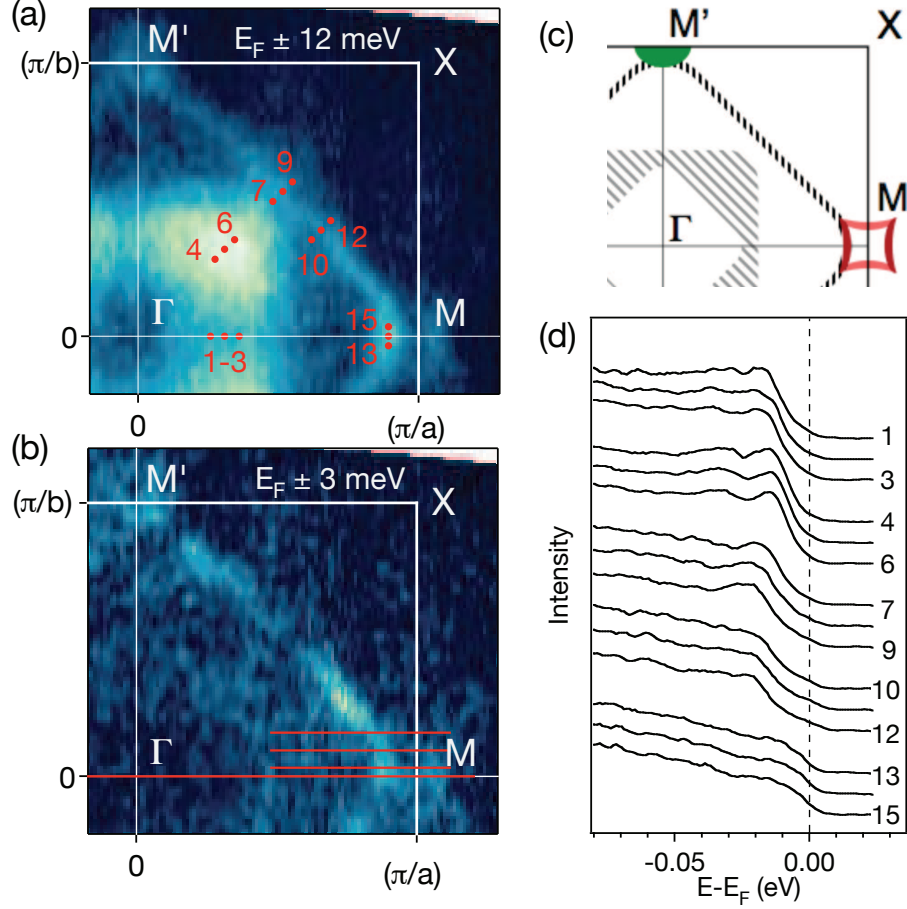


Figure 4.2: (a), (b) Momentum distribution of the lowest lying spectral weight in $\text{Ca}_3\text{Ru}_2\text{O}_7$ at $T = 9$ K. The two different energy windows correspond to effective resolutions of 25 meV and 10 meV, respectively. Red lines in (b) indicate momentum space locations of the dispersion plots in Fig. 4.3 (c) Schematic of the dominant features in the low energy excitations. The small Fermi arc near the M -point is back-folded by the proposed nesting vector to connect to a closed Fermi surface contour (see text). (d) Selected spectra, extracted from the data-set of (a),(b) demonstrating different gap sizes for various points in the BZ. Metallic states are found only in the vicinity of the M -points.

the FS [18]. The diamond shape seen in Fig. 4.2(b) suggests that the FS of $\text{Ca}_3\text{Ru}_2\text{O}_7$ is composed of quasi-1D $d_{xz,yz}$ orbitals, as detailed in the following letter. Strikingly, the detected underlying FS contour exhibits extended parallel sections and is almost perfectly nested with the vector $(\pi/a, \pi/b)$ corresponding to a real space periodicity of two Ru-Ru nearest neighbor distances. Based on this finding, we postulate the formation of a commensurate density wave below 48 K. This idea is fully consistent with the temperature

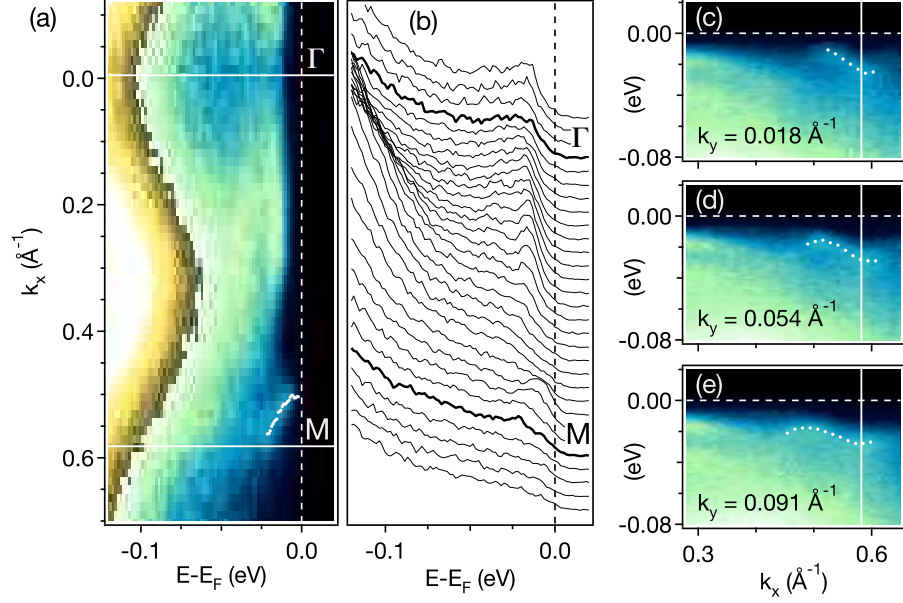


Figure 4.3: (a),(b) Dispersion of QP states along Γ M displayed as false color plot or stack of equally spaced EDCs, respectively. A metallic band is found near the M-point. White dots indicate the peak positions found from Lorentzian fits to MDCs. (c)–(e) are taken along the momentum space lines indicated in Fig. 4.2(b) and show in detail how the bands bend back and a gap opens as the nested part of the underlying FS is approached. White dots mark the peak positions in EDCs.

dependence of the gap, the QO data and the low electronic specific heat as will be shown later.

The postulate of a density wave in $\text{Ca}_3\text{Ru}_2\text{O}_7$, introducing the new periodicity of $(\pi/a, \pi/b)$ is further supported by the details of the quasiparticle dispersion, shown in Fig. 4.3. The dispersion of the metallic states in the rounded corners of the underlying FS is traced in Fig. 4.3(a) by white dots, obtained from Lorentzian fits of the momentum distribution curves (MDCs). The group velocity of $\approx 0.26 \text{ eV\AA}$ for this band is in good agreement with the estimate of $5 \times 10^4 \text{ m/s}$ (0.33 eV\AA) from the QOs. The evolution of the dispersion upon approaching the nested sections of the underlying FS is shown in Fig. 4.3(c)–(e). Moving away from the high symmetry line by as little as $0.09 \pi/b$ (Fig. 4.3(d)), the QP band starts to bend back and a gap of a few meV opens. This raises the intriguing question of how the Fermi level crossing around $0.88(\pi/a)$, seen in Fig. 4.3(a), connects to a closed FS-contour. Folding the rounded corner of the “large square” by the newly imposed periodicity corresponding to the nesting vector of $(\pi/a, \pi/b)$, we would expect a roughly square electron pocket centered at M with slightly concave edges, as sketched in Fig. 4.2(c). The volume of such a pocket can be estimated as $(0.12\pi/a)^2 \sim 0.36\% A_{BZ}$, assuming a simple square shape, in good agreement with the average FS-sheet volume deduced from

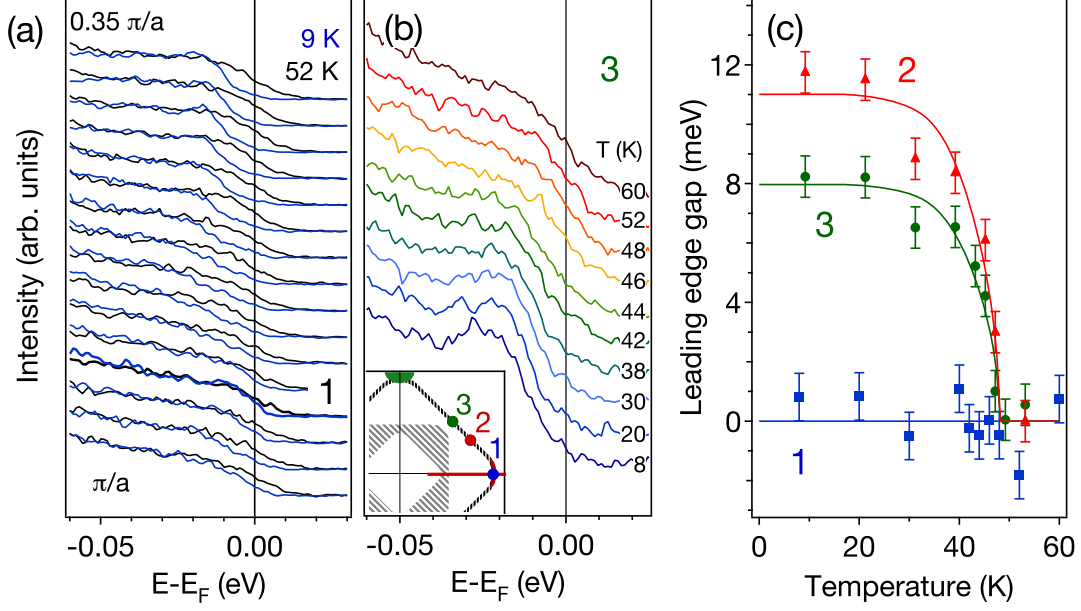


Figure 4.4: Temperature and momentum dependence of the gap. (a) shows spectra taken at 9 K and 52 K along the red line depicted in the BZ inset. (b) Temperature series of spectra at point '3'. (c) Evolution of the leading edge gap with temperature for momentum space points 1–3 with $(k_x, k_y) = (0.88\frac{\pi}{a}, 0)$; $(0.69\frac{\pi}{a}, 0.34\frac{\pi}{b})$; $(0.5\frac{\pi}{a}, 0.5\frac{\pi}{b})$, respectively.

the QOs. The apparent absence of the folded bands in the FS-map and dispersion plots does not disprove this model, since the intensity of folded bands in ARPES is proportional to the coupling responsible for the folding [18]. Taking the energy gap (~ 5 meV) as a measure of this coupling, and comparing it to typical band gap sizes (~ 0.5 eV), we expect a suppression of the folded bands to intensities clearly below a level detectable by ARPES. Additional metallic states are found near M' , but the band topology is less clear, in part because of the smaller BZ-dimension along b , which moves the zone boundary closer to the edge of the “large square” contour.

In Fig. 4.4, we show the temperature and momentum dependence of the gap. The direct comparison of spectra taken above and below the 48 K phase transition temperature along the high symmetry line ΓM (Fig. 4.4(a)) clearly demonstrates a significant momentum dependence in the low-temperature phase and confirms that the states in the corners of the low-energy square contour remain metallic: the highlighted spectra at point '1' show identical leading edge midpoints, which coincide within the experimental error with the Fermi level. The evolution of the low-energy spectral weight with temperature is shown in Fig. 4.4(b) for point '3' marked in the BZ-inset. The spectral line shape does not change significantly at the Néel transition temperature of 56 K, and only a minor redistribution

of weight occurs at 48 K. This is consistent with the weak perturbation, expected from a symmetry breaking ordering with low phase transition temperature and small gap. More pronounced changes of the spectral function are observed below 35 K, where sharply defined, faint QP peaks emerge. Notably this coincides with the onset of metallic transport, roughly 10 K below the structural phase transition temperature [10], rather than with the transition temperature itself.

Leading edge gaps Δ_{LE} were obtained from empirical fits to the data, and are shown in Fig. 4.4(c). The opening of the gap is observed at 48.3 K, in perfect agreement with the bulk structural phase transition temperature of 48 K³. No hysteresis was observed within the experimental errors of ~ 2 K. The gap opens to a full size of $\Delta_{LEG} = 10 - 12$ meV at low temperature. It is thus of the same order of magnitude as the mean-field value for the Peierls-gap of $2\Delta = 3.5 kT$ (14.6 meV at 48 K), but significantly smaller than the value of ~ 0.1 eV, reported previously from an analysis of Raman data from flux grown crystals [19].

The nested Fermi surface and the above described temperature dependence of the gap suggest that the unusual ground state of $\text{Ca}_3\text{Ru}_2\text{O}_7$ does not result from an orbital selective Mott transition, as it has been proposed for $\text{Ca}_{2-x}\text{Sr}_x\text{RuO}_4$ [7], but originates from the interaction with spin, orbital or lattice degrees of freedom and bears some resemblance to a Peierls transition. Although much of the data reported in this letter is consistent with weak coupling theory, we found several spectroscopic signatures which point beyond a nesting driven Peierls-instability. The very small Z and the coexistence of heavy, non-nested bands which become similarly gapped at 48 K with a dispersive nested band suggest a more complex picture where strong and possibly orbital dependent interactions are present. Whether the observed electronic instability is the consequence or the driving force of the simultaneous structural and magnetic phase transition remains ambiguous, as does the nature of the symmetry breaking ordering, which we propose from the observed nesting vector of $(\pi/a, \pi/b)$ and the gapping of all nested states. It is hoped that the present work stimulates neutron- or x-ray diffraction studies which can give direct evidence for ordering of lattice, spin or orbital degrees of freedom. The latter has been proposed independently from recent Raman scattering, magnetization and transport measurements [20, 21].

We thank G. Wigger and J. Denlinger for helpful discussions. This work has been supported by the ONR grant N00014-01-1-0048. Additional support from SSRL is provided by the DOE's office of Basic Energy Science, Division of Material Science with Contract DE-FG03-OIER45929-A001.

³The given temperatures may contain an absolute error of about 2 K at temperatures around 48 K, due to the unknown gradient within sample and sample-holder.

Bibliography

- [1] M. Imada, A. Fujimori, and Y. Tokura, *Rev. Mod. Phys.* **70**, 1039 (1998).
- [2] A.P. Mackenzie and Y. Maeno, *Rev. Mod. Phys.* **75**, 657 (2003).
- [3] A.P. Mackenzie *et al.*, *Phys. Rev. Lett.* **76**, 3786 (1996).
- [4] R.A. Borzi *et al.*, *Phys. Rev. Lett.* **92**, 216403 (2004).
- [5] N.J.C. Ingle *et al.*, *Phys. Rev. B* **72**, 205114 (2005).
- [6] A. Damascelli *et al.*, *Phys. Rev. Lett.* **85**, 5194 (2000).
- [7] V.I. Anisimov *et al.*, *Eur. Phys. J. B* **25**, 191 (2002).
- [8] S. Nakatsuji and Y. Maeno, *Phys. Rev. Lett.* **84**, 2666 (2000).
- [9] Y. Yoshida *et al.*, *Phys. Rev. B* **69**, 220411(R) (2004).
- [10] N. Kikugawa *et al.*, unpublished.
- [11] L. Capogna *et al.*, *Phys. Rev. Lett.* **88**, 076602 (2002).
- [12] Y. Yoshida *et al.*, *Phys. Rev. B* **72**, 054412 (2005).
- [13] E. Ohmichi *et al.*, *Phys. Rev. B* **70**, 104414 (2004).
- [14] D.J. Singh, and S. Auluck, submitted, 2005.
- [15] D.J. Singh and I.I. Mazin, *Phys. Rev. B* **63**, 165101 (2001).
- [16] A.V. Puchkov *et al.*, *Phys. Rev. Lett.* **81**, 2747 (1998a).
- [17] A.V. Puchkov, Z.X. Shen, and G. Cao, *Phys. Rev. B* **58**, 6671 (1998b).
- [18] J. Voit *et al.*, *Science* **290**, 501 (2000).
- [19] H.L. Liu *et al.*, *Phys. Rev. B* **60**, 6980(R) (1999).
- [20] J.F. Karpus *et al.*, *Phys. Rev. Lett.* **93**, 167205 (2004).
- [21] G. Cao *et al.*, *N. J. Phys.* **6**, 159 (2004).

Chapter 5

In-situ doping control of the surface of high- T_c cuprates

Central to the understanding of high- T_c superconductivity is the evolution of the electronic structure as doping alters the density of charge carriers in the CuO_2 planes. Superconductivity emerges along the path from a normal metal on the overdoped side to an antiferromagnetic insulator on the underdoped side. This path also exhibits a severe disruption of the overdoped, normal metal's Fermi surface [1, 2, 3]. Angle-resolved photoemission spectroscopy (ARPES) on the surfaces of easily cleaved materials such as $\text{Bi}_2\text{Sr}_2\text{CaCu}_2\text{O}_{8+\delta}$ shows that in zero magnetic field the Fermi surface breaks up into disconnected arcs [4, 5, 6]. However, in high magnetic field, quantum oscillations at low temperatures in $\text{YBa}_2\text{Cu}_3\text{O}_{6.5}$ [7] indicate the existence of small Fermi surface pockets [8, 9, 10, 11, 12, 13, 14, 15, 16, 17, 18]. Reconciling these two phenomena through ARPES studies of $\text{YBa}_2\text{Cu}_3\text{O}_{7-\delta}$ (YBCO) has been hampered by the surface sensitivity of the technique [19, 20, 21]. Here we show that this stems from the polarity and resulting self-doping of the YBCO surface. By in-situ deposition of potassium atoms on cleaved YBCO, we can continuously control the surface doping and follow the evolution of the Fermi surface from the overdoped to the underdoped regime. The present approach opens the door to new systematic studies of high- T_c cuprates, such as creating new electron-doped superconductors from insulating parent compounds. ¹

¹A version of this chapter has been published. Hossain, M.A., Mottershead, J.D.F., Fournier, D., Bostwick, A., McChesney, J.L., Rotenberg, E., Liang, R., Hardy, W.N., Sawatzky, G.A., Elfimov, I.S., Bonn, D.A., and Damascelli, A. (2008) In situ doping control of the surface of high-temperature superconductors. *Nature Physics*. 4: 527-531.

In the heavily overdoped regime, angular magnetoresistance oscillation [1] and ARPES experiments [2, 3] on $Tl_2Ba_2CuO_{6+\delta}$ have arrived at a quantitative consensus in observing a large hole-like Fermi surface (FS). Upon reducing the number of holes in the CuO_2 planes, the FS volume decreases in the manner expected by Luttinger's theorem, but below optimal doping the single-particle FS appears to reduce to four disconnected nodal Fermi arcs. This scenario was suggested from ARPES studies of Bi-cuprates [4, 5] and $Ca_{2-x}Na_xCuO_2Cl_2$ [6], and is thought to be connected to the existence of the pseudogap. The detection of quantum oscillations in oxygen-ordered ortho-II YBCO6.5 suggests a different scenario involving FS reconstruction into hole and/or electron pockets [7, 9, 10]. These two pictures are derived from quite different measurement techniques, performed on different materials, and under conditions of high magnetic field in one case, but zero field in the other. Due to the complex multiband and correlated character of the electronic structure of YBCO6.5 [11], the determination of the nature of these pockets and their generality to the underdoped cuprates requires connecting transport and single-particle spectroscopy information on the same underdoped system. The study of YBCO6.5 by ARPES is thus crucial. Unfortunately, this material is complicated by the lack of a natural [001] cleavage plane (Fig. 5.1a) and also by the presence of CuO -chain layers. More specifically, YBCO cleaves between the CuO chain

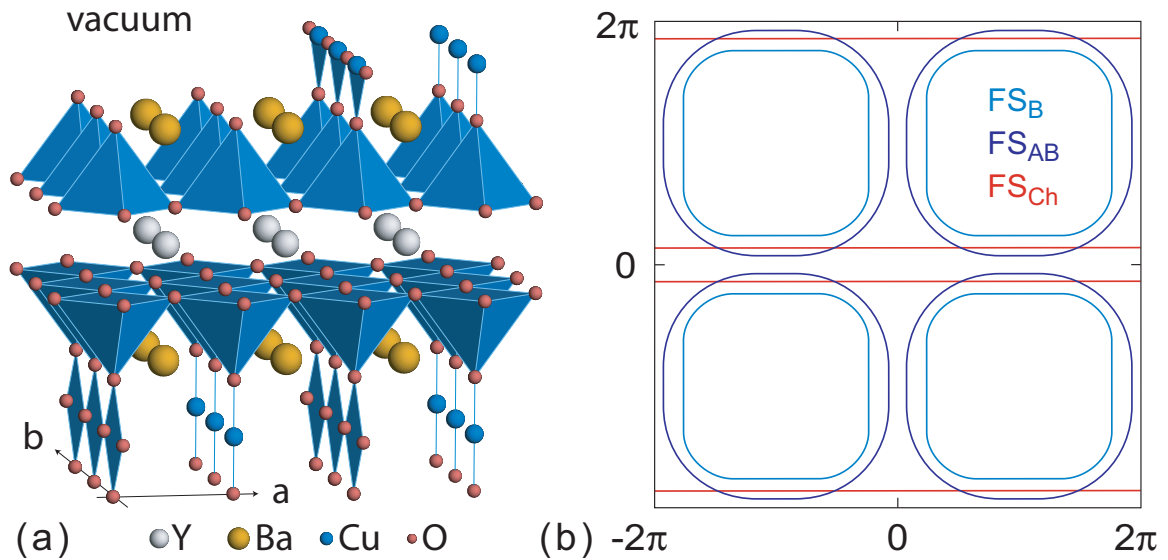


Figure 5.1: **The surface of cleaved YBCO.** (a) Structure of oxygen-ordered YBCO6.5 (with alternating oxygen full and empty chains), showing the BaO and CuO chain terminations of the cleaved surface. Electronic reconstruction takes place at these polar surfaces, similar to the prototypical case of a polar catastrophe in ionic insulators with a $|1 + |1 - |1 + |1 - | \dots$ layer-by-layer charge [25]. This leads to ‘overdoped-like’ FS features for the surface topmost layers, as shown pictorially in (b) for CuO_2 -plane bonding and antibonding bands (FS_B and FS_{AB}), and the one-dimensional CuO chain band (FS_{Ch}).

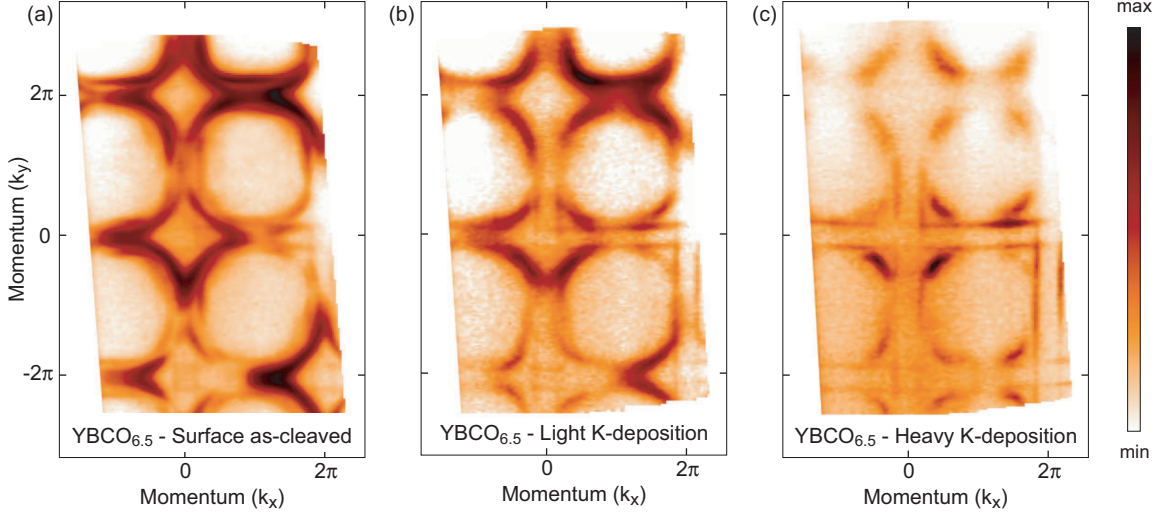


Figure 5.2: **YBCO FS evolution upon e^- doping.** (a) ARPES FS of as-cleaved YBCO6.5, exhibiting an effective hole doping $p = 0.28$ per planar Cu atom, as determined from the average area of bonding and antibonding CuO_2 -bilayer FSs. (b,c) By evaporating potassium on the same sample (< 1 monolayer), electrons are transferred to the top-most CuO_2 bilayer and the corresponding FSs become progressively more hole-underdoped. (c) For heavy K-deposition ($p = 0.11$ as estimated from the area of the chain FS), the E_F ARPES intensity reduces to the 1D CuO chain FS and four disconnected nodal CuO_2 FS arcs.

layer and the BaO layer, leaving on the cleaved surface relatively large regions ($> 100 \text{ \AA}$) of either CuO or BaO terminations. Scanning-tunneling microscopy shows that the CuO chain terraces are characterized by prominent surface density waves [22] and differ substantially from the bulk: as also seen in ARPES [19], they exhibit surface states and unavoidable doping disorder. Recent ARPES studies of nearly optimally doped YBCO indicated that surfaces terminating in either a CuO and BaO layer give different contributions to the total photoemission intensity [21], and that the doping of the top-most CuO_2 planes is $p = 0.3$, almost irrespective of the nominal bulk doping. This corresponds to heavy overdoping, all the way into the non-superconducting regime (Fig. 5.4), and is actually not achievable in bulk, fully-oxygenated YBCO7.0 for which $p = 0.194$ [23]. Similar problems have been encountered in the ARPES study of $\text{YBa}_2\text{Cu}_4\text{O}_8$ [24].

Overcoming these problems requires, first of all, recognizing that the cleaved surface of YBCO is actually polar. This can lead to overdoped-like FSs (Fig. 5.1b) due to reconstruction of the electronic states [25]. A wide momentum distribution map of the FS from ‘as-cleaved’ YBCO6.5 is presented in Fig. 5.2a (see also Methods). The ARPES data are a superposition of features from the BaO and CuO terminated regions: because of the few \AA electron escape depth at these photon energies, the ARPES intensity from the BaO-terminated regions is dominated by the CuO_2 -bilayer bands and that from the

CuO-terminated regions by the chain band. The comparison with Fig. 5.1b, allows one to identify the FS features originating from the CuO₂-plane bonding and antibonding bands (FS_B and FS_{AB}), and the one-dimensional (1D) CuO chain band (FS_{Ch}). Note that the strong momentum-dependent intensity modulation of the ARPES features, which seems inconsistent with the sample symmetry, is simply a manifestation of the matrix elements effects associated with the photon/crystal/electron geometry changing across the field of view (no symmetrization was performed). Also, this particular ortho-II sample happened to be twinned, in the bulk and not just on the surface, as confirmed by x-ray diffraction (this has an effect on FS_{Ch} but not on the discussion of the four-fold symmetric Fermi arcs). Most importantly, the fit of the two-dimensional ARPES FSs over multiple zones returns the following areas, counting electrons, relative to the Brillouin zone area $A_{BZ} = 4\pi^2/ab$: the bonding Fermi surface area FS_B = 46.2%, the antibonding FS_{AB} = 26.0%, and the chain surface FS_{Ch} = 13.8%. From the average of bonding and antibonding FS areas, one can calculate the hole-doping $p = 0.28 \pm 0.01$ per planar copper ($p = 0$ for the 1/2-filled Mott insulator with 1 hole per Cu atom). As summarized in the phase diagram of Fig. 5.4, this indicates that the self-doping of the YBCO6.5 polar surface is that of a heavily-overdoped, non-superconducting cuprate.

The next step is that of actively controlling the self-doping of the surface, so as to reduce its hole content to that of underdoped, bulk YBCO6.5. This can be achieved by in-situ evaporation of potassium onto the cleaved surface (see also Methods): owing to the low ionization potential, K¹⁺ ions are adsorbed on the surface and electrons are doped into the top-most layers. As a consequence, we would anticipate the evolution of all detected features towards the underdoped regime of hole-doped cuprates, which is precisely what one can observe in Fig. 5.2, from panel a to c, upon increasing the K¹⁺ concentration (i.e., decreasing the hole doping). The doping is indeed changing according to an increase in electron filling (all data were acquired on the same sample after subsequent K evaporations). This is evidenced by the continuous FS_{Ch} area increase (counting electrons), which evolves from FS_{Ch} = 13.8% for the as-cleaved surface to FS_{Ch}^{K1} = 14.7% and FS_{Ch}^{K2} = 16.6% for the increasingly K-deposited YBCOK1 (Fig. 5.2b) and YBCOK2 (Fig. 5.2c). By comparing the carrier concentration per chain-Cu measured by the FS_{Ch} area with the results of ab-initio LDA band structure calculations [11], we can estimate the corresponding hole-doping per planar-Cu. This way we find good agreement with the value $p = 0.28$ already estimated for as-cleaved YBCO6.5 from the average of FS_B and FS_{AB}. Most importantly, however, we obtain a hole-doping $p^{K1} = 0.20$ and $p^{K2} = 0.11$ for YBCOK1 and YBCOK2, which means that the surface of YBCOK2 is very close to the doping level $p = 0.097$ of bulk YBCO6.5.

The most interesting aspect of the data in Fig. 5.2 is the evolution of the CuO₂-plane features. For heavy K deposition (Fig. 5.2c), the LDA-like CuO₂-bilayer bonding and antibonding FSs of overdoped YBCO have collapsed into four nodal Fermi arcs, consistent with other underdoped cuprates [6, 4, 5]. This is accompanied by the complete suppression of CuO₂ antinodal spectral intensity as well as nodal bilayer splitting, which in contrast were clearly resolved for as-cleaved YBCO6.5 (Fig. 5.2a). Their disappearance with K deposition hints at a severe loss of coherence upon underdoping. Correspondingly the CuO₂ nodal Fermi wavevectors, relative to the Brillouin zone diagonal (0,0)-(π , π), have evolved from $k_F^{AB} = 0.29$ and $k_F^B = 0.36$ for ‘overdoped’ as-cleaved YBCO6.5, to a single $k_F^{K2} = 0.40$ for

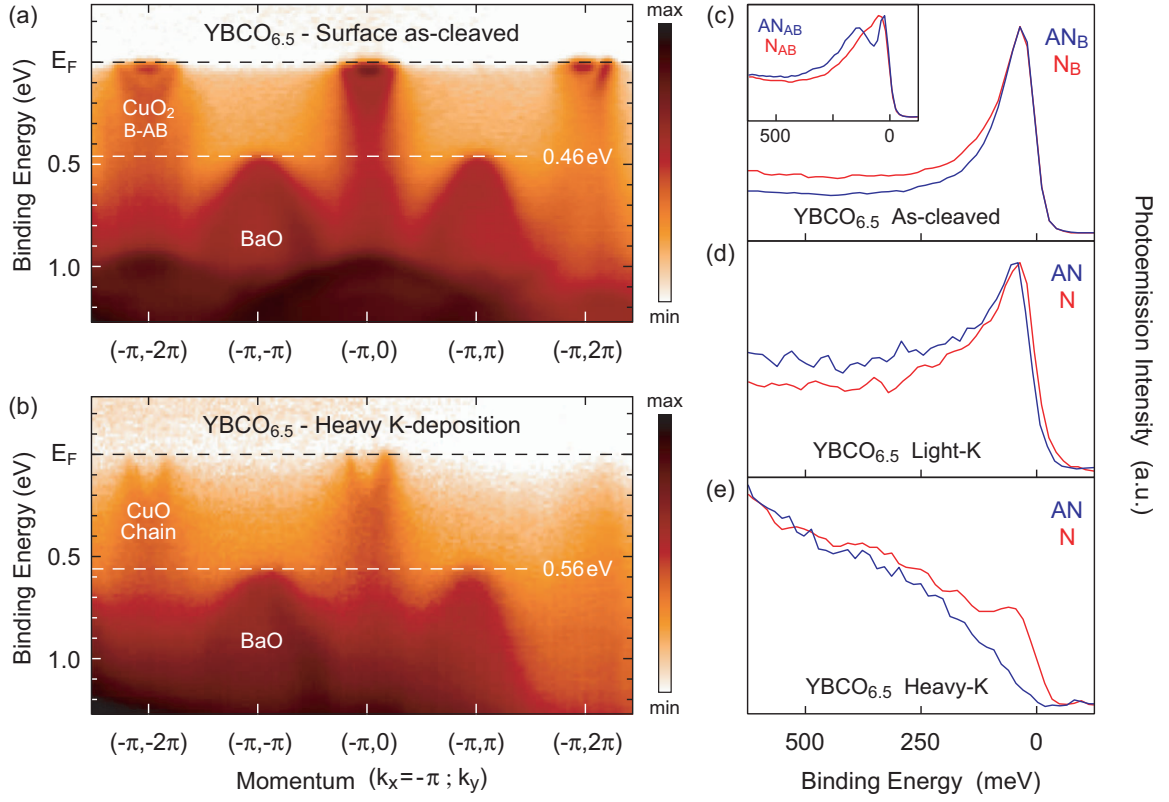


Figure 5.3: **YBCO dispersion and EDC evolution upon e^- doping.** (a,b) The BaO band high-energy shift in YBCOK2 as compared to YBCO6.5 reveals that electrons are added upon K deposition; also, bonding (B) and antibonding (AB) CuO_2 features vanish at the antinodes and only the CuO chain band is detected. (c-e) Nodal (N) and antinodal (AN) k_F EDCs showing the progressive opening of an AN gap and loss of CuO_2 -plane quasiparticle coherence upon underdoping ($\Delta \sim 10$ and 80 meV for YBCOK1 and YBCOK2); the B and AB splitting is resolved only for as-cleaved YBCO6.5.

‘underdoped’ YBCOK2. These numbers compare well to what has been observed on other cuprates at similar dopings (note that the following are both single CuO_2 -layer systems): $k_F = 0.36$ and 0.41 , respectively, for overdoped ($p = 0.26$) $\text{Tl}_2\text{Ba}_2\text{CuO}_{6+\delta}$ [2] and underdoped ($p = 0.12$) $\text{Ca}_{2-x}\text{Na}_x\text{CuO}_2\text{Cl}_2$ [6].

The transfer of electrons to the surface of YBCO upon K deposition is also confirmed by an inspection of the electronic dispersions along the $(-\pi, -2\pi)$ - $(-\pi, 2\pi)$ direction (corresponding momentum-distribution curves are shown in the Supplementary Information). On $p = 0.28$ as-cleaved YBCO6.5 (Fig. 5.3a), we detect well-defined bonding and antibonding CuO_2 bands crossing E_F at the antinodes, as well as the BaO band with a maximum binding energy at the zone corners $(-\pi, \pm\pi)$. On underdoped $p = 0.11$ YBCOK2 (Fig. 5.3b), the BaO band is located ~ 100 meV deeper in energy. This indicates a shift of the chemical

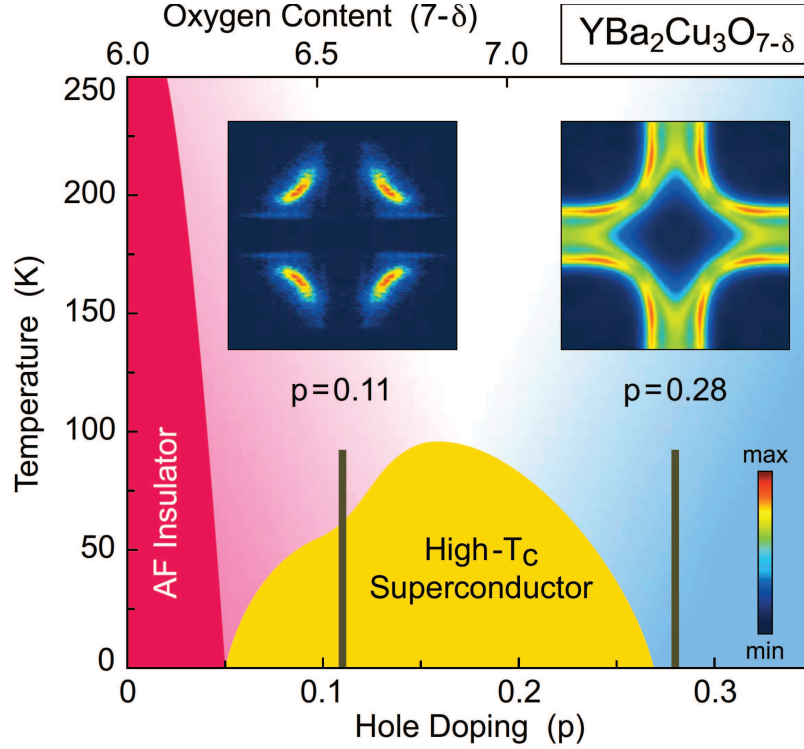


Figure 5.4: **Phase diagram of YBCO by ARPES.** Schematic temperature-doping phase diagram of YBCO adapted from Ref. [7]. The hole doping p per planar copper ($p = 0$ for the $1/2$ -filled Mott insulator with 1 hole per Cu atom), and the corresponding oxygen content ($7-\delta$), are indicated on bottom and top axes [23]. The ARPES FS for under- and overdoped YBCO is also shown; the momentum-distribution maps have been 2-fold and 4-fold symmetrized for $p = 0.11$ and 0.28 , respectively. Similar to the data in Fig. 5.2, the doping levels were determined for $p = 0.11$ from the area of FS_{Ch} , and for $p = 0.28$ from the area of FS_B and FS_{AB} .

potential consistent with the transfer of electrons from adsorbed K atoms to the top-most BaO, CuO-chain, and CuO₂-plane layers. On YBCOK2 the only coherent feature detected at the antinodes is the 1D CuO chain band; the antinodal CuO₂-plane spectral weight has now become fully incoherent. The nodal and antinodal energy-distribution curves (EDCs) in Fig. 5.3(c-e) clearly show that the progressive loss of quasiparticle coherence with K deposition is very similar to what is observed on other cuprates upon hole underdoping [2, 6, 4, 5]. Most importantly, while metallic behavior is observed on as-cleaved YBCO6.5, a leading-edge antinodal gap $\Delta \sim 10$ and 80 meV is detected for YBCOK1 and YBCOK2, respectively. This is consistent with YBCO being superconducting for $p = 0.11$ and 0.20 but not 0.28 (Fig. 5.4 – the experiments were all performed at $T = 20$ K), and allows us to conclude that the properties of K-deposited YBCO surfaces are representative of the bulk.

We now summarize our findings, illustrated by the phase diagram and symmetrized FS data for YBCO_{K2} and as-cleaved YBCO_{6.5} in Fig. 5.4. Our study demonstrates that the self-hole-doping of the cleaved polar surfaces of YBCO can be controlled by the in-situ evaporation of alkali metals, in the present case K. This novel approach paves the way for the study of this important material family – across the whole phase diagram – by single particle spectroscopies. As this material has been the gold standard in a number of seminal bulk-sensitive studies of the normal and superconducting properties, the direct connection with single-particle spectroscopy can lead to an understandable underdoped anchor point, analogous to $\text{Tl}_2\text{Ba}_2\text{CuO}_{6+\delta}$ in the overdoped regime [3]. The results obtained for $p=0.11$ YBCO_{K2} establish that the ARPES FS of underdoped YBCO consists of the superposition of 1D CuO chain FS and CuO₂-plane-derived nodal Fermi arcs. It is thus consistent, with the additional complication of the chains, to what has already been observed in oxychloride [6] and Bi-cuprates [4, 5]. In this sense, the disruption of the large hole-like coherent FS in underdoped cuprates is a truly universal phenomenon.

Having obtained the first momentum resolved FS data for underdoped YBCO, it becomes crucial to understand the connection between ARPES and quantum oscillation results [7, 10]. First, the detection of the BaO band maximum at ~ 0.5 eV below E_F rules out the scenario coming from LDA band structure calculations, which suggested that the small Fermi surface found in the quantum oscillation measurements might originate from small pockets produced by BaO-Cu_{chain} bands at $(\pm\pi, \pm\pi)$ [11, 12]. We also did not observe any signature of CuO₂-derived band folding arising from the ortho-II oxygen-ordering of the chains [11, 12], which is possibly consistent with the loss of three-dimensional coherence evidenced by the suppression of bilayer band splitting upon underdoping.

Recent measurements of the Hall resistance in high magnetic field have noted a sign change with decreasing temperature [9], suggesting that the quantum oscillations seen on top of a negative Hall coefficient might come from small electron pockets, rather than the hole pockets originally proposed [7]. However, there is no sign of such electron pockets in our ARPES data from underdoped YBCO_{K2}, nor are there signs of additional zone-folding due to the kinds of density wave instabilities that might give rise to such a Fermi surface reconstruction [8, 9, 15].

If any pocket had to be postulated on the basis of the present ARPES data, the most obvious possibility would be that the Fermi arcs are in fact hole-like nodal Fermi pockets, as obtained for light doping of the antiferromagnetic parent compound in self-consistent Born calculations [26] and already speculated from the study of other underdoped cuprates [6, 4, 5]. The lack of a finite ARPES intensity on the outer side of the pockets would be consistent with the strong drop in the quasiparticle coherence $Z_{\mathbf{k}}$ expected beyond the antiferromagnetic zone boundary [27, 13]. To estimate an area for these ostensible nodal pockets, we can fold the detected arc profile, either with respect to the antiferromagnetic zone boundary or the end points of the arc itself, obtaining values of either 2.6% or 1.3%, relative to the full Brillouin zone area $A_{BZ} = 4\pi^2/ab$. These numbers compare relatively well with the pocket area 1.9% suggested on the basis of quantum oscillation experiments on bulk YBCO_{6.5} [7, 10]. However, these are hole, not electron pockets. Thus, the interpretation of high field measurements in terms of electron and hole pockets differs markedly from single particle spectroscopy on the same material, suggesting that the high magnetic field might

be inducing a state different from that being studied in zero field.

Whatever the solution to the puzzle outlined above, it should be emphasized that the present approach, based on the in-situ alkaline metal evaporation on freshly cleaved surfaces, opens the door to this type of manipulation of other cuprates and complex oxides, not only to control the self-doping of polar surfaces but also to reach doping levels otherwise precluded in the bulk. For instance, one could try to underdope the surface of $Tl_2Ba_2CuO_{6+\delta}$, which grows naturally overdoped [3], or even to obtain an electron-doped superconductor starting from the insulating parent compounds.

Methods

Sample preparation. $YBa_2Cu_3O_{6+x}$ single crystals were grown in non-reactive $BaZrO_3$ crucibles using a self-flux technique. The CuO_x chain oxygen content was set to $x = 0.51$ by annealing in a flowing $O_2:N_2$ mixture and homogenized by further annealing in a sealed quartz ampoule, together with ceramic at the same oxygen content. After mounting for the cleave required in an ARPES measurement, the samples were cooled from $100^\circ C$ to room temperature over several days to establish the ortho-II superstructure ordering of the CuO_x chain layer [28]. The particular sample used in the present study was twinned, as confirmed by x-ray diffraction after the ARPES measurements.

ARPES experiments. ARPES measurements were carried out on the Electronic Structure Factory endstation at Beamline 7.01 of the Advanced Light Source (ALS). The data were measured with linearly-polarized 110 eV photons and a Scienta R4000 electron analyzer in angle-resolved mode. YBCO6.5 single crystals were cleaved in situ at a base pressure better than 2.5×10^{-11} torr and then oriented by taking fast Fermi surface scans. Several procedures were tried out on these samples in an attempt to suppress the surface contribution to the total photoemission intensity and gain direct insight into the bulk electronic structure. For instance, samples were temperature-cycled between 20 and 100 K or were cleaved at higher temperature (~ 80 K) and then cooled down to 20 K [29], in order to age and/or vary the characteristics of the cleaved surfaces. While both procedures have proved successful in measuring the bulk dispersion and FS of layered Sr_2RuO_4 [29], no effect was observed in the case of YBCO6.5. Successful control of the self-doping of the cleaved surfaces was achieved by in-situ deposition of submonolayers of potassium, with a commercial SAES getter source [30], on freshly cleaved YBCO6.5. In this latter case, the samples were kept at 20 K at all times during the cleaving, K-deposition, and ARPES measurements (temperature dependent measurements could not be performed because of the need of maintaining the most stable experimental conditions over extended time, during and between subsequent K evaporations). All ARPES data shown in Fig. 5.2, 5.3, and 5.4 were obtained on the same sample, i.e. as-cleaved and after two subsequent K evaporations. Energy and angular resolutions were set to ~ 30 meV and 0.2° ($\pm 15^\circ$ angular window) for the data in Fig. 5.2 and 5.3, and to ~ 30 meV and 0.1° ($\pm 7^\circ$ angular window) for the higher-quality FS mappings in Fig. 5.4. The Fermi surface maps of Fig. 5.2 and 5.4 were obtained by integrating the ARPES intensity over a 30 meV energy window about E_F , and then by normalizing the intensity maps relative to one another for display purposes. A more quan-

titative comparison of the ARPES intensity for as-cleaved and K-deposited surfaces is given in the Supplementary Information on the basis of the analysis of momentum-distribution curves (MDCs), which shows an overall intensity suppression by a factor of 4.4 and 7.2 for low and high K coverage, with respect to the as-cleaved surface.

Author information

Correspondence and requests for materials should be addressed to A. Damascelli (damascelli@physics.ubc.ca).

Acknowledgments

We gratefully acknowledge J. van den Brink for insightful discussions. This work was supported by the Alfred P. Sloan Foundation (A.D.), an ALS Doctoral Fellowship (M.A.H.), the CRC Program (A.D. and G.A.S), NSERC, CFI, CIFAR Quantum Materials, and BCSI. The Advanced Light Source is supported by the Director, Office of Science, Office of Basic Energy Sciences, of the U.S. Department of Energy under Contract No. DE-AC02-05CH11231.

Author contributions

M.A.H. and J.D.F.M. contributed equally to this work.

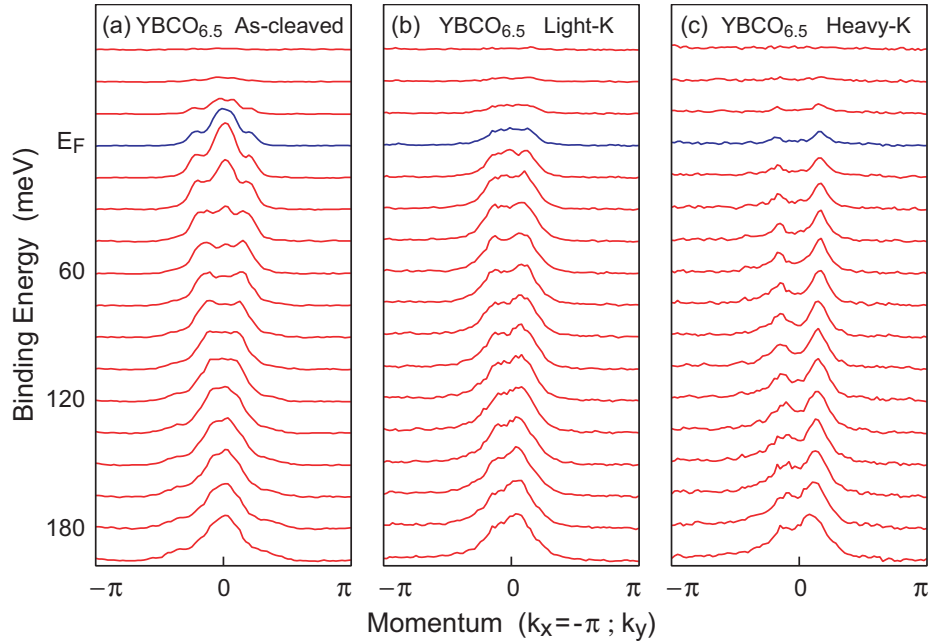


Figure 5.5: **YBCO MDC evolution upon e^- doping.** MDCs measured on (a) as-cleaved and (b,c) K-deposited YBCO6.5, along the same momentum-space direction of the EDCs shown in Fig. 5.3(a,b), yet limited to the $k_x = -\pi$ and $k_y = [-\pi, \pi]$ range. The energy step between adjacent MDCs is of 15 meV. Also note that, due to the relative peak/background intensity decrease upon K deposition, the MDCs for YBCOK1 and YBCOK2 have been rescaled by a factor of 4.4 and 7.2, respectively, with respect to those of as-cleaved YBCO6.5.

Supplementary information

The analysis of the E -vs.- k ARPES intensity map and EDCs in Fig. 5.3 can also be extended to the corresponding momentum-distribution curves (MDCs), which confirms what already noticed. The MDCs for as-cleaved YBCO6.5, YBCOK1, and YBCOK2 are shown in Fig. 5.5. For overdoped ($p=0.28$) as-cleaved YBCO6.5, the MDCs are characteristic of an antinodal signal dominated by bonding and antibonding CuO_2 bands (Fig. 5.5a). The single peak at 180 meV corresponds to approximately the bottom of the bonding band, and evolves into two symmetric peaks with respect to $k_y=0$ upon approaching E_F , as expected for a parabolic dispersion. Closer to the Fermi energy ($E_B \lesssim 60$ meV), a second more intense peak is detected, which corresponds to the antibonding band bottom and also splits in two upon crossing E_F . As potassium is deposited on the cleaved YBCO6.5 surface, the peak-to-background intensity ratio progressively decreases (the MDCs were multiplied by 4.4 and 7.2 for YBCOK1 and YBCOK2). Although the overall background is increasing, the MDCs' widths are still well defined without evident sign of further broadening, suggesting that the doping evolution of the ARPES response is not dominated by disorder arising from the adsorption of potassium. In addition, the intensity associated with the CuO_2 bands decreases and the CuO chains start instead to dominate the antinodal response (Fig. 5.5b). It is very obvious that on YBCOK2 the only detectable features come from the parabolic CuO-chain dispersion (Fig. 5.5c), which is substantially deeper than that of the CuO_2 plane bands (two distinct MDC peaks are still observable at 180 meV in Fig. 5.5c, as opposed to the single one in Fig. 5.5a). Finally, one should note that the E_F ($\pi,0$) weight is progressively decreasing, consistent with the reduction of quasiparticle coherence and the opening of the antinodal gap, as discussed in the context of Fig. 5.3.

Bibliography

- [1] Hussey, N.E. , Abdel-Jawad, M., Carrington, A., Mackenzie, A.P. & Ballcas, L. A coherent three-dimensional Fermi surface in a high-transition-temperature superconductor. *Nature* **425**, 814-817 (2003).
- [2] Platé, M. *et al.* Fermi surface and quasiparticle excitations of overdoped $\text{Tl}_2\text{Ba}_2\text{CuO}_{6+\delta}$ by ARPES. *Phys. Rev. Lett.* **95**, 077001 (2005).
- [3] Peets, D. C. *et al.* $\text{Tl}_2\text{Ba}_2\text{CuO}_{6+\delta}$ brings spectroscopic probes deep into the overdoped regime of the high- T_c cuprates. *New Journ. Physics* **9**, 1-32 (2007).
- [4] Norman, M. R. *et al.* Destruction of the Fermi surface in underdoped high- T_c superconductors. *Nature* **392**, 157-160 (1998).
- [5] Kanigel, A. *et al.* Evolution of the pseudogap from Fermi arcs to the nodal liquid. *Nature Physics* **2**, 447-451 (2006).
- [6] Shen, K. M. *et al.* Nodal quasiparticles and antinodal charge ordering in $\text{Ca}_{2-x}\text{Na}_x\text{CuO}_2\text{Cl}_2$. *Science* **307**, 901-904 (2005).
- [7] Doiron-Leyraud, N. *et al.* Quantum oscillations and the Fermi surface in an underdoped high- T_c superconductor. *Nature* **447**, 565-568 (2007).
- [8] Balakirev, F. F. *et al.* Fermi surface reconstruction at optimum doping in high- T_c superconductors. Preprint at <http://arxiv.org/abs/0710.4612> (2007).
- [9] LeBoeuf, D. *et al.* Electron pockets in the Fermi surface of hole-doped high- T_c superconductors. *Nature* **450**, 533-536 (2007).
- [10] Jaudet, C. *et al.* de Haas-van Alphen oscillations in the underdoped cuprate $\text{YBa}_2\text{Cu}_3\text{O}_{6.5}$. Preprint at <http://arxiv.org/abs/0711.3559> (2007).
- [11] Elfimov, I. S., Sawatzky, G. A. & Damascelli, A. Fermi pockets and correlation effects in underdoped $\text{YBa}_2\text{Cu}_3\text{O}_{6.5}$. *Phys. Rev. B* **77**, 060504(R) (2008) .
- [12] Carrington, A. & Yelland, E. A. Band-structure calculations of Fermi-surface pockets in ortho-II $\text{YBa}_2\text{Cu}_3\text{O}_{6.5}$. *Phys. Rev. B* **76**, 140508(R) (2007).
- [13] Harrison, N., McDonald, R. D. & Singleton, J. Cuprate Fermi orbits and Fermi arcs: the effect of short-range antiferromagnetic order. *Phys. Rev. Lett.* **99**, 206406 (2007).

-
- [14] Chen, W.-Q., Yang, K.-Y., Rice, T. M. & Zhang, F. C. Quantum oscillations in magnetic field induced antiferromagnetic phase of underdoped cuprates : application to ortho-II $\text{YBa}_2\text{Cu}_3\text{O}_{6.5}$. *Europhys. Lett.* **82**, 17004 (2008).
- [15] Millis, A. J. & Norman, M. Antiphase stripe order as the origin of electron pockets observed in 1/8-hole-doped cuprates. *Phys. Rev. B* **76**, 220503(R) (2007).
- [16] Chakravarty, S. & Kee, H.-Y. Fermi pockets and quantum oscillations of the Hall coefficient in high temperature superconductors. Preprint at <http://arxiv.org/abs/0710.0608> (2007).
- [17] Alexandrov, A. S. Theory of quantum magneto-oscillations in underdoped cuprate superconductors. Preprint at <http://arxiv.org/abs/0711.0093> (2007).
- [18] Melikyan, A., Vafek, O. Quantum oscillations in the mixed state of d -wave superconductor. Preprint at <http://arxiv.org/abs/0711.0776> (2007).
- [19] Schabel, M. C. *et al.* Angle-resolved photoemission on untwinned $\text{YBa}_2\text{Cu}_3\text{O}_{6.95}$. I. Electronic structure and dispersion relations of surface and bulk bands. *Phys. Rev. B* **57**, 6090 (1998).
- [20] Lu, D. H. *et al.* Superconducting gap and strong in-plane anisotropy in untwinned $\text{YBa}_2\text{Cu}_3\text{O}_{7-d}$. *Phys. Rev. Lett.* **86**, 4370 (2001).
- [21] Zabolotnyy, V. B. *et al.* Momentum and temperature dependence of renormalization effects in the high-temperature superconductor $\text{YBa}_2\text{Cu}_3\text{O}_{7-d}$. *Phys. Rev. B* **76**, 064519 (2007).
- [22] Derro, D. J. *et al.* Nanoscale one-dimensional scattering resonances in the CuO chains of $\text{YBa}_2\text{Cu}_3\text{O}_{6+x}$. *Phys. Rev. Lett.* **88**, 097002 (2002).
- [23] Liang, R., Bonn, D. A. & Hardy, W. N. Evaluation of CuO_2 plane hole doping in $\text{YBa}_2\text{Cu}_3\text{O}_{6+x}$ single crystals. *Phys. Rev. B* **73**, 180505 (2006).
- [24] Kondo, T. *et al.* Dual character of the electronic structure of $\text{YBa}_2\text{Cu}_4\text{O}_8$: the conduction bands of CuO_2 planes and CuO chains. *Phys. Rev. Lett.* **98**, 157002 (2007).
- [25] Hesper, R., Tjeng, L. H., Heeres, A. & Sawatzky, G. A. Photoemission evidence of electronic stabilization of polar surfaces in K_3C_{60} . *Phys. Rev. B* **62**, 16046-16055 (2000).
- [26] Sushkov, O. P., Sawatzky, G. A., Eder, R. & Eskes, H. Hole photoproduction in insulating copper oxide. *Phys. Rev. B* **56**, 11769-11776 (1997).
- [27] Eskes, H. & Eder, R. Hubbard model versus t - J model: the one-particle spectrum. *Phys. Rev. B* **54**, 14226-14229 (1996).
- [28] Liang, R., Bonn, D. A. & Hardy, W. N. Preparation and x-ray characterization of highly ordered ortho-II phase $\text{YBa}_2\text{Cu}_3\text{O}_{6.50}$ single crystals. *Physica C* **336**, 57-62 (2000).

-
- [29] Damascelli, A. *et al.* Fermi surface, surface states, and surface reconstruction in Sr_2RuO_4 . *Phys. Rev. Lett.* **85**, 5194-5197 (2000).
- [30] Ohta, T., Bostwick, A., Seyller, T., Horn, K. & Rotenberg, E. Controlling the electronic structure of bilayer graphene. *Science* **313**, 951-954 (2006).

Chapter 6

Two gaps make a high-temperature superconductor?

One of the keys to the high-temperature superconductivity puzzle is the identification of the energy scales associated with the emergence of a coherent condensate of superconducting electron pairs. These might provide a measure of the pairing strength and of the coherence of the superfluid, and ultimately reveal the nature of the elusive pairing mechanism in the superconducting cuprates. To this end, a great deal of effort has been devoted to investigating the connection between the superconducting transition temperature T_c and the normal-state pseudogap crossover temperature T^* . Here we present a review of a large body of experimental data which suggests a coexisting two-gap scenario, i.e. superconducting gap and pseudogap, over the whole superconducting dome. We will focus on spectroscopic data from cuprate systems characterized by $T_c^{max} \sim 95$ K, such as $\text{Bi}_2\text{Sr}_2\text{CaCu}_2\text{O}_{8+\delta}$, $\text{YBa}_2\text{Cu}_3\text{O}_{7-\delta}$, $\text{Tl}_2\text{Ba}_2\text{CuO}_{6+\delta}$, and $\text{HgBa}_2\text{CuO}_{4+\delta}$, with particular emphasis on the Bi-compound which has been the most extensively studied with single-particle spectroscopies.

1

¹A version of this chapter has been published. Hüfner, S., Hossain, M.A., Damascelli, A., Sawatzky, G.A. (2008) Two Gaps Make a High-Temperature Superconductor? Reports on Progress in Physics. **71**: 062501.

Since their discovery [1], the copper-oxide high- T_c superconductors (HTSCs) have become one of the most investigated class of solids [?]. However, despite the intense theoretical and experimental scrutiny, an understanding of the mechanism that leads to superconductivity is still lacking. At the very basic level, what distinguishes the cuprates from the conventional superconductors is the fact that they are doped materials, the highly atomic-like Cu $3d$ orbitals give rise to strong electron correlations (e.g., the undoped parent compounds are antiferromagnetic Mott-Hubbard-like insulators), and the superconducting elements are weakly-coupled two-dimensional layers (i.e., the celebrated square CuO_2 planes). Among the properties that are unique to this class of superconducting materials, in addition to the unprecedented high superconducting T_c , the normal-state gap or *pseudogap* is perhaps the most noteworthy. The pseudogap was first detected in the temperature dependence of the spin-lattice relaxation and Knight shift in nuclear magnetic resonance and magnetic susceptibility studies [25]. The Knight shift is proportional to the density of states at the Fermi energy; a gradual depletion was observed below a cross-over temperature T^* , revealing the opening of the pseudogap well above T_c on the underdoped side of the HTSC phase diagram (Fig. 6.1). As the estimates based on thermodynamic quantities are less direct than in spectroscopy we will, in the course of this review, mainly concentrate on spectroscopic results; more information on other techniques can be found in the literature [5].

As established by a number of spectroscopic probes, among which primarily angle-resolved photoemission spectroscopy [26, 27], the pseudogap manifests itself as a suppression of the normal-state electronic density of states at E_F exhibiting a momentum dependence reminiscent of a $d_{x^2-y^2}$ functional form. For hole-doped cuprates, it is largest at Fermi momenta close to the antinodal region in the Brillouin zone - i.e. around $(\pi, 0)$ - and vanishes along the nodal direction - i.e. the $(0, 0)$ to (π, π) line. Note however that, strictly speaking, photoemission and tunneling probe a suppression of spectral weight in the single-particle spectral function, rather than directly of density of states; to address this distinction, which is fundamental in many-body systems and will not be further discussed here, it would be very interesting to investigate the quantitative correspondence between nuclear magnetic resonance and single-particle spectroscopy results. Also, no phase information is available for the pseudogap since, unlike the case of optimally and overdoped HTSCs [28], no phase-sensitive experiments have been reported for the underdoped regime where $T^* \gg T_c$. As for the doping dependence, the pseudogap T^* is much larger than the superconducting T_c in underdoped samples, it smoothly decreases upon increasing the doping, and seems to merge with T_c in the overdoped regime, eventually disappearing together with superconductivity at doping levels larger than $x \sim 0.27$ [9, 10, 5, 16, 13, 14, 11, 7, 8, 19, 6, 23, 12, 15, 17, 18, 20, 21, 22, 24].

In order to elaborate on the connection between pseudogap and high- T_c superconductivity, or in other words between the two energy scales E_{pg} and E_{sc} identified by T^* and T_c respectively, let us start by reminding that in conventional superconductors the onset of superconductivity is accompanied by the opening of a gap at the chemical potential in the one-electron density of states. According to the Bardeen-Cooper-Schrieffer (BCS) theory of superconductivity [29], the gap energy provides a direct measure of the binding energy of the two electrons forming a Cooper pair (the two-particle bosonic entity that characterizes the superconducting state). It therefore came as a great surprise that a gap, i.e. the pseu-

dogap, was observed in the HTSCs not only in the superconducting state as expected from BCS, but also well above T_c . Because of these properties and the hope it might reveal the mechanism for high-temperature superconductivity, the pseudogap phenomenon has been very intensely investigated. However, no general consensus has been reached yet on its origin, its role in the onset of superconductivity itself, and not even on its evolution across the HTSC phase diagram.

As discussed in three recent papers on the subject [12, 15, 17], and here summarized in Fig. 6.1, three different phase diagrams are usually considered with respect to the pseudogap line. While Millis [15] opts for a diagram like in Fig. 6.1a, Cho [17] prefers a situation where the pseudogap line meets the superconducting dome at $x \simeq 0.16$ (Fig. 6.1b,c); Norman et al. [12] provide a comprehensive discussion of the three different possibilities. One can summarize some of the key questions surrounding the pseudogap phenomenon and its relevance to high-temperature superconductivity as follows:[12, 15, 17]

1. Which is the correct phase diagram with respect to the pseudogap line?
2. Does the pseudogap connect to the insulator quasiparticle spectrum?
3. Is the pseudogap the result of some one-particle band structure effect?
4. Or, alternatively, is it a signature of a two-particle pairing interaction?
5. Is there a true order parameter defining the existence of a pseudogap phase?
6. Do the pseudogap and a separate superconducting gap coexist below T_c ?
7. Is the pseudogap a necessary ingredient for high- T_c superconductivity?

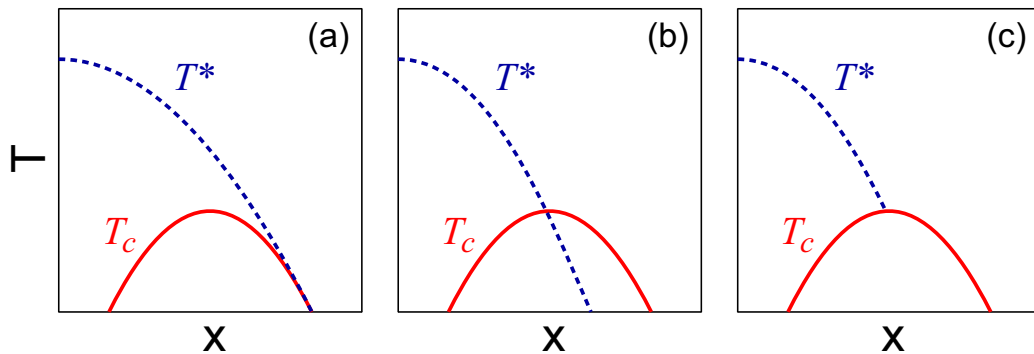


Figure 6.1: Various scenarios for the interplay of pseudogap (blue dashed line) and superconductivity (red solid line) in the temperature-doping phase diagram of the HTSCs. While in (a) the pseudogap merges gradually with the superconducting gap in the strongly overdoped region, in (b) and (c) the pseudogap lines intersects the superconducting dome at about optimal doping (i.e., maximum T_c). In most descriptions, the pseudogap line is identified with a crossover with a characteristic temperature T^* rather than a phase transition; while at all dopings $T^* > T_c$ in (a), beyond optimal doping $T^* < T_c$ in (b) and T^* does not even exist in (c). Adapted from Ref.[12].

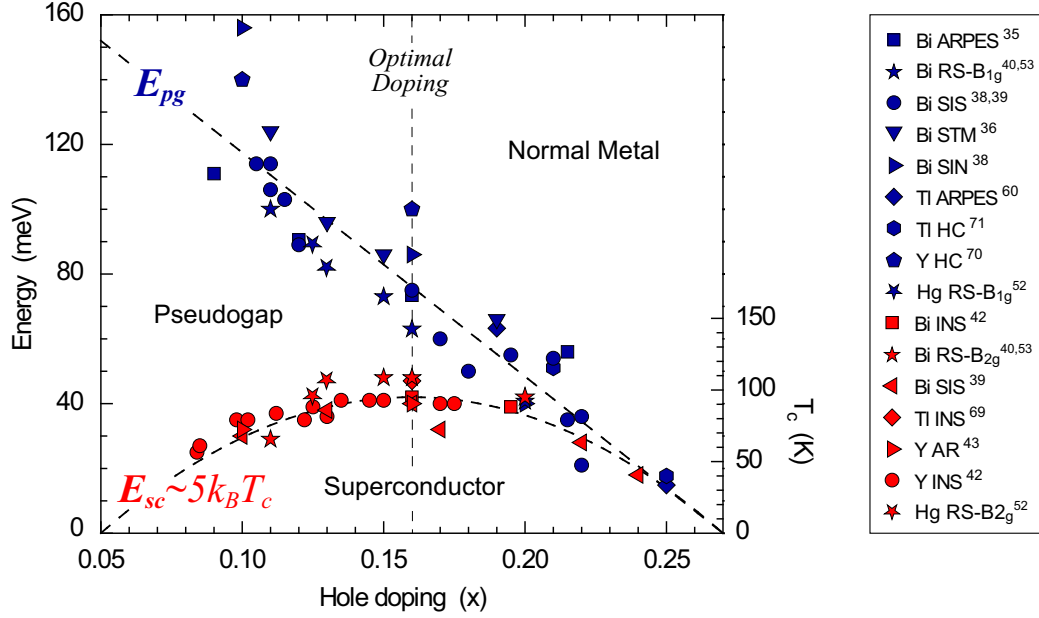


Figure 6.2: Pseudogap ($E_{pg} = 2\Delta_{pg}$) and superconducting ($E_{sc} \sim 5k_B T_c$) energy scales for a number of HTSCs with $T_c^{max} \sim 95$ K (Bi2212, Y123, Tl2201, and Hg1201). The datapoints were obtained, as a function of hole doping x , by angle-resolved photoemission spectroscopy (ARPES), tunneling (STM, SIN, SIS), Andreev reflection (AR), Raman scattering (RS), and heat conductivity (HC). On the same plot we are also including the energy Ω_r of the magnetic resonance mode measured by inelastic neutron scattering (INS), which we identify with E_{sc} because of the striking quantitative correspondence as a function of T_c . The data fall on two universal curves given by $E_{pg} = E_{pg}^{max}(0.27 - x)/0.22$ and $E_{sc} = E_{sc}^{max}[1 - 82.6(0.16 - x)^2]$, with $E_{pg}^{max} = E_{pg}(x = 0.05) = 152 \pm 8$ meV and $E_{sc}^{max} = E_{sc}(x = 0.16) = 42 \pm 2$ meV (the statistical errors refer to the fit of the selected datapoints; however, the spread of all available data would be more appropriately described by ± 20 and ± 10 meV, respectively).

In this communication we will revisit some of these questions, with specific emphasis on the one- vs. two-gap debate. Recently, this latter aspect of the HTSCs has been discussed in great detail by Goss Levi [30], in particular based on scanning-tunneling microscopy data from various groups [31, 32, 33]. Here we will expand this discussion to include the plethora of experimental results available from a wide variety of techniques. We will show that one fundamental and robust conclusion can be drawn: the HTSC phase diagram is dominated by two energy scales, the superconducting transition temperature T_c and the pseudogap crossover temperature T^* , which converge to the very same critical point at the end of the superconducting dome. Establishing whether this phenomenology can be conclusively described in terms of a coexisting two-gap scenario, and what the precise nature of the gaps would be, will require a more definite understanding of the quantities measured by

Optimally doped Bi2212 ($T_c \sim 90\text{-}95\text{ K}$)			
Experiment	Energy	meV	Ref.
ARPES - $(\pi, 0)$ peak	E_{pg}	80	[34, 35]
Tunneling - STM		70	[18, 36]
Tunneling - SIN		85	[37]
Tunneling - SIS		75	[38, 39]
Raman - B_{1g}		65	[40]
Electrodynamics		80	[5, 41]
Neutron - $(\pi, \pi) \Omega_r$	E_{sc}	40	[42]
Raman - B_{2g}		45	[40]
Andreev		45	[43]
SIS - dip		40	[39]

Table 6.1: Pseudogap E_{pg} and superconducting E_{sc} energy scales (2Δ) as inferred, for optimally doped Bi2212, from different techniques and experiments. Abbreviations are given in the main text, while the original references are listed.

the various probes.

Emerging phenomenology

The literature on the HTSC superconducting gap and/or pseudogap is very extensive and still growing. In this situation it seems interesting to go over the largest amount of data obtained from as many experimental techniques as possible, and look for any possible systematic behavior that could be identified. This is the primary goal of this focused review. We want to emphasize right from the start that we are not aiming at providing exact quantitative estimates of superconducting and pseudogap energy scales for any specific compound or any given doping. Rather, we want to identify the general phenomenological picture emerging from the whole body of available experimental data [9, 5, 16, 13, 18, 44, 45, 38, 39, 46, 37, 36, 47, 48, 49, 50, 51, 52, 40, 53, 35, 54, 55, 56, 57, 58, 59, 60, 61, 62, 63, 34, 64, 65, 66, 67, 41, 42, 68, 69, 70, 71, 43, 72].

In the following, we will consider some of the most direct probes of low-energy, electronic excitations and spectral gaps, such as angle-resolved photoemission (ARPES), scanning tunneling microscopy (STM), superconductor/insulator/normal-metal (SIN) and superconductor/insulator/superconductor (SIS) tunneling, Andreev reflection tunneling (AR), and Raman scattering (RS), as well as less conventional probes such as heat conductivity (HC) and inelastic neutron scattering (INS). The emphasis in this review will be on spectroscopic data because of their more direct interpretative significance; however, these will be checked against thermodynamic/transport data whenever possible. With respect to the spectroscopic data, it will be important to differentiate between single-particle probes such as ARPES and STM, which directly measure the one-electron excitation energy Δ with respect to the chemical potential (on both side of E_F in STM), and two-particle probes

such as Raman and inelastic neutron scattering, which instead provide information on the particle-hole excitation energy 2Δ . Note that the values reported here are those for the ‘full gap’ 2Δ (associated with either E_{sc} or E_{pg}), while frequently only half the gap Δ is given for instance in the ARPES literature. In doing so one implicitly assumes that the chemical potential lies half-way between the lowest-energy single-electron removal and addition states; this might not necessarily be correct but appears to be supported by the direct comparison between ARPES and STM/Raman results. A more detailed discussion of the quantities measured by the different experiments and their interpretation will be provided in the following subsections. Here we would like to point out that studies of B_{2g} and B_{1g} Raman intensity [19, 52, 40], heat conductivity of nodal quasiparticles [70, 71], and neutron magnetic resonance energy Ω_r [42], do show remarkable agreement with superconducting or pseudogap energy scales as inferred by single-particle probes, or with the doping dependence of T_c itself. Thus they provide, in our opinion, an additional estimate of E_{sc} and

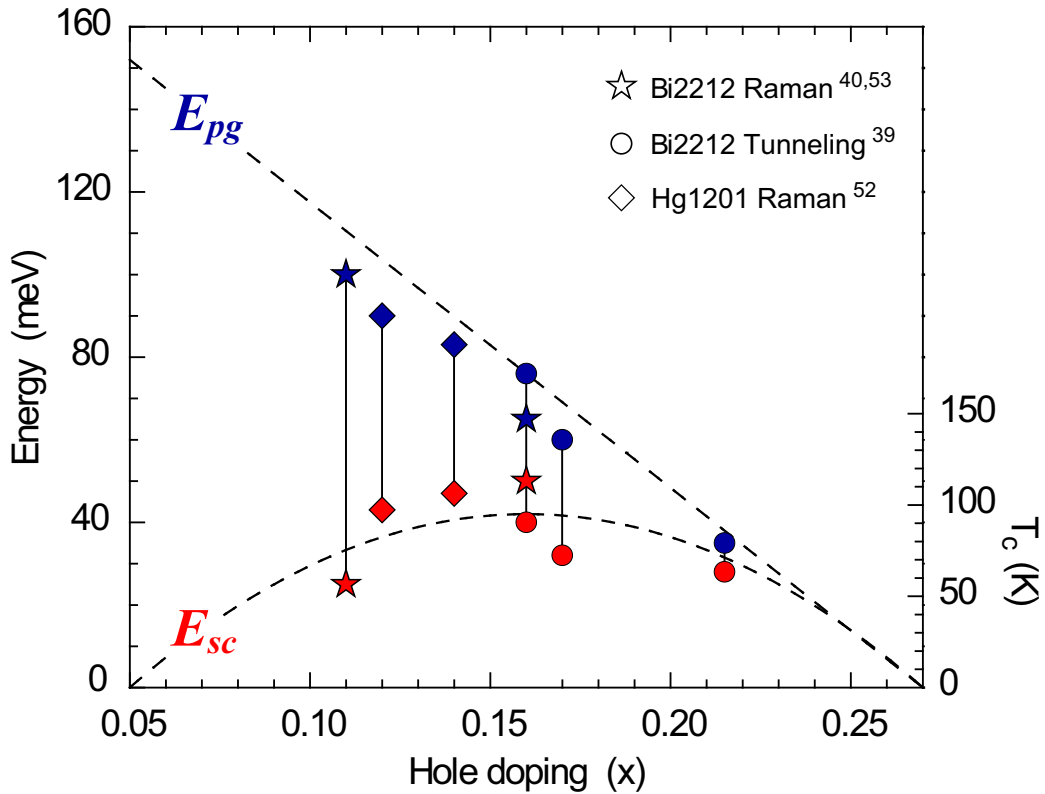


Figure 6.3: Pseudogap E_{pg} and superconducting E_{sc} energy scales (2Δ) as estimated, by a number of probes and for different compounds, in one single experiment on the very same sample. These data provide direct evidence of for the simultaneous presence of two energy scales, possibly two spectral gaps, coexisting in the superconducting state. The superconducting and pseudogap lines are defined as in Fig. 6.2.

E_{pg} .

As for the choice of the specific compounds to include in our analysis, we decided to focus on those HTSCs exhibiting a similar value of the maximum superconducting transition temperature T_c^{max} , as achieved at optimal doping, so that the data could be quantitatively compared without any rescaling. We have therefore selected $\text{Bi}_2\text{Sr}_2\text{CaCu}_2\text{O}_{8+\delta}$ (Bi2212), $\text{YBa}_2\text{Cu}_3\text{O}_{7-\delta}$ (Y123), $\text{Tl}_2\text{Ba}_2\text{CuO}_{6+\delta}$ (Tl2201), and $\text{HgBa}_2\text{CuO}_{4+\delta}$ (Hg1201), which have been extensively investigated and are all characterized by $T_c^{max} \sim 95$ K [73] (with particular emphasis on Bi2212, for which the most extensive set of single-particle spectroscopy data is available). It should also be noted that while Bi2212 and Y123 are ‘bilayer’ systems, i.e. their crystal structure contains as a key structural element sets of two adjacent CuO_2 layers, Tl2201 and Hg1201 are structurally simpler single CuO_2 -layer materials. Therefore, this choice of compounds ensures that our conclusions are generic to all HTSCs with a similar T_c , independent of the number of CuO_2 layers.

A compilation of experimental results for the magnitude of pseudogap ($E_{pg} = 2\Delta_{pg}$) and superconducting ($E_{sc} \sim 5k_B T_c$) energy scales, as a function of carrier doping x , is presented in Fig. 6.2 (only some representative datapoints are shown, such as not to overload the figure; similar compilations were obtained also by a number of other authors) [9, 5, 16, 13, 52, 57, 60, 42, 70, 43, 74, 75]. The data for these HTSCs with comparable $T_c^{max} \sim 95$ K fall on two universal curves: a straight line for the pseudogap energy $E_{pg} = 2\Delta_{pg}$, and a parabola for the superconducting energy scale $E_{sc} \sim 5k_B T_c$. The two curves converge to the same $x \sim 0.27$ critical point at the end of the superconducting dome, similar to the cartoon of Fig. 6.1a. In order to summarize the situation with respect to quantitative estimates of E_{pg} and E_{sc} , we have listed in Table 6.1 the values as determined by the different experimental techniques on optimally doped Bi2212 (with T_c ranging from 90 to 95 K). While one obtains from this compilation the average values of $E_{pg} \simeq 76$ meV and $E_{sc} \simeq 41$ meV at optimal doping, the numbers do scatter considerably. Note also that these numbers differ slightly from those given in relation to the parabolic and straight lines in Fig. 6.2 (e.g., $E_{sc}^{max} = 42$ meV) because the latter were inferred from a fitting of superconducting and pseudogap data over the whole doping range, while those in Table 6.1 were deduced from results for optimally doped Bi2212 only. It is also possible to plot the pseudogap E_{pg} and superconducting E_{sc} energy scales as estimated simultaneously in one single experiment on the very same sample. This is done in Fig. 6.3 for Raman, tunneling, and ARPES results from Bi2212 and Hg1201, which provide evidence for the presence of two energy scales, or possibly two spectral gaps as we will discuss in greater detail below, coexisting over the whole superconducting dome.

Angle-resolved photoemission

The most extensive investigation of excitation gaps in HTSCs has arguably been done by ARPES [9, 10, 26, 27, 35, 54, 55, 56, 57, 76, 77, 78, 79, 80, 58, 59, 60, 61, 62, 63, 34, 64, 65, 66]. This technique provides direct access to the one-electron removal spectrum of the many-body system; it allows, for instance in the case of a BCS superconductor [29], to measure the momentum dependence of the absolute value of the pairing amplitude 2Δ via the excitation gap Δ observed for single-electron removal energies, again assuming E_F to be located halfway in the gap [9, 10]. This is the same in some tunneling experiments such as STM,

which however do not provide direct momentum resolution but measure on both side of E_F [18]. The gap magnitude is usually inferred from the ARPES spectra from along the normal-state Fermi surface in the antinodal region, where the d -wave gap is largest; it is estimated from the shift to high-binding energy of the quasiparticle spectral weight relative to the Fermi energy. With this approach only one gap is observed below a temperature scale that smoothly evolves from the so-called pseudogap temperature T^* in the underdoped regime, to the superconducting T_c on the overdoped side. We identify this gap with the pseudogap energy scale $E_{pg} = 2\Delta_{pg}$. This is also in agreement with recent investigations of the near-nodal ARPES spectra from single and double layer Bi-cuprates [57, 76, 77], which further previous studies of the underdoped cuprates' Fermi arc phenomenology [78, 79, 80]. From the detailed momentum dependence of the excitation gap along the Fermi surface contour, and the different temperature trends observed in nodal and antinodal regions, these studies suggest the coexistence of two distinct spectral gap components over the whole superconducting dome: superconducting gap and pseudogap, dominating the response in the nodal and antinodal regions respectively, which would eventually collapse to one single energy scale in the very overdoped regime.

Tunneling

The HTSCs have been investigated by a wide variety of tunneling techniques [13, 18, 44, 45, 38, 39, 46, 37, 36, 47, 48, 49, 50, 51], such as SIN [38, 51], SIS [38, 39, 37], STM [18, 46, 36], intrinsic tunneling [47, 48, 49, 50] and Andreev reflection, which is also a tunneling experiment but involves two-particle rather than single-particle tunneling (in principle, very much like SIS) [13, 43, 72]. All of these techniques, exception made for intrinsic tunneling [81], are here represented either in the figures or table.

Similar to what was discussed for ARPES at the antinodes, there are many STM studies that report a pseudogap E_{pg} smoothly evolving into E_{sc} upon overdoping [18, 31]. In addition, a very recent temperature-dependent study of overdoped single-layer Bi-cuprate detected two coexisting, yet clearly distinct, energy scales in a single STM experiment [32]. In particular, while the pseudogap was clearly discernible in the differential conductance exhibiting the usual large spatial modulation, the evidence for a spatially-uniform superconducting gap was obtained by normalizing the low-temperature spectra by those just above $T_c \simeq 15$ K. These values have not been included in Fig. 6.2 and 6.3 because $T_c \ll 95$ K; however, this study arguably provides the most direct evidence for the coexistence of two distinct excitation gaps in the HTSCs.

One can regard Andreev reflection (pair creation in addition to a hole) as the inverse of a two-particle scattering experiment such as Raman or INS. A different view is also possible: SIN tunneling goes over to AR if the insulator layer gets thinner and thinner [13]; thus a SIN tunneling, as also STM, should give the same result as AR. However while SIN and STM measure the pseudogap, AR appears to be sensitive to the superconducting energy scale E_{sc} (Fig. 6.2). We can only conjecture that this has to do with the tunneling mechanisms being actually different.

SIS tunneling experiments [39] find $E_{pg}/E_{sc} \gtrsim 1$ for Bi2212 at all doping levels. There are however some open questions concerning the interpretation of the SIS experiments.

This technique, which exploits Josephson tunneling, measures pair spectra; the magnitude of E_{pg} can readily be obtained from the most pronounced features in the spectra [39]. The signal related to E_{sc} is seen as a ‘sideband’ on the E_{pg} features; it seems not obvious why, if the E_{sc} signal did originate from a state of paired electrons, it would not show up more explicitly.

Raman scattering

Light scattering measures a two-particle excitation spectrum providing direct insights on the total energy needed to break up a two-particle bound state or remove a pair from a condensate. Raman experiments can probe both superconducting and pseudogap energy scales, if one interprets the polarization dependent scattering intensity in terms of different momentum averages of the d -wave-like gap functions: one peaked at $(\pi,0)$ in B_{1g} geometry, and thus more sensitive to the larger E_{pg} which dominates this region of momentum space; the other at $(\pi/2,\pi/2)$ in B_{2g} geometry, and provides an estimate of the slope of the gap function about the nodes, $\frac{1}{\hbar} \frac{d\Delta}{dk}|_n$, which is more sensitive to the arguably steeper functional dependence of E_{sc} out of the nodes [19, 52, 40, 53]. One should note however that the signal is often riding on a high background, which might result in a considerable error and data scattering. At a more fundamental level, while the experiments in the antinodal geometry allow a straightforward determination of the gap magnitude E_{pg} , the nodal results need a numerical analysis involving a normalization of the Raman response function over the whole Brillouin zone, a procedure based on a low-energy B_{2g} sum rule (although also the B_{2g} peak position leads to similar conclusions) [52]. This is because a B_{2g} Raman experiment is somewhat sensitive also to the gap in the antinodal direction, where it picks up in particular the contribution from the larger pseudogap.

Inelastic neutron scattering

Inelastic neutron scattering experiments have detected the so-called $q = (\pi,\pi)$ resonant magnetic mode in all of the $T_c \simeq 95$ K HTSCs considered here [16]. This resonance is proposed by some to be a truly collective magnetic mode that, much in the same way as phonons mediate superconductivity in the conventional BCS superconductors, might constitute the bosonic excitation mediating superconductivity in the HTSCs. The total measured intensity, however, amounts to only a small portion of what is expected based on the sum rule for the magnetic scattering from a spin 1/2 system [16, 8, 24, 42, 68, 69]; this weakness of the magnetic response should be part of the considerations in the modeling of magnetic-resonance mediated high- T_c superconductivity. Alternatively, its detection below T_c might be a mere consequence of the onset of superconductivity and of the corresponding suppression of quasiparticle scattering. Independently of the precise interpretation, the INS data reproduced in Fig. 6.2 show that the magnetic resonance energy Ω_r tracks very closely, over the whole superconducting dome, the superconducting energy scale $E_{sc} \sim 5k_B T_c$ [similar behavior is observed, in the underdoped regime, also for the spin-gap at the incommensurate momentum transfer $(\pi,\pi \pm \delta)$][82]. Remarkable is also the correspondence between the energy of the magnetic resonance and that of the B_{2g} Raman peak. *Note that while the $q = (\pi,\pi)$ momentum transfer observed for the magnetic resonance in INS is a key ingredient*

of most proposed HTSC descriptions, Raman scattering is a $q = 0$ probe. It seems that understanding the connection between Raman and INS might reveal very important clues.

Heat conductivity

Heat conductivity data from Y123 and Tl2201 fall on to the pseudogap line. This is a somewhat puzzling result because they have been measured at very low temperatures, well into the superconducting state, and should in principle provide a measure of both gaps together if these were indeed coexisting below T_c . However, similar to the B_{2g} Raman scattering, these experiments are only sensitive to the slope of the gap function along the Fermi surface at the nodes, $\frac{1}{\hbar} \frac{d\Delta}{dk}|_n$; the gap itself is determined through an extrapolation procedure in which only one gap was assumed. The fact that the gap values, especially for Y123, come out on the high side of the pseudogap line may be an indication that an analysis with two coexisting gaps might be more appropriate.

Outlook & conclusion

The data in Fig. 6.2 and 6.3 demonstrate that there are two coexisting energy scales in the HTSCs: one associated with the superconducting T_c and the other, as inferred primarily from the antinodal region properties, with the pseudogap T^* . The next most critical step is that of addressing the subtle questions concerning the nature of these energy scales and the significance of the emerging two-gap phenomenology towards the development of a microscopic description of high- T_c superconductivity.

As for the pseudogap, which grows upon underdoping, it seems natural to seek a connection to the physics of the insulating parent compound. Indeed, it has been pointed out that this higher energy scale might smoothly evolve, upon underdoping, into the quasiparticle dispersion observed by ARPES in the undoped antiferromagnetic insulator [83, 84]. At zero doping the dispersion and quasiparticle weight in the single-hole spectral function as seen by ARPES can be very well explained in terms of a self-consistent Born approximation [85], as well as in the diagrammatic quantum Monte Carlo [86] solution to the so called t - t' - t'' - J model. In this model, as in the experiment [83, 84], the energy difference between the top of the valence band at $(\pi/2, \pi/2)$ and the antinodal region at $(\pi, 0)$ is a gap due to the quasiparticle dispersion of about 250 ± 30 meV. Note that this would be a single-particle gap Δ . For the direct comparison with the pseudogap data in Fig. 6.2, we would have to consider $2\Delta \sim 500$ meV; this however is much larger than the $x=0$ extrapolated pseudogap value of 186 meV found from our analysis across the phase diagram. Thus there seem to be an important disconnection between the finite doping pseudogap and the zero-doping quasiparticle dispersion.

The fact that the pseudogap measured in ARPES and SIN experiments is only half the size of the gap in SIS, STM, B_{1g} Raman, and heat conductivity measurements, points to a pairing gap. So, although the origin of the pseudogap at finite doping remains uncertain, we are of the opinion that it most likely reflects a pairing energy of some sort. To this end, the trend in Fig. 6.2 brings additional support to the picture discussed by many authors that the reduction in density of state at T^* is associated with the formation of electron

pairs, well above the onset of phase coherence taking place at T_c (see, e.g. Ref. [87] and [88]). The pseudogap energy $E_{pg} = 2\Delta_{pg}$ would then be the energy needed to break up a preformed pair. To conclusively address this point, it would be important to study very carefully the temperature-dependence of the $(\pi,0)$ response below T_c ; any further change with the onset of superconductivity, i.e. an increase of E_{pg} , would confirm the two-particle pairing picture, while a lack thereof would suggest a one-particle band structure effect as a more likely interpretation of the pseudogap.

The lower energy scale connected to the superconducting T_c (parabolic curve in Fig. 6.2, 6.3) has already been proposed by many authors to be associated with the condensation energy [87, 89, 90, 88], as well as with the magnetic resonance in INS [91]. One might think of it as the energy needed to take a pair of electrons out of the condensate; however, for a condensate of charged bosons, a description in terms of a collective excitation, such as a plasmon or roton, would be more appropriate [24]. The collective excitation energy would then be related to the superfluid density and in turn to T_c . In this sense, this excitation would truly be a two-particle process and should not be measurable by single-particle spectroscopies. Also, if the present interpretation is correct, this excitation would probe predominantly the charge-response of the system; however, there must be a coupling to the spin channel, so as to make this process neutron active (yet not as intense as predicted by the sum rule for pure spin-1/2 magnetic excitations, which is consistent with the small spectral weight observed by INS). As discussed, one aspect that needs to be addressed to validate these conjectures is the surprising correspondence between $q = 0$ and $q = (\pi, \pi)$ excitations, as probed by Raman and INS respectively.

We are thus led to the conclusion that the coexistence of two energy scales is essential for high- T_c superconductivity, with the pseudogap defining the pairing strength and the other, always smaller than the pseudogap, reflecting the superconducting condensation energy. This supports the proposals that the HTSCs can not be considered as classical BCS superconductors, but rather are smoothly evolving from the BEC into the BCS regime [92, 93, 94], as carrier doping is increased from the underdoped to the overdoped side of the phase diagram.

Acknowledgments

S.H. would like to thank the University of British Columbia for its hospitality. Helpful discussions with W.N. Hardy, D.G. Hawthorn, N.J.C. Ingle, and K.M. Shen are gratefully acknowledged. This work was supported by the Deutsche Forschungsgemeinschaft (SFB 277, TP B5), the Alfred P. Sloan Foundation (A.D.), CRC and CIFAR Quantum Materials Programs (A.D. and G.A.S), CFI, NSERC, and BCSI. M.A.H. has been supported by the Advanced Light Source (ALS) Doctoral Fellowship Program, Berkeley; ALS is supported by the Director, Office of Science, Office of Basic Energy Sciences, of the U.S. Department of Energy under Contract No. DE-AC02-05CH11231.

Bibliography

- [1] J.G. Bednorz and K.A. Müller. Possible high- T_c superconductivity in the Ba-La-Cu-O system. *Z. Phys. B*, 64:189–193, 1986.
- [2] W.E. Pickett. Electronic structure of the high-temperature oxide superconductors. *Rev. Mod. Phys.*, 61:433–512, 1989.
- [3] E. Dagotto. Correlated electrons in high-temperature superconductors. *Rev. Mod. Phys.*, 66:763–841, 1994.
- [4] M.A. Kastner, R.J. Birgeneau, G. Shirane, and Y. Endoh. Magnetic, transport, and optical properties of monolayer copper oxides. *Rev. Mod. Phys.*, 70:897–928, 1998.
- [5] T. Timusk and B.W. Statt. The pseudogap in high-temperature superconductors: an experimental survey. *Rep. Prog. Phys.*, 62:61–122, 1999.
- [6] J. Orenstein and A.J. Millis. Advances in the physics of high-temperature superconductivity. *Science*, 288:468–474, 2000.
- [7] C.C. Tsui and J.R. Kirtley. Pairing symmetry in cuprate superconductors. *Rev. Mod. Phys.*, 72:969–1016, 2000.
- [8] M.R. Norman and C. Pepin. The electronic nature of high temperature cuprate superconductors. *Rep. Prog. Phys.*, 66:1547–1610, 2003.
- [9] A. Damascelli, Z. Hussain, and Z.-X. Shen. Angle-resolved photoemission studies of the cuprate superconductors. *Rev. Mod. Phys.*, 75:473–541, 2003.
- [10] J.C. Campuzano, M.R. Norman, and M. Randeria. *Photoemission in the high T_c superconductors*, volume II, pages 167–265. Springer, Berlin, 2004.
- [11] Q. Chen, J. Stajic, S. Tan, and K. Levin. BCS-BEC crossover: from high temperature superconductors to ultracold superfluids. *Physics Reports*, 412:1–88, 2005.
- [12] M.R. Norman, D. Pines, and C. Kallin. The pseudogap: friend or foe of high T_c ? *Advances in Physics*, 54:715–733, 2005.
- [13] G. Deutscher. Andreev-Saint-James reflections: a probe of cuprate superconductors. *Rev. Mod. Phys.*, 77:109–135, 2005.
- [14] Special issue on high-temperature superconductors. *Nature Physics*, 2:133–210, 2006.
- [15] A.J. Millis. Gaps and our understanding. *Science*, 314:1888–1889, 2006.

-
- [16] M. Eschrig. The effect of collective spin-1 excitations on electronic spectra in high- T_c superconductors. *Advances in Physics*, 55:47–183, 2006.
- [17] A. Cho. High T_c : the mystery that defies solution. *Science*, 314:1072–1075, 2006.
- [18] Ø. Fischer, M. Kugler, I. Maggio-Aprile, C. Berthod, and C. Renner. Scanning tunneling spectroscopy of high-temperature superconductors. *Rev. Mod. Phys.*, 79:353–419, 2007.
- [19] T.P. Devereaux and R. Hackl. Inelastic light scattering from correlated electrons. *Rev. Mod. Phys.*, 79:175–233, 2007.
- [20] J.R. Schrieffer ed. *Treatise of high temperature superconductivity*. Springer, Berlin, 2007.
- [21] P.A. Lee, N. Nagaosa, and X.-G. Wen. Doping a Mott insulator: physics of high-temperature superconductivity. *Rev. Mod. Phys.*, 78:17–85, 2007.
- [22] D.N. Basov and T. Timusk. Electrodynamics of high- T_c superconductors. *Rev. Mod. Phys.*, 77:721–779, 2005.
- [23] A.J. Leggett. What do we know about high T_c ? *Nature Physics*, 2:134–136, 2006.
- [24] Y.J. Uemura. Twin spin/charge roton mode and superfluid density: primary determining factors of T_c in high- T_c superconductors observed by neutron, ARPES, and μ SR. *Physica B*, 374:1–8, 2006.
- [25] B. Batlogg, H.Y. Hwang, H. Takagi, R.J. Cava, H.L. Kao, and J. Kwo. Normal state phase diagram of $(\text{La,Sr})_2\text{CuO}_4$ from charge and spin dynamics. *Physica C*, 130:235–240, 1994.
- [26] A.G. Loeser, Z.-X. Shen, D.S. Dessau, D.S. Marshall, C.H. Park, P. Fournier, and A. Kapitulnik. Excitation gap in the normal state of underdoped $\text{Bi}_2\text{Sr}_2\text{CaCu}_2\text{O}_{8+\delta}$. *Science*, 273:325–329, 1996.
- [27] H. Ding, T. Yokoya, J.C. Campuzano, T. Takahashi, M. Randeria, M.R. Norman, T. Mochiku, K. Hadowaki, and J. Giapintzakis. Spectroscopic evidence for a pseudogap in the normal state of underdoped high- T_c superconductors. *Nature*, 382:51–54, 1996.
- [28] C.C. Tsuei and J.R. Kirtley. Pairing symmetry in cuprate superconductors. *Rev. Mod. Phys.*, 72:969–1016, 2000.
- [29] J. Bardeen, L.N. Cooper, and J.R. Schrieffer. Theory of superconductivity. *Phys. Rev.*, 108:1175–1204, 1957.
- [30] B. Goss Levi. New experiments fuel debate over the nature of high- T_c superconductors. *Physics Today*, 60(12):17–21, 2007.

-
- [31] K.K. Gomes, A.N. Pasupathy, A. Pushp, S. Ono, Y. Ando, and A. Yazdani. Visualizing pair formation on the atomic scale in the high- T_c superconductor $\text{Bi}_2\text{Sr}_2\text{CaCu}_2\text{O}_{8+y}$. *Nature*, 447:569–572, 2007.
- [32] M.C. Boyer, W.D. Wise, K. Chatterjee, M. Yi, K. Kondo, T. Takeuchi, H. Ikuta, and E.W. Hudson. Imaging the two gaps of the high-temperature superconductor $\text{Bi}_2\text{Sr}_2\text{CuO}_{6+x}$. *Nature Physics*, 3:802–806, 2007.
- [33] Y. Kohsaka, C. Taylor, K. Fujita, A. Schmidt, C. Lupien, T. Hanaguri, M. Azuma, M. Takano, H. Eisaki, H. Takagi, S. Uchida, and J.C. Davis. An intrinsic bond-centered electronic glass with unidirectional domains in underdoped cuprates. *Science*, 315:1380–1385, 2007.
- [34] A.V. Fedorov, T. Valla, P.D. Johnson, Q. Li, G.D. Gu, and N. Koshizuka. Temperature dependent photoemission studies of optimally doped $\text{Bi}_2\text{Sr}_2\text{CaCu}_2\text{O}_8$. *Phys. Rev. Lett.*, 82:2179–2182, 1999.
- [35] H. Ding, J.R. Engelbrecht, Z. Wang, J.C. Campuzano, S.-C. Wang, H.-B. Yang, R. Rogan, T. Takahashi, K. Kadowaki, and D.G. Hinks. Coherent quasiparticle weight and its connection to high- T_c superconductivity from angle-resolved photoemission. *Phys. Rev. Lett.*, 87:227001, 2001.
- [36] K. McElroy, D.-H. Lee, J.E. Hoffman, K.M. Lang, J. Lee, E.W. Hudson, H. Eisaki, S. Uchida, and J.C. Davis. Coincidence of checkerboard charge order and antinodal state decoherence in strongly underdoped superconducting $\text{Bi}_2\text{Sr}_2\text{CaCu}_2\text{O}_{8+\delta}$. *Phys. Rev. Lett.*, 94:197005, 2005.
- [37] N. Miyakawa, P. Guptasarma, J.F. Zasadzinski, D.G. Hinks, and K.E. Gray. Strong dependence of the superconducting gap on oxygen doping from tunneling measurements on $\text{Bi}_2\text{Sr}_2\text{CaCu}_2\text{O}_{8-\delta}$. *Phys. Rev. Lett.*, 80:157–160, 1998.
- [38] N. Miyakawa, J.F. Zasadzinski, L. Ozyuzer, P. Guptasarma, D.G. Hinks, C. Kendziora, and K.E. Gray. Predominantly superconducting origin of large energy gaps in underdoped $\text{Bi}_2\text{Sr}_2\text{CaCu}_2\text{O}_{8+\delta}$ from tunneling spectroscopy. *Phys. Rev. Lett.*, 83:1018–1021, 1999.
- [39] J.F. Zasadzinski, L. Ozyuzer, N. Miyakawa, K.E. Gray, D.G. Hinks, and C. Kendziora. Correlation of tunneling spectra in $\text{Bi}_2\text{Sr}_2\text{CaCu}_2\text{O}_{8+\delta}$ with the resonance spin excitation. *Phys. Rev. Lett.*, 87:067005, 2001.
- [40] F. Venturini, M. Opel, R. Hackl, H. Berger, L. Forro, and B. Revaz. Doping dependence of the electronic Raman spectra in cuprates. *J. Phys. Chem. Solids*, 63:2345–2348, 2002.
- [41] A.V. Puchkov, D.N. Basov, and T. Timusk. The pseudogap state in high- T_c superconductors: an infrared study. *J. Phys.: Condens. Mat.*, 8:10049–10082, 1996.

-
- [42] Y. Sidis, S. Pailhes, B. Keimer, P. Bourges, C. Ulrich, and L. P. Regnault. Magnetic resonant excitations in high- T_c superconductors. *J. Phys. Stat. Sol. B*, 241:1204–1210, 2004.
- [43] G. Deutscher. Coherence and single-particle excitations in the high-temperature superconductors. *Nature*, 397:410–412, 1999.
- [44] T. Shibauchi, L. Krusin-Elbaum, M. Li, M.P. Maley, and P.H. Kes. Closing the pseudogap by Zeeman splitting in $\text{Bi}_2\text{Sr}_2\text{CaCu}_2\text{O}_{8+y}$ at high magnetic fields. *Phys. Rev. Lett.*, 86:5763–5766, 2001.
- [45] L. Krusin-Elbaum, T. Shibauchi, G. Blatter, C.H. Mielke, M. Li, M.P. Maley, and P.H. Kes. Pseudogap state in overdoped $\text{Bi}_2\text{Sr}_2\text{CaCu}_2\text{O}_{8+y}$. *Physica C*, 387:169–174, 2003.
- [46] J. Lee, K. Fujita, K. McElroy, J.A. Slezak, M. Wang, Y. Aiura, H. Bando, M. Ishikado, T. Masui, J.-X. Zhu, A.V. Balatsky, H. Eisaki, S. Uchida, and J.C. Davis. Interplay of electron-lattice interactions and superconductivity in $\text{Bi}_2\text{Sr}_2\text{CaCu}_2\text{O}_{8+\delta}$. *Nature*, 442:546–550, 2006.
- [47] V.M. Krasnov, A. Yurgens, D. Winkler, P. Delsing, and T. Claeson. Evidence for coexistence of the superconducting gap and the pseudogap in Bi-2212 from intrinsic tunneling spectroscopy. *Phys. Rev. Lett.*, 84:5860–5863, 2000.
- [48] A. Yurgens, D. Winkler, T. Claeson, S. Ono, and Y. Ando. Intrinsic tunneling spectra of $\text{Bi}_2(\text{Sr}_{2-x}\text{La}_x)\text{CuO}_{6+\delta}$. *Phys. Rev. Lett.*, 90:147005, 2003.
- [49] M. Suzuki and T. Watanabe. Discriminating the superconducting gap from the pseudogap in $\text{Bi}_2\text{Sr}_2\text{CaCu}_2\text{O}_{8+\delta}$ by interlayer tunneling spectroscopy. *Phys. Rev. Lett.*, 85:4787–4790, 2000.
- [50] S.P. Zhao, X.B. Zhu, and Y.F. Wei. Intrinsic tunneling spectra of $\text{Bi}_2\text{Sr}_2\text{CaCu}_2\text{O}_{8+\delta}$ near optimal doping. *cond-mat/0703177*, 2007.
- [51] J.F. Zasadzinski, L. Ozyuzer, L. Coffey, K. Gray, D.G. Hinks, and C. Kendziora. Intrinsic tunneling spectra of $\text{Bi}_2(\text{Sr}_{2-x}\text{La}_x)\text{CuO}_{6+\delta}$. *Phys. Rev. Lett.*, 90:147005, 2003.
- [52] M. Le Tacon, A. Sacuto, A. Georges, G. Kotliar, Y. Gallais, D. Colson, and A. Forget. Two energy scales and two distinct quasiparticle dynamics in the superconducting state of underdoped cuprates. *Nature Physics*, 2:537–543, 2006.
- [53] S. Sugai, H. Suzuki, Y. Takayanagi, T. Hosokawa, and N. Hayamizu. Carrier-density-dependent momentum shift of the coherent peak and the LO phonon mode in p -type high- T_c superconductors. *Phys. Rev. B*, 68:184504, 2003.
- [54] J. Mesot, M.R. Norman, H. Ding, M. Randeria, J.C. Campuzano, A. Paramakanti, H.M. Fretwell, A. Kaminski, T. Takeuchi, T. Yokoya, T. Sato, T. Takahashi, T. Mochiku, and K. Kadowaki. Superconducting gap anisotropy and quasiparticle interactions: a doping dependent photoemission study. *Phys. Rev. Lett.*, 83:840–843, 1999.

-
- [55] T. Kondo, T. Takeuchi, A. Kaminski, S. Tsuda, and S. Shin. Evidence for two energy scales in the superconducting state of optimally doped $(\text{Bi,Pb})_2(\text{Sr,La})_2\text{CuO}_{6+\delta}$. *Phys. Rev. Lett.*, 98:267004, 2007.
- [56] T. Yoshida, X.J. Zhou, D.H. Lu, S. Komiya, Y. Ando, H. Eisaki, T. Kakeshita, S. Uchida, Z. Hussain, Z.-X. Shen, and A. Fujimori. Low-energy electronic structure of the high- T_c cuprates $\text{La}_{2-x}\text{Sr}_x\text{CuO}_4$ studied by angle-resolved photoemission spectroscopy. *J. Phys.: Condens. Matter*, 19:125209, 2007.
- [57] K. Tanaka, W.S. Lee, D.H. Lu, A. Fujimori, T. Fujii, Risdiana, I. Terasaki, D.J. Scalapino, T.P. Devereaux, Z. Hussain, and Z.-X. Shen. Distinct Fermi-momentum-dependent energy gaps in deeply underdoped Bi2212. *Science*, 314:1910–1913, 2006.
- [58] T. Valla, A.V. Fedorov, J. Lee, J.C. Davis, and G.D. Gu. The ground state of the pseudogap in cuprate superconductors. *Science*, 314:1914–1916, 2006.
- [59] M. Platé, J.D.F. Mottershead, I.S. Elfimov, D.C. Peets, R. Liang, D.A. Bonn, W.N. Hardy, S. Chiuzaian, M. Falub, M. Shi, L. Patthey, and A. Damascelli. Fermi Surface and Quasiparticle Excitations of overdoped Tl2201 by ARPES. *Phys. Rev. Lett.*, 95:077001, 2005.
- [60] D.C. Peets, J.D.F. Mottershead, B. Wu, I.S. Elfimov, R. Liang, W.N. Hardy, D.A. Bonn, M. Raudsepp, N.J.C. Ingle, and A. Damascelli. $\text{Tl}_2\text{Ba}_2\text{CuO}_{6+\delta}$ brings spectroscopic probes deep into the overdoped regime of the high- T_c cuprates. *New Journ. Physics*, 9:1–32, 2007.
- [61] A.D. Gromko, A.V. Fedorov, Y.-D. Chuang, J.D. Koralek, Y. Aiura, Y. Yamaguchi, K. Oka, Y. Ando, and D.S. Dessau. Mass-renormalized electronic excitations at $(\pi, 0)$ in the superconducting state of $\text{Bi}_2\text{Sr}_2\text{CaCu}_2\text{O}_{8+\delta}$. *Phys. Rev. B*, 68:174520, 2003.
- [62] T. Cuk, F. Baumberger, D.H. Lu, N. Ingle, X.J. Zhou, H. Eisaki, N. Kaneko, Z. Hussain, T.P. Devereaux, N. Nagaosa, and Z.-X. Shen. Coupling of the B_{1g} Phonon to the Antinodal Electronic States of $\text{Bi}_2\text{Sr}_2\text{CaCu}_2\text{O}_8$. *Phys. Rev. Lett.*, 93:117003, 2004.
- [63] J. Fink, A. Koitzsch, J. Geck, V. Zabolotnyy, M. Knupfer, B. Buchner, A. Chubukov, and H. Berger. Reevaluation of the coupling to a bosonic mode of the charge carriers in $(\text{Bi,Pb})_2\text{Sr}_2\text{CaCu}_2\text{O}_{8+\delta}$ at the antinodal point. *Phys. Rev. B*, 74:165102–12, 2006.
- [64] J.C. Campuzano, H. Ding, M.R. Norman, H.M. Fretwell, M. Randeria, A. Kaminski, J. Mesot, T. Takeuchi, T. Sato, T. Yokoya, T. Takahashi, T. Mochiku, K. Kadowaki, P. Guptasarma, D.G. Hinks, Z. Konstantinovic, Z.Z. Li, and H. Raffy. Electronic spectra and their relation to the (π, π) collective mode in high- T_c superconductors. *Phys. Rev. Lett.*, 83:3709–3712, 1999.
- [65] P.D. Johnson, T. Valla, Z. Fedorov, A.V. and Yusof, B.O. Wells, Q. Li, A.R. Moodenbaugh, G.D. Gu, N. Koshizuka, C. Kendziora, S. Jian, and D.G. Hinks. Doping and temperature dependence of the mass enhancement observed in the cuprate $\text{Bi}_2\text{Sr}_2\text{CaCu}_2\text{O}_{8+\delta}$. *Phys. Rev. Lett.*, 87:177007, 2001.

-
- [66] A.A. Kordyuk and S.V. Bosisenko. ARPES on high-temperature superconductors: simplicity vs. complexity. *Low Temp. Phys.*, 32:298–304, 2006.
- [67] S.V. Dordevic, C.C. Homes, J.J. Tu, T. Valla, M. Strongin, P.D. Johnson, G.D. Gu, and D.N. Basov. Extracting the electron- boson spectral function $\alpha^2F(\omega)$ from infrared and photoemission data using inverse theory. *Phys. Rev. B*, 71:104529, 2005.
- [68] P. Dai, H.A. Mook, R.D. Hunt, and F. Dogan. Evolution of the resonance and incommensurate spin fluctuations in superconducting $\text{YBa}_2\text{Cu}_3\text{O}_{6+x}$. *Phys. Rev. B*, 63:054525, 2001.
- [69] H. He, H. He, P. Bourges, Y. Sidis, C. Ulrich, L.P. Regnault, S. Pailhs, N.S. Berziyarova, N.N. Kolesnikov, and B. Keimer. Magnetic resonant mode in the single-layer high-temperature superconductor $\text{Tl}_2\text{Ba}_2\text{CuO}_{6+\delta}$. *Science*, 295:1045–1047, 2002.
- [70] M. Sutherland, D.G. Hawthorn, R.W. Hill, F. Ronning, S. Wakimoto, H. Zhang, C. Proust, E. Boaknin, C. Lupien, L. Taillefer, R. Liang, D.A. Bonn, W.N. Hardy, R. Gagnon, N.E. Hussey, T. Kimura, M. Nohara, and H. Takagi. Thermal conductivity across the phase diagram of cuprates: Low-energy quasiparticles and doping dependence of the superconducting gap. *Phys. Rev. B*, 67:174520, 2003.
- [71] D.G. Hawthorn, S.Y. Li, M. Sutherland, E. Boaknin, R.W. Hill, C. Proust, F. Ronning, M.A. Tanatar, J. Paglione, L. Taillefer, D. Peets, R. Liang, D.A. Bonn, W.N. Hardy, and N.N. Kolesnikov. Doping dependence of the superconducting gap in $\text{Tl}_2\text{Ba}_2\text{CuO}_{6+\delta}$ from heat transport. *Phys. Rev. B*, 75:104518, 2007.
- [72] G. Deutscher. Superconducting gap and pseudogap. *Low Temp. Phys.*, 397:410–412, 1999.
- [73] H. Eisaki, N. Kaneko, D.L. Feng, A. Damascelli, P.K. Mang, K.M. Shen, Z.-X. Shen, and M. Geven. Effect of chemical inhomogeneity in bismuth-based copper oxide superconductors. *Phys. Rev. B*, 69:064512, 2004.
- [74] C. Panagopoulos and T. Xiang. Relationship between the superconducting energy gap and the critical temperature in high- T_c superconductors. *Phys. Rev. Lett.*, 81:2336, 1998.
- [75] B. Valenzuela and E. Bascones. Phenomenological description of the two energy scales in underdoped cuprate superconductors. *Phys. Rev. Lett.*, 98:227002, 2007.
- [76] T. Kondo, T. Takeuchi, A. Kaminski, S. Tsuda, and S. Shin. Evidence for two energy scales in the superconducting state of optimally doped $(\text{Bi,Pb})_2(\text{Sr,Lu})_2\text{CuO}_{6+\delta}$. *Phys. Rev. Lett.*, 98:267004, 2007.
- [77] W.S. Lee, I.M. Vishik, K. Tanaka, D.H. Lu, T. Sasagawa, N. Nagaosa, T.P. Devereaux, Z. Hussain, and Z.-X. Shen. Abrupt onset of a second energy gap at the superconducting transition of underdoped $\text{Bi}2212$. *Nature*, 450:81–84, 2007.

-
- [78] M.R. Norman, H. Ding, M. Randeria, J.C. Campuzano, T. Yokoya, T. Takeuchi, T. Takahashi, T. Mochiku, K. Kadowaki, P. Guptasarma, and D.G. Hinks. Destruction of the Fermi surface in underdoped high- T_c superconductors. *Nature*, 392:157–160, 1998.
- [79] A. Kanigel, M.R. Norman, M. Randeria, U. Chatterjee, S. Souma, A. Kaminski, H.M. Fretwell, S. Rosenkranz, M. Shi, T. Sato, T. Takahashi, Z.Z. Li, H. Raffy, K. Kadowaki, D. Hinks, L. Ozyuzer, and J.C. Campuzano. Evolution of the pseudogap from Fermi arcs to the nodal liquid. *Nature Physics*, 2:447–451, 2006.
- [80] K.M. Shen, F. Ronning, D.H. Lu, F. Baumberger, N.J.C. Ingle, W.S. Lee, W. Meevasana, Y. Kohsaka, M. Azuma, M. Takano, H. Takagi, and Z.-X. Shen. Nodal quasiparticles and antinodal charge ordering in $\text{Ca}_{2-x}\text{Na}_x\text{CuO}_2\text{Cl}_2$. *Science*, 307:901–904, 2005.
- [81] The most convincing tunneling results showing two coexisting gaps were actually obtained by intrinsic tunneling [47, 48, 49, 50], in particular from $\text{Bi}_2\text{Sr}_2\text{CuO}_{6+\delta}$ (Bi2201) [48]. However, because this technique suffers from systematic problems [50], and one would anyway have to scale the Bi2201 data because of the lower value of T_c and in turn gap energy scales, these results were not included in Fig. 6.2 or 6.3. Since intrinsic tunneling is in principle a clean SIS experiment which measures pair energies through Josephson tunneling, a refinement of the technique might provide an accurate estimate of both superconducting and pseudogap simultaneously, and is thus highly desirable.
- [82] J. Chang, A.P. Schnyder, R. Gilardi, H.M. Rnnow, S. Pailhes, N.B. Christensen, Ch. Niedermayer, D.F. McMorrow, A. Hiess, A. Stunault, B. Enderle, M. Lake, O. Sobolev, N. Momono, M. Oda, M. Ido, C. Mudry, and J. Mesot. Magnetic-field-induced spin excitations and renormalized spin gap of the underdoped $\text{La}_{1.895}\text{Sr}_{0.105}\text{CuO}_4$ superconductor. *Phys. Rev. Lett.*, 98:077004, 2007.
- [83] F. Ronning, C. Kim, D.L. Feng, D.S. Marshall, A.G. Loeser, L. L. Miller, J. N. Eckstein, L. Bozovic, and Z.-X. Shen. Photoemission evidence for a remnant Fermi surface and a d -wave-like dispersion in insulating $\text{Ca}_2\text{CuO}_2\text{Cl}_2$. *Science*, 282:2067–2072, 1998.
- [84] F. Ronning, C. Kim, K.M. Shen, N.P. Armitage, A. Damascelli, D.H. Lu, D.L. Feng, Z.-X. Shen, L.L. Miller, Y.-J. Kim, F. Chou, and I. Terasaki. Universality of the electronic structure from a half-filled CuO_2 Plane. *Phys. Rev. B*, 67:035113, 2003.
- [85] O.P. Sushkov, G.A. Sawatzky, R. Eder, and H. Eskes. Hole photoproduction in insulating copper oxide. *Phys. Rev. B*, 56:11769, 1997.
- [86] N.V. Prokof'ev and B.V. Svistunov. Polaron problem by diagrammatic quantum monte carlo. *Phys. Rev. Lett.*, 81:2514–2517, 1998.
- [87] G. Kotliar. Resonating valence bonds and d -wave superconductivity. *Phys. Rev. B*, 37:3664–3666, 1988.

-
- [88] V.J. Emery and S.A. Kivelson. Importance of phase fluctuations in superconductors with small superfluid density. *Nature*, 374:434–437, 1995.
- [89] G. Kotliar and J. Liu. Superexchange mechanism and d -wave superconductivity. *Phys. Rev. B*, 38:5142–5145, 1988.
- [90] Y.J. Uemura, G.M. Luke, B.J. Sternlieb, J.H. Brewer, J.F. Carolan, W.N. Hardy, R. Kadono, J.R. Kempton, R.F. Kiefl, S.R. Kreitzman, P. Mulhern, T.M. Riseman, L. Williams, B.X. Yang, S. Uchida, H. Takagi, J. Gopalakrishnan, A.W. Sleight, M.A. Subramanian, C.L. Chien, M.Z. Cieplak, G. Xiao, V.Y. Lee, B.W. Statt, C.E. Stronach, W.J. Kossler, and X.H. Yu. Universal correlations between T_c and n_s/m^* (carrier density over effective mass) in high- T_c cuprate superconductors. *Phys. Rev. Lett.*, 62:2317–2320, 1989.
- [91] S.-C. Zhang. A unified theory based on SO(5) symmetry of superconductivity and antiferromagnetism. *Science*, 275:1089–1096, 1997.
- [92] A.J. Leggett. *Quantum liquids*. Oxford, 2006.
- [93] A.J. Leggett. *Modern trends in the theory of condensed matter*, pages 13–27. Springer Verlag, 1980.
- [94] P. Nozieres and S. Schmitt-Rink. Bose condensation in an attractive fermion gas: from weak to strong coupling superconductivity. *J. Low. Temp. Phys.*, 59:195–211, 1985.

Chapter 7

Conclusions

In this chapter, additional data are presented that were not included in the papers presented in the previous chapters. These data/ideas are intended to provide further explanation, support and fresh perspective to the conclusions reached in the previous chapters. The chapter ends with open questions, speculations and a brief reassessment of the projects.

7.1 Signature of long range antiferromagnetism from XAS

As mentioned in Chapter 1, X-ray linear dichroism (XLD) has proved to be one of the most decisive tool to probe temperature and field dependence of magnetic moments in antiferromagnets where other standard techniques to probe ferromagnetic materials such as X-ray circular dichroism (XCD) fails. This is because XCD is sensitive to the expectation value of the local magnetic moment $\langle \mathbf{M} \rangle$ while XLD is proportional to $\langle \mathbf{M}^2 \rangle$. In addition to be sensitive to long range magnetic order, only recently XLD has been proved to be sensitive to the orientation of magnetic moments [1, 2] and has been established as a direct measure of nearest-neighbor spin-spin correlation function. However, this powerful feature/aspect of XLD has not been explored in case of itinerant systems with dilute magnetic impurities/dopants where the magnetic impurities being far away from each other might be interacting via the non-magnetic/itinerant electrons surrounding them. Signature of such an effect may establish XLD as a technique sensitive to not only nearest-neighbor spin-spin correlation function but also to next-nearest-neighbor spin-spin correlation and so on.

We have shown in Chapter 3 that Mn doped $\text{Sr}_3\text{Ru}_2\text{O}_7$ goes through a metal-insulator transition to an antiferromagnetic insulating phase at low temperature. Here we want to investigate the signature of this long range order/transition in the x-ray absorption spectra (XAS) that is known to be a local spectroscopic probe. Fig. 7.1(a,c) present temperature-dependent XAS data, limited for simplicity to the L_2 Mn-edge, from 5 and 20% Mn-doped samples. A pronounced evolution can be observed for the 5% sample, with peaks A and B, respectively, gaining and losing intensity across the phase transition (no dependence was detected between 295 and 80K). The 20% sample shows a much weaker and actually reversed evolution for A and B peaks. Remarkably, this temperature dependence is captured by multiplet calculations with the inclusion of a 1meV exchange (i.e., antiferromagnetic) field. At room temperature [red lines in Fig. 7.1(b,d)], no difference is observed between 5 and 20% Mn, and the lineshape is uniquely determined by the orbital population (in this case, because $T \gg H^{ex} = 1\text{meV} \simeq 10\text{K}$, we are effectively in a non-magnetic ground state). Performing the calculations at lower temperatures, contributions from antiferromagnetic ordering are detected in Fig. 7.1(b,d). The opposite temperature trends observed for the two dopings is reproduced by the inclusion of exchange fields with different orientations

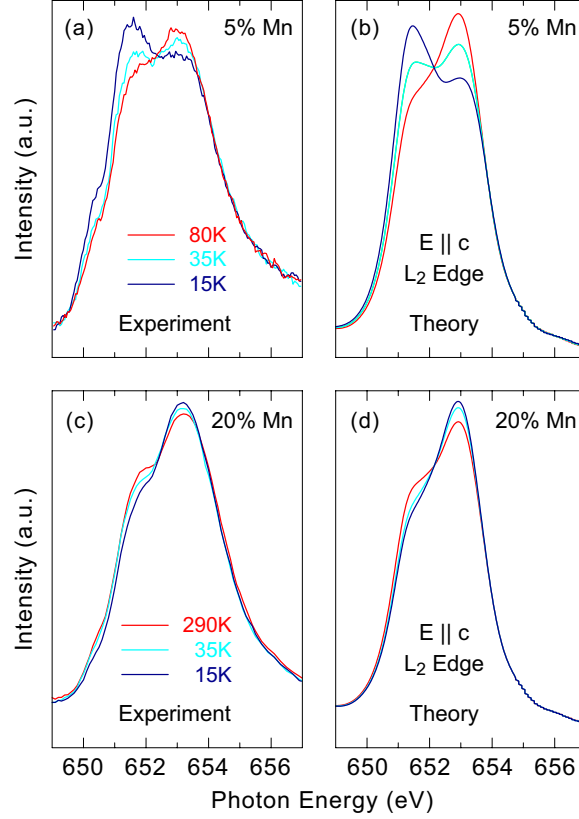


Figure 7.1: (a,c) Temperature dependent Mn L_2 -edge XAS spectra measured on 5 and 20% Mn-doped samples with $\mathbf{E} \parallel \mathbf{c}$. (b,d) Theoretical L_2 -edge spectra calculated with the inclusion of a 1meV antiferromagnetic exchange field: (b) H^{ex} 30° away from c -axis, $T_{Neel} = 50\text{K}$; (d) $H^{ex} \parallel c$ -axis, $T_{Neel} = 100\text{K}$. While no field dependence is observed in the 300K non-magnetic state ($T \gg H^{ex} = 1\text{meV} \simeq 10\text{K}$), a clear effect is seen once the ground state is antiferromagnetic. This demonstrates the extreme sensitivity of XAS and linear dichroism to the onset of antiferromagnetic ordering, that Mn impurities do induce antiferromagnetism in $\text{Sr}_3\text{Ru}_2\text{O}_7$, and that the field orientation varies progressively from out-of-plane (b) to in-plane (d) upon increasing Mn-doping from 5 to 20%.

with respect to the c -axis (see caption). This demonstrates the extreme sensitivity of XAS and X-ray LD to the onset of antiferromagnetic ordering and, more specifically, that Mn impurities do induce antiferromagnetism in $\text{Sr}_3\text{Ru}_2\text{O}_7$, with an exchange field orientation that varies progressively from out-of-plane to in-plane upon increasing Mn-content from 5 to 20%.

A summary of the complete temperature-dependent XAS study of 5, 10, and 20% doped $\text{Sr}_3(\text{Ru}_{1-x}\text{Mn}_x)_2\text{O}_7$ is presented in Fig. 7.2, where the relative intensity change of A and B peaks [$L_2^R(T)/L_2^R(15)$, see caption for definition] is compared to the electrical resistivity

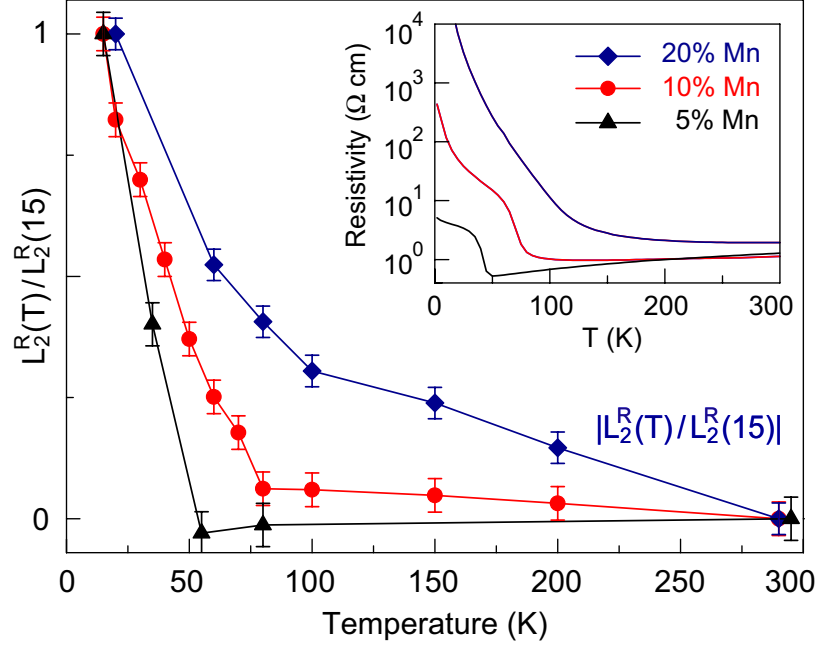


Figure 7.2: Normalized L_2 -edge peak-height ratio, defined as $L_2^R(T)/L_2^R(15)$, where $L_2^R(T) = [\frac{I_A - I_B}{I_A + I_B}(T) - \frac{I_A - I_B}{I_A + I_B}(295)]$ and $I_{A,B}$ is the intensity of peak A, B in Fig. 7.1, plotted vs. temperature for 5, 10, and 20% Mn-doped $\text{Sr}_3\text{Ru}_2\text{O}_7$. For 20% Mn, the modulus of the data is plotted. The inset presents temperature dependent electrical resistivity data (in logarithmic scale), for the same samples [3]. A sharp increase is observed in both resistivity and X-ray linear dichroism experiments for 5 and 10% Mn, and only a continuous evolution for 20% Mn, indicating that the metal-insulator transition is driven by the onset of antiferromagnetic ordering.

data of Mathieu et al. [3]. Clearly, a sharp transition is observed in the X-ray linear dichroism data for 5 and 10% Mn, at 50 and 80K respectively, while only a continuous evolution for 20% Mn. Together with the analysis presented in Fig. 7.1 connecting the temperature dependence of the XAS-LD signal to the onset of antiferromagnetic ordering. It is remarkable that temperature dependent XAS data can quantitatively track the trend provided by transport data that probe the long range electronic properties of the system.

7.2 Puzzle of the energy gap

Having established the presence of emerging antiferromagnetic correlations around the Mn impurities at low temperature, one might wonder whether the jump observed in the L_2 edge reflects an increase in electron scattering, perhaps due to the formation of magnetoelastic polarons, rather than a true full-blown metal-insulator transition. Indeed in Chapter 3

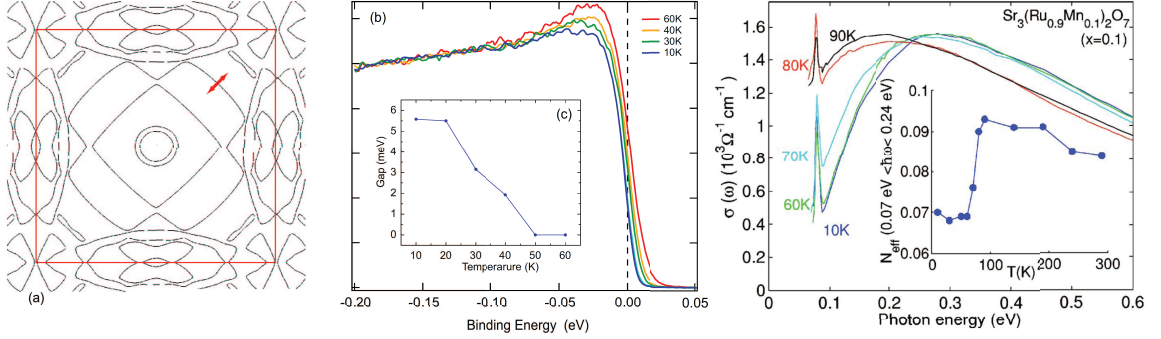


Figure 7.3: (a) Band structure calculations performed for the distorted structure of the pure compound (after Ref. [5]). (b) Temperature dependent ARPES spectra measured on the 5% Mn-doped sample, in correspondence of the Fermi surface sheets originating from the xy band of the undistorted structure. (c) Across the metal-insulator antiferromagnetic transition a leading-edge gap opens, as seen also on other portions of the Fermi surface.

we have shown that the system goes to an unconventional antiferromagnetic phase below the metal-insulator transition. However, a direct look at the energy gap as a function of momentum (energy-momentum resolved map of the Fermi surface) is needed to investigate the origin of the $\mathbf{q} = (\frac{1}{4}, \frac{1}{4}, 0)$ modulated order. With these specific goals in mind, we have performed angle-resolved photoemission spectroscopy (ARPES) experiments on 5 and 10% Mn doped samples. This technique allows the detection of a gap opening along the normal state Fermi surface of a metal, even in the case of momentum-dependent gaps as the d -wave superconducting gap of the high-temperature copper oxides [4]. Fig. 7.3 presents temperature-dependent ARPES data measured on the 5% Mn-doped sample at different temperatures. In correspondence of the xy band derived Fermi surface crossing indicated in the theoretical Fermi surface plot of Fig. 7.3(a) [5], the leading edge of the spectra pulls back with respect to the chemical potential, upon reducing the temperature below $T_c = 50\text{K}$. This allow us to conclude that, across the antiferromagnetic transition, a true excitation gap opens up on the Fermi surface. A similar behavior was also observed at other locations in the Brillouin zone. Thus, the Mn-impurities produce a global effect on the physical properties of the host system.

However, there seems to be a disagreement between the magnitude of the gap obtained from ARPES and optical spectroscopy [3]. Mathieu *et al.* estimates the gap to be ~ 200 meV that is about two orders of magnitude larger than ARPES estimation! This discrepancy can be due to several reasons: the Fermi surface gap can be strongly momentum dependent and we happen to measure at a place where it is particularly small. Although we did not observe strong momentum dependence of the gap, a through investigation is needed. On top of that, ARPES is a surface sensitive technique and hence the gap we are measuring may not reflect the gap in the bulk of the material. Also, the optical spectroscopy data is not particularly unambiguous in the sense that peaks are very broad and that makes it

hard to extract a precise number for the energy shift.

7.3 Random impurities as a probe of spatially inhomogeneous order

As mentioned in Chapter 3, RSXS is an element sensitive technique and at the Mn L edge, the resonance enhanced scattering signal is only coming from the dilute Mn impurities in the sample. This means our model is based on the fact that the spins of the randomly distributed Mn atoms are correlated and can scatter coherently to reflect the underlying order of the Ru-O matrix. We simulated that even a very low concentration of Mn ($\sim 1\%$) is enough to give rise to the superlattice peak. For a single domain situation, this can also be shown analytically in the following manner:

$$\begin{aligned}
 F^{Mn}(\mathbf{Q}) &= \sum_{\mathbf{r}_j} f_j(\mathbf{Q}) \sum_{\mathbf{R}_n} e^{i\mathbf{Q}\cdot(\mathbf{r}_j+\mathbf{R}_n)} \times \eta(\mathbf{R}_n) \\
 &= \sum_{\mathbf{R}_n} \eta \sum_{\mathbf{r}_j} f_j(\mathbf{Q}) e^{i\mathbf{Q}\cdot(\mathbf{r}_j)} \\
 &= \bar{\eta} \sum_{\mathbf{r}_j} f_j(\mathbf{Q}) e^{i\mathbf{Q}\cdot(\mathbf{r}_j)} \tag{7.1}
 \end{aligned}$$

where $\eta(\mathbf{R}_n)$ is a random number that is nonzero only at the Mn impurity sites, \mathbf{r}_j denote the positions of the atoms in the unit cell and \mathbf{R}_n denote the positions of the unit cells. It is important to note that the average number of Mn atoms comes only as a factor in amplitude and hence the total intensity should scale quadratically with the percentage of Mn impurities present in the sample. The model also provides a picture of the doping evolution of the order, described in Chapter 3, and shows that order is visible on the Mn edge even if the Mn atoms are distributed randomly in domains.

Interestingly, the underlying spin order is extremely difficult to observe on the Ru L edge although Ru occupies 95% of the lattice sites, i.e. scattering signal from 5% Mn is much stronger than that of 95% of the Ru! This happens partly due to much stronger magnetic moment and scattering cross section of Mn compared to Ru. Also, Mn impurities act as seed for the magnetic islands and the spin order in the RuO environment is more susceptible to disorder due to overlapping regions containing more than two islands (leading to frustration) etc. Overall, this shows the promise of using a “suitable” dilute impurity (with high scattering cross-section, magnetic-moment, orbital polarizability etc) as a “magnifying glass” to induce and detect weak spin/charge/orbital order in the host system that is difficult to access via the majority lattice population. The beauty of this approach is that we can scatter from the impurity and host atoms selectively and hence, the approach is especially suitable for spatially inhomogeneous orders, e.g. vortices, spirals, density wave type of orders etc. For instance, if we have a spiral spin order in Ru with Mn spins are along the c -axis, we will see different azimuthal angle dependence in Ru and Mn edge.

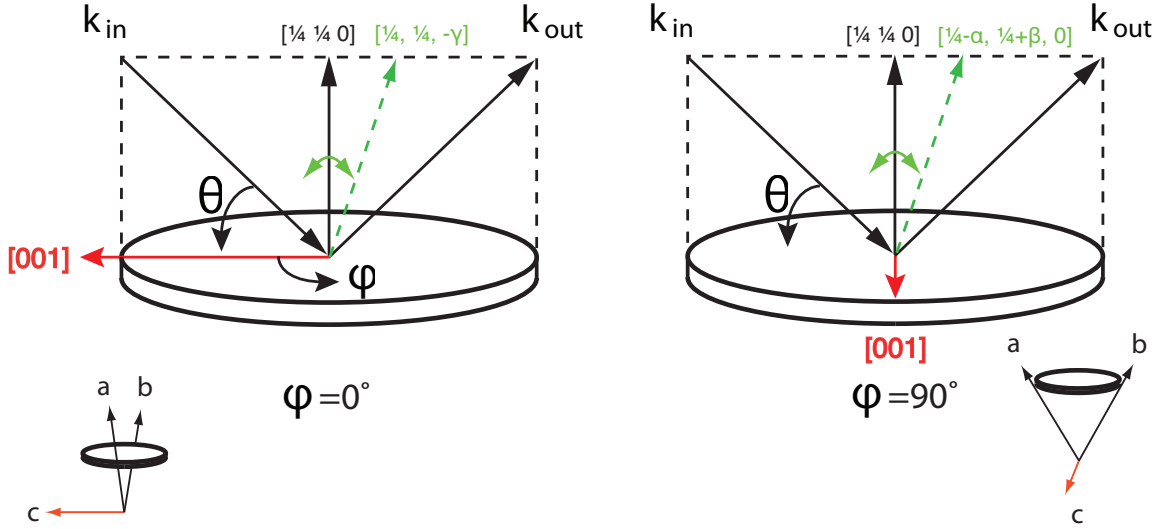


Figure 7.4: Interpretation of “ θ -scans” in two different azimuthal angle geometry of the sample with respect to the scattering plane. At $\phi = 0^\circ$ and 90° geometry one probes the order along the c -axis and ab -plane respectively.

7.4 Scattering momentum scans

It is important to distinguish between the two different types of momentum scans presented Chapter 3 since they provide us different kinds of information. The scans presented in Fig. 3.1 (b) are commonly known as “ θ scans” and that in Fig. 3.1(c) and 3.3(a) are known as “ $\theta - 2\theta$ scans”. Chapter 3 utilizes a combination of these scans in various geometries to probe the dimensionality of the magnetic order in Mn doped $\text{Sr}_3\text{Ru}_2\text{O}_7$. Fig. 7.4 shows the geometry of the “ θ scans” for two different azimuthal (ϕ) angles. As it can be seen in the figure, we are not doing the $(h, \frac{1}{4}, 0)$, or $(\frac{1}{4}, k, 0)$ scans, instead, for $\phi = 0^\circ$ (close to $\phi = -5^\circ$ shown in Fig. 3.1(b)), we are doing $(\frac{1}{4}, \frac{1}{4}, l)$ scans and thereby probing c -axis component of the order. On the other hand, for $\phi = 90^\circ$, we are doing $(h, -k, 0)$ scans probing the in-plane (ab) component of the order. Therefore, the FWHM of the scans is directly related to the out of plane and in-plane correlation length, respectively. From, Fig. 3.1(b) we can say that correlation length along the c -axis is much weaker compared to that of the ab -plane. Instead, the scans shown in Fig. 3.2(a) are longitudinal (“ $\theta - 2\theta$ ”) scans taken at the same azimuthal position ($\phi = 90^\circ$), which probe the correlation length in the ab -plane. Therefore, the observed difference in the FWHM cannot result from a correlation difference along the c -axis. On the other hand, “ $\theta - 2\theta$ ” scans always probe momentum along the surface normal which is $[110]$ in this case, regardless of the azimuthal angle.

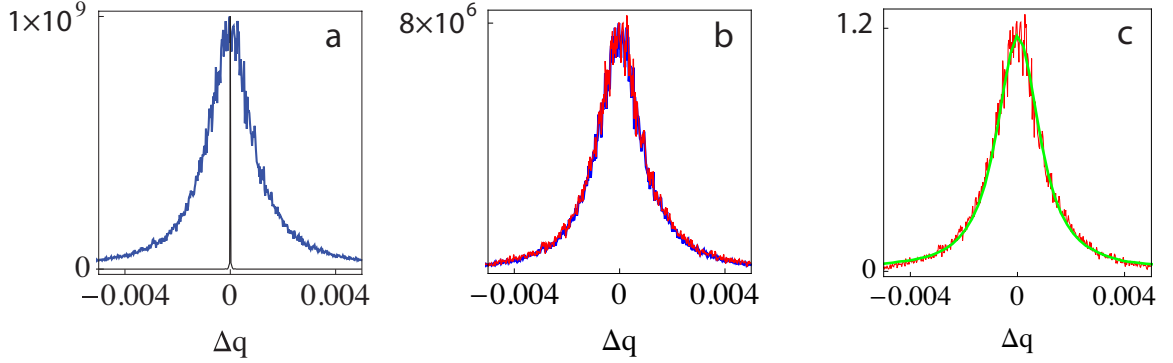


Figure 7.5: Comparison of the momentum scan (“ $\theta - 2\theta$ ”) widths resulting from scattered intensities from: (a) 100% sites without domains with the same system having average domain size of 320 lattice spacing. (b) 100% sites from the system with domains with 10% randomly selected sites from the same system (normalized). (c) 10% random sites with measured ($\frac{1}{4} + \Delta q, \frac{1}{4} + \Delta q, 0$) scan on 10% Mn doped $\text{Sr}_3\text{Ru}_2\text{O}_7$.

7.5 Solitons in a 1D spin chain: effect on momentum scan width

In this section, we would like to investigate the effect of domain wall population (solitons or kinks in the phase [7, 8]) in the width of scattering momentum scans. Fig. 7.5 (a, b, c) compare the momentum scan (“ $\theta - 2\theta$ ” scan) width simulations from a 1-dimensional spin chain system; as we go from a chain with 100% sites occupied by Mn impurities to a situation where only 10% sites occupied in a system of spin chains with domains. The calculations were done with spin chains consisting of 64000 sites and, while the average domain size has been fixed to 320 lattice spacing, domain positions were randomly generated and each momentum scan is an average over 200 independent domain selection iterations. One dimensional model has been chosen to reduce calculation time and due to the fact that we only need width and intensity information, i.e. cross-sectional information of the diffraction peaks are enough. In each panel the momentum scans are normalized to the peak intensity to compare the widths. Fig 7.5(a) compares ($\frac{1}{4} + \Delta q, \frac{1}{4} + \Delta q, 0$) momentum scan intensity profiles from lattices with 100% of the sites contributing to the signal, one without domains (Black) and the other one with domains of the average size of 320 lattice spacing (blue). The huge increase in width in the intensity profile generated from the lattice with domains is clearly noticeable. We can now randomly select 10% sites from the system with domains and generate intensity profile to find out if the peak is still observable. Fig 7.5(b) compares momentum scans generated from the system with domains with 100% lattice sites contributing (Blue) to that of the same system with only 10% randomly selected sites contributing (red) to the signal. Indeed, scattering signal from the system with only 10% sites randomly distributed in domains generates clear superlattice peak. Fig 7.5(c)

compares this simulated intensity profile with the experimental momentum scan on 10% doped sample (purple). The same procedure has been followed for the 5% doped case (not shown here) and the experimental momentum scan fits very well with the simulated scan with average domain size of 85 lattice spacing and the summary is that scattered signal from dilute impurities randomly distributed in domains can indeed reflect the underlying electronic order.

7.6 Summary, significance and possibilities: Ruthenates

In Chapter 2 we have shown a mechanism to control the localized impurity (Mn) valence-orbital symmetry via the dimensionality of the delocalized host (Ru-O). Layered material $\text{Sr}_3\text{Ru}_2\text{O}_7$ has building blocks of Ru-O perovskite structures where each Ru atom is surrounded by a cage made of 6 Oxygens that has more room along the out-of-plane vertical direction (c -axis) than the in-plane (ab). If we replace a very small fraction (5% or more) of Ru atoms with Mn impurities, Mn takes the unusual valency of 3+ and thereby keeps an extra valence electron to itself. Since the surrounding O cage has more room along the out-of-plane direction, the extra Mn valence electron must occupy the orbital with the out-of-plane symmetry so that it can stay away from the tightly placed in-plane O electrons. We found that due to very two dimensional and delocalized nature of the host Ru-O matrix this Mn valence electron is forced to make the unlikely choice of occupying the orbital of in-place symmetry, as if very 2D environment flattens out the Mn that would normally try to stick out from the plane; just like a rubber blob on the surface of a balloon gets flattened as the balloon is inflated. This dominance of the delocalized 2D environment over localized $3d$ impurities can be exploited further more by putting even more localized impurities like $4f$ valence shell atoms, a combination that is very likely to bring designer materials with exotic dimensional interplay.

In Chapter 3 we showed for the first time - both experimentally and theoretically - that one can measure diffraction arising from randomly-distributed dilute impurities; and this even in the presence of differently-aligned ordered domains. This newer way to exploit the element sensitivity of REXS is a breakthrough in the field. It has been here implemented to further our understanding of the metal-insulator transition in Mn doped $\text{Sr}_3\text{Ru}_2\text{O}_7$ and of the intrinsic nematic fluid behavior of the parent compound; it can be used for a wide variety of other doped systems and transition metal oxides. Neutron scattering can probe magnetic order with site specificity; however, lacking the element specificity, this would not be possible for dilute and randomly distributed impurities.

It should be noted that neutron scattering experiments can detect spin order but cannot detect or confirm the presence of orbital order. The claim of t_{2g} orbital order in Mathieu's earlier paper is just a speculation. Since this is an interesting suggestion, it deserves a closer look and was among the motivations of our study. We showed that the $(\frac{1}{4}, \frac{1}{4}, 0)$ peak is due to spin order and there is no sign of orbital order, as evidenced by the agreement between the observed azimuthal dependence and a theoretical analysis based on the assumption of pure spin order. We also showed that the spin order is two-dimensional, with possibly up-up-down-down zigzag pattern, and spin direction is along the c -axis. Although we could not conclusively establish the precise pattern, we provided circumstantial supporting

evidence; this has a central role in the understanding of the nematic fluid behavior of the parent compound. The temperature dependence of the correlation length revealed that Mn impurities induce spin-ordered islands around them and thereby the metal-insulator transition at low temperatures; in other words, the ordering is triggered by the impurities and not by the majority Ru atoms. At the same time, the Mn-concentration independence of the forbidden superlattice diffraction peak points at an intrinsic instability of the parent compound. This information could only be found by probing randomly distributed Mn impurities separately from Ru, which is only possible by means of an element sensitive probe like REXS. We found the length scales and doping dependence of the separated phases. This is very important for the percolation driven inhomogeneous metal-insulator transitions, which are common in many correlated oxide systems. For example, the exact length scales of the insulating/metallic island are still controversial in important classes of materials such as the manganites [9].

Based on our work we can make few speculations that are tabulated below. From the continuous rise of the correlations length as the temperature is lowered below T_c , we can state that the ordered insulating islands of the average size 4×4 first appears at T_c and their spatial size grows as the temperature is lowed below T_c . This also implies that the ordered islands start to form around Mn at a certain temp above T_c , say at a temperature T^* (regardless of the doping concentration) and the spatial extent grow as we lower the temperature and at T_c the average size becomes 4×4 . In the dilute limit of 5%, these islands eventually get connected (at T_c) and form bigger ordered insulating clusters that eventually block all the metallic paths in the ab -plane, i.e. percolation threshold appears at T_c . This can already answer few important remaining questions:

1. Why does the metal-insulator transition (MIT) appears first at 5% doping concentration?

As we mentioned in the paper, 5% is the percolation threshold for a 4×4 insulating island (this particular size appears at $T_c \sim 40\text{K}$ for 5%). For 2.5% (that doesn't show any MIT at any temperature) it is possible that these islands are never big enough to reach the percolation threshold. This sets the limit for the maximum size of the insulating islands.

2. Why does T_c increase as we go to higher doping level (T_c for 5% and 10% are $\sim 40\text{K}$ and 70K)?

It takes smaller insulating island size to reach the percolation threshold for higher doping.

3. What is the origin of the non-monotonic temperature dependence of the diffraction peak intensity?

We assume that the insulating islands keep growing, even after forming bigger clusters. As the temperature is lowered below T_c , there should not be any problem in the interior region of the ordered clusters. However, the phase of the order for each of these clusters are already locked and when the edges of the clusters overlap there will be frustration and order will be destroyed in those overlap region. May be this is why

we see the non-monotonic temp dependence of the diffraction peak intensity. Also, the low-dimensionality of the proposed spin pattern can play a role in the down turn of the intensity.

The key unresolved issues are the following:

1. Where does the extra hole go?

Form our XAS studies we found that when a Ru is replaced by dilute Mn impurities, the valence of the Mn atoms are 3+ instead of the 4+ valence of the host atoms. This means each Mn atoms are donating a hole to the system. It is a question of fundamental interest that where this hole goes. There are several possibilities. The hole can go to one of the neighboring Ru site and make the Ru 5+. Alternatively, it can be shared by the four oxygen atoms surrounding the Mn site, forming a Zhang-Rice singlet [6] type of scenario. An element selective technique sensitive to screened and unscreened carriers in the system, e.g. core level photoemission spectroscopy can help to answer this fundamental question.

2. Why do we have $(\frac{1}{4}, \frac{1}{4}, 0)$ instability in the parent compound? Are there other magnetic instabilities?

A systematic ARPES study on $\text{Sr}_3\text{Ru}_2\text{O}_7$ doped by various magnetic impurities may shed light on this problem. It is possible that there exist a $\mathbf{q} = (\frac{1}{4}, \frac{1}{4}, 0)$ nesting vector in these compound and ARPES is the perfect tool to investigate this possibility. Also momentum dependent susceptibility calculations are needed to have a complete map of the existing magnetic instabilities.

7.7 Summary, significance and possibilities: YBCO

Our ARPES work on $\text{YBa}_2\text{Cu}_3\text{O}_{6.5}$ showed that due to the presence of polar surfaces there is electronic reconstruction on the surface of a cleaved sample. Since ARPES probes only the first few surface monolayers of a system, ARPES has always been probing this charge reconstructed surface and not the bulk electronic properties. We have devised a novel technique that allows us to control the surface doping level *in situ* by evaporating Potassium (K) on the YBCO surface. We showed that K tunes the surface doping level by donating electrons and thereby let us continuously tune the surface doping level throughout the phase diagram. The beauty of this approach is that we can use a single experimental technique to probe a single piece of sample giving us momentum dependent information covering the whole phase diagram. Our measurements on $\text{YBa}_2\text{Cu}_3\text{O}_{6.5}$ does show clear gap opening up as a function of potassium (K) deposition around the $(\pi, 0)$ point. However, this particular study cannot determine the nature of this gap apart from the fact that the $2 \times \text{gap}$ -value falls on the pseudogap line shown in Chapter 6, Fig. 6.2, giving support to our claim that ARPES can only probe the pseudogap. Also, our results reveal clear Fermi arcs in $\text{YBa}_2\text{Cu}_3\text{O}_{6.5}$ and opened up a unique opportunity to investigate the lack of the outer side of the pockets, where the electron-removal spectral weight is expected to be vanishingly small because of the strong drop in the quasiparticle coherence.

Overall, the ability to continuously tune the doping level of a cuprate surface and thereby letting ARPES to reliably deliver momentum resolved data has opened up exciting possibilities to shed new light on the origin and interplay of the pseudogap and the superconducting gap. For instance, as it has been suggested in the paper, by depositing K, one may be able to make electron doped cuprate starting from a hole doped bulk crystal. Also, the technique may be applied to other compounds with polar surfaces or applied to charge neutral surfaces to make them polar. These possibilities to tailor surfaces with specific charge content may provide insights about the physics of polar surfaces in general.

This work has, of course, generated important questions and thereby possibilities to do more. Some of these questions and possibilities are discussed below:

1. The approach of continuous control of the doping level of YBCO with K deposition can shed light on an important but unresolved issue in cuprate physics in general, namely the absence of apical oxygen in electron doped cuprates. So far, all the electron doped cuprates discovered has no apical oxygen site and this had led to the conjecture that absence of apical oxygen is a necessity for this class of materials. If it is possible to dope YBCO to the extreme that it crosses the zero doping line to the regime of electron doping, one may be able to disprove the conjecture regarding the absence of apical oxygen, since YBCO does contain apical oxygens.
2. How do the K impurities distributed over the surface of YBCO? Do they form any ordered pattern structurally? Spatially resolved probe like Scanning Tunneling Microscope (STM) with can answer this.
3. Do the K impurities induce any surface magnetism on YBCO, just like magnetism induced by charge reconstruction in oxide interfaces? Resonant elastic X-ray scattering on YBCO surface can shed light on this issue.
4. How do the K impurities affect the the layers just below the surface layer, i.e. change in the electronic structure as a function of c -axis thickness?
5. Does other types of cation than K, e.g. Na, has the same effect on polar surfaces of YBCO?
6. How K and other cations affect polar surface in general, e.g. on LSCO ($\text{La}_{2-x}\text{Sr}_x\text{CuO}_4$) or surfaces of oxides like LaAlO_3 that has alternating charged planes similar to YBCO. In case of LSCO, STM or STS experiments has failed on cleaved sample surface. This is believed to be connected to the charge instability/reconstruction arising from the fact that both the CuO_2 and $\text{La}_{1-\frac{x}{2}}\text{Sr}_{\frac{x}{2}}\text{O}$ are polar with charge $-(2-x)$ and $1-x/2$ respectively. Hence, applying cations like K on LSCO might be particularly interesting.
7. Can we think of interfaces like hole doped YBCO and an electron doped HTCS? For instance, how would a YBCO/NCCO ($\text{Nd}_{2-x}\text{Ce}_x\text{CuO}_4$) interface behave?
8. Where does this cation doping effect breaks down? It has been suggested in Chapter 5 that one may be able to electron dope a low hole doped YBCO to enter the electron

dope side of the phase diagram. This possibility needs to be checked and the exact limitations of this approach need to be found.

Bibliography

- [1] P. Kuiper *et al.*, Phys. Rev. Lett. **70**, 1549 (1993).
- [2] D. Alders *et al.*, Phys. Rev. B **57**, 11623 (1998).
- [3] R. Mathieu *et al.*, Phys. Rev. B **72**, 092404 (2005).
- [4] A. Damascelli, Z. Hussain and Z.-X. Shen, Rev. Mod. Phys. **75**, 473 (2003).
- [5] D.J. Singh and I. I. Mazin, Phys. Rev. B **63**, 165101 (2001).
- [6] F.C. Zhang and T.M. Rice, Phys. Rev. B **37**, 3759 (1988).
- [7] R. Rajaraman, Solitons and instantons, North-Holland (1982).
- [8] W.P. Su, J.R. Schrieffer and A.J. Heeger, Phys. Rev. Lett. **42**, 1698 (1979).
- [9] E. Dagotto, Nanoscale Phase Separation and Colossal Magnetoresistance, Springer-Verlag (2002).

Appendix A

List of publications

1. **Hossain, M.A.**, Bohnenbuck, B., Chuang, Y.-D., Cruz, E., Wu, H.-H., Zegkinoglu, I., Haverkort, M.W., Geck, J., Hawthorn, D.G., Hu, Z., Schüßler-Langeheine, C., Mathieu, R., Tokura, Y., Satow, S., Takagi, H., Yoshida, Y., Denlinger, J.D., Tjeng, L.H., Elfimov, I.S., Hussain, Z., Keimer, B., Sawatzky, G.A., and Damascelli, A. (2009) Spatially inhomogeneous metal-insulator transition in lightly Mn doped $\text{Sr}_3\text{Ru}_2\text{O}_7$. arXiv:0906.0035v1 (2009).
2. **Hossain, M.A.**, Mottershead, J.D.F., Fournier, D., Bostwick, A., McChesney, J.L., Rotenberg, E., Liang, R., Hardy, W.N., Sawatzky, G.A., Elfimov, I.S., Bonn, D.A., and Damascelli, A. (2008) In situ doping control of the surface of high-temperature superconductors. *Nature Physics*. **4**: 527-531.
3. **Hossain, M.A.**, Hu, Z., Haverkort, M.W., Burnus, T., Chang, C.F., Klein, S., Denlinger, J.D., Lin, H.-J., Chen, C.T., Mathieu, R., Kaneko, Y., Tokura, Y., Satow, S., Yoshida, Y., Takagi, H., Tanaka, A., Elmov, I.S., Sawatzky, G.A., Tjeng, L.H., and Damascelli A. (2008) Crystal-field level inversion in lightly Mn-doped $\text{Sr}_3\text{Ru}_2\text{O}_7$. *Physical Review Letters*. **101**: 016404.
4. Hübner, S., **Hossain, M.A.**, Damascelli, A., Sawatzky, G.A. (2008) Two Gaps Make a High-Temperature Superconductor? *Reports on Progress in Physics*. **71**: 062501.
5. Kikugawa, N., Rost, A., Baumberger, F., Ingle, N.J.C., **Hossain, M.A.**, Meevasana, W., Shen, K.M., Lu, D.H., Damascelli, A., Mackenzie, A.P., Hussain, Z., and Shen, Z.-X. (2007) $\text{Ca}_3\text{Ru}_2\text{O}_7$: Electronic instability and extremely strong quasiparticle renormalisation. *Journal of Magnetism and Magnetic Materials*. **310**: 10271029.
6. Baumberger, F., Ingle, N.J.C., Kikugawa, N., **Hossain, M.A.**, Meevasana, W., Perry, R.S., Shen, K.M., Lu, D.H., Damascelli, A., Rost, A., Mackenzie, A.P., Hussain, Z., and Shen, Z.-X. (2006) Nested Fermi Surface and Electronic Instability in $\text{Ca}_3\text{Ru}_2\text{O}_7$. *Physical Review Letters*. **96**: 107601.